Towards electrochemical-performance evaluation of fiber-based batteries Fiber-arrangement-based method and FE^2 multiscale framework

Zhuo, M.

DOI
10.4233/uuid:d70c85aa-7aa6-4ae0-970b-c944cec74dec

Publication date
2021

Document Version
Final published version

Citation (APA)
Zhuo, M. (2021). *Towards electrochemical-performance evaluation of fiber-based batteries: Fiber-arrangement-based method and FE^2 multiscale framework*. [Dissertation (TU Delft), Delft University of Technology]. https://doi.org/10.4233/uuid:d70c85aa-7aa6-4ae0-970b-c944cec74dec

Towards electrochemical-performance evaluation of fiber-based batteries

Fiber-arrangement-based method and FE^2 multiscale framework

Dissertation

for the purpose of obtaining the degree of doctor
at Delft University of Technology
by the authority of the Rector Magnificus, prof. dr. ir. T. H. J. J. van der Hagen,
chair of the Board for Doctorates,
to be defended publicly on
Thursday 28 January 2021 at 10:00 o'clock

by

Mingzhao ZHUO

Master of Philosophy in Mechanical Engineering,
Hong Kong University of Science and Technology, Hong Kong, China
born in Anhui, China

This dissertation has been approved by the promotors.

Composition of the doctoral committee:

Rector Magnificus,	chairperson
Prof. dr. ir. L. J. Sluys,	Delft University of Technology, promotor
Prof. dr. ir. A. Simone,	University of Padova, Italy, promotor
Independent members:	
Prof. dr. ir. E. Schlangen,	Delft University of Technology
Prof. Alejandro A. Franco,	Institut Universitaire de France, France
Prof. dr. ir. F. M. Mulder,	Delft University of Technology
Dr. Vahur Zadin,	University of Tartu, Estonia
Other members:	
Dr. Davide Grazioli,	University of Padova, Italy

The research presented in this thesis has received funding from the European Research Council under the European Union's Seventh Framework Programme (FP7/2007–2013) / ERC Grant agreement n° 617972.

Keywords: Li-ion batteries, fiber-based battery electrode, multi-scale, multi-physics, FE^2 method, computational homogenization

ISBN 000-00-0000-000-0

An electronic version of this dissertation is available at
http://repository.tudelft.nl/.

Contents

Preface

To my parents and sisters.

Mingzhao Zhuo
August 2020
Delft, the Netherlands

1

Introduction

Rechargeable lithium-ion batteries are the power sources in many fields, ranging from portable consumer electronics to electric vehicles.

Within the weight and size limitations of these devices, increasing power supply still remains the most challenging problem; the current electrochemical technology is far from providing an ideal—light, small, but powerful—battery.

For example, the present-day cell phones are suffering from the short-battery-life problem, and electric cars are always bothered by running out of charge, the so-called range anxiety.

1.1 Aims of the thesis

Lithium-ion (Li-ion) batteries are receiving extensive research attention because of their applications in a wide range of fields and the growing energy demand from the market. There have been a plenty of experimental activities in order to find more suitable materials and more efficient microstructures for better performance. However, most of the traditional modeling approaches assume, implicitly or explicitly, a specific microstructure for the active material, and thus they are not adequate to address the use of newly-emerging materials such as fiber-based composites.

This thesis aims to contribute to improving battery performance by developing computational tools for battery microstructure exploration. To this end, we employ two computational strategies: (1) a fiber-arrangement-based numerical approach that allows for the estimation of effective conductivity and capacity using Monte Carlo method and an equivalent resistor network model; (2) a FE^2 multiscale method for solving physics-based governing equations of batteries.

In the remainder of this general introduction, a succinct description of the basics of Li-ion battery cell, especially the electrode microstructure, is presented. The modeling efforts are then reviewed to serve the context for computational tools discussed in this thesis.

1.2 Li-ion batteries and new developments

A typical Li-ion battery cell and its working process is sketched in Fig. 1.1. The battery cell consists of five components: two current collectors, two electrodes, and a separator. The electrodes and separator have porous microstructures with electrolyte filling the pores to conduct ions. In the discharge process, the negative electrode gives out lithium ions and electrons. The lithium ions will move through the electrolyte to the positive electrode, while the electrons travel through the external circuit and react with the lithium ion in the positive electrode. In the charge process, the movement of electrons and lithium ions is reversed.

To get insights into how the battery works, we show the microstructure and composition of commercial battery cathodes in Fig. 1.2. The porous cathode consists of active materials, conductive materials, and the polymer binder. The pores are filled with liquid electrolyte. Present-day commercial batteries have two major types of cathodes differing in terms of the active material: the NMC and LFP cathodes, composed of Lithium Nickel Manganese Cobalt oxide ($LiNiMnCoO_2$) and Lithium Iron Phosphate ($LiFePO_4$), respectively. The porous anode often takes graphite as the active material. The separator is a porous polymer membrane with electrolyte filling the pores.

To satisfy the increasing energy demand, researchers and scientists have been working

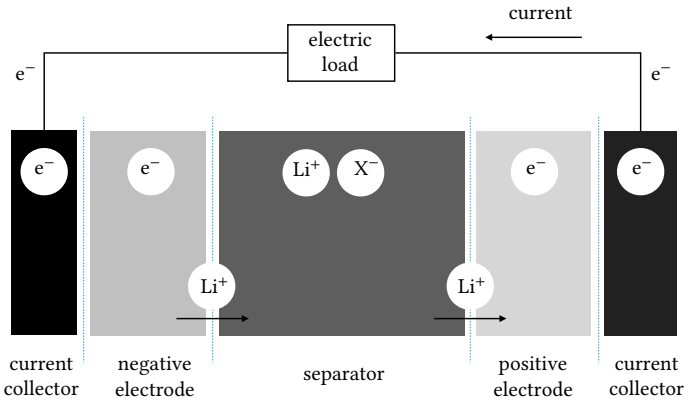

Fig. 1.1. Schematic representation of a typical battery cell and its discharging process.

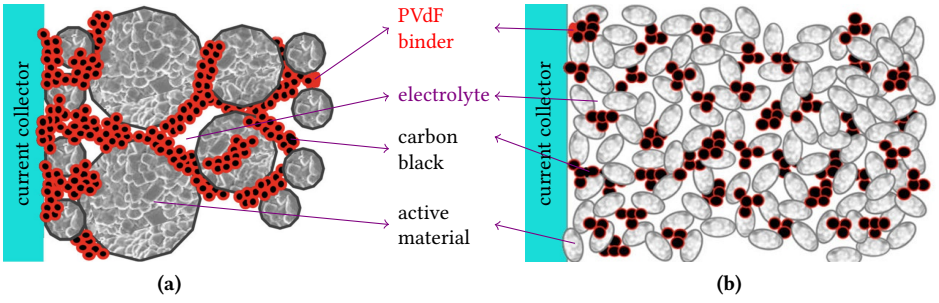

Fig. 1.2. Schematic of the composition of two popular commercial Li-ion battery cathodes: (a) an NMC cathode and (b) an LFP cathode [1]. The porous cathode consists of active materials, conductive carbon black, and PVdF polymer binder. The two types of cathodes differ in the choice of active materials: NMC electrodes use Lithium Nickel Manganese Cobalt oxide ($LiNiMnCoO_2$) while LFP takes Lithium Iron Phosphate ($LiFePO_4$). The electrolyte fills in the pores.

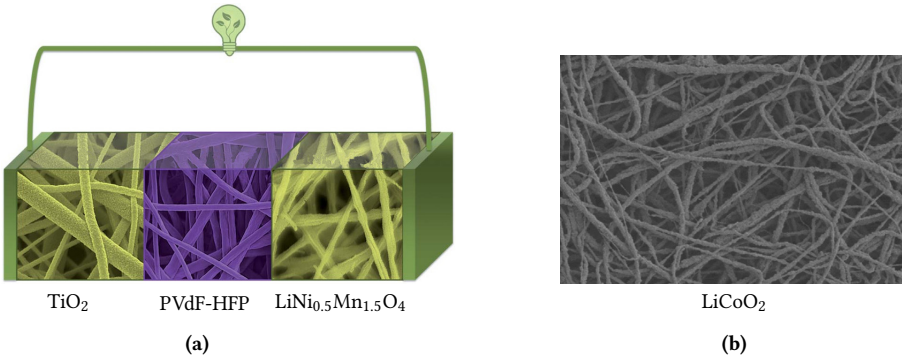

Fig. 1.3. (a) A Li-ion battery cell with all components consisting of electrospun nanofibers [6]. (b) SEM images of a $LiCoO_2$/C/PVdF cathode showing as-spun fiber mat [2].

intensively on exploring new materials and testing new battery cell designs. Among all these efforts, changing the material morphology from the current particle to nanofiber has been shown to be effective in strengthening the battery performance. Compared to particles, fibers possess higher surface-to-volume ratio and shorter diffusion paths, leading to improved charge/discharge rate capabilities and extended cycle life of the electrodes [2–5]. In Fig. 1.3, we show two examples of achieving exceptional performance by using electrospun nanofibers in batteries. A discussion on the fiber morphology benefits can be found in Section 2.1.

Besides material morphology improvement, another strategy is to develop multi-functional materials with combined structural and energy storage capabilities, called structural batteries. Currently, stand-alone bulky batteries are directly incorporated into electric devices resulting in a significant weight addition and interior volume reduction. However, these traditional batteries do not contribute to the structural performance of the devices: they are structurally parasitic. By merging the battery function with the structural casing of mobile devices, we can immediately reduce weight and size of our smart phones and laptops. Actually, 15% weight reductions are possible with batteries used as part of the body panel in a conceptual electric car as demonstrated by Volvo [7] (Fig. 1.4a). On the other hand, a slight power gain has been reported in an unmanned aircraft vehicle [8] due to a multifunctional structural battery embedded. Work by a Swedish interdisciplinary team of scientists has demonstrated that such multi-functional materials can be synthesized from carbon fiber reinforced polymer composites [9, 10]. An ideal structure battery model was proposed by Liu et al. [11] and shown in Fig. 1.4b.

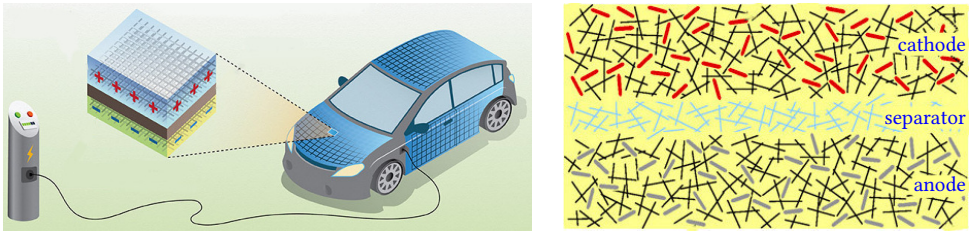

(a) (b)

Fig. 1.4. (a) Structure batteries made of carbon fibers could be used as the body panels of a car [12] for the combined purposes of mechanical function and energy storage. (b) An ideal model of a structural battery cell [11]: the cathode is made of $LiCoO_2$ active material fibers (red) and conductive carbon fibers (black) blended in a structural polymer binder (yellow); the separator is the structural polymer reinforced by insulating glass fibers (blue); the anode is similar to the cathode but takes graphite (gray) as the active material. The structural polymer binder also functions as the solid electrolyte to conduct ions.

1.3 Existing battery modeling efforts

Compared to experimental exploration, modeling and simulation are more efficient approaches in terms of processing cost for understanding the physics of battery operation and hence optimizing battery design and health management. This section briefly reviews the battery modeling strategies in the literature.

The most popular model up to the present is the pseudo-two-dimensional (P2D) model introduced by Doyle et al. [13]. The P2D model is based on the porous electrode theory and concentrated solution theory [13] to predict electrochemical responses. The porous electrode consists of a solid porous matrix of the active material, conductive material, and structural polymer binder, and the electrolytic solution filling the void spaces of the porous matrix [14]. According to the porous electrode theory, the composite electrode is homogenized as a superposition of two continuous phases—the solid porous matrix and liquid electrolyte—at the cell level. The homogenized electrolyte phase is characterized by the lithium ion concentration c_e and electric potential ϕ_e, while the homogenized solid phase is only associated with the electric potential ϕ_s. The lithium concentration c_s is modeled in a representative active material particle at the pore-scale (Fig. 1.5). The lithium ion diffusion and migration as well as the current flow in the electrolyte phase are described by those derived from the concentrated solution theory [13, 14]. The lithium diffusion in the solid particle and the electric potential variation on the homogenized solid phase are governed by Fick's first law and Ohm's law, respectively. The interfacial flux between the solid particles and electrolyte, governed by the kinetics equations, is used to bridge macro- and micro-scales. Regarding effective transport properties, porosity alone is used to characterize the microstructure and correct bulk transport properties. Based on particle representation of

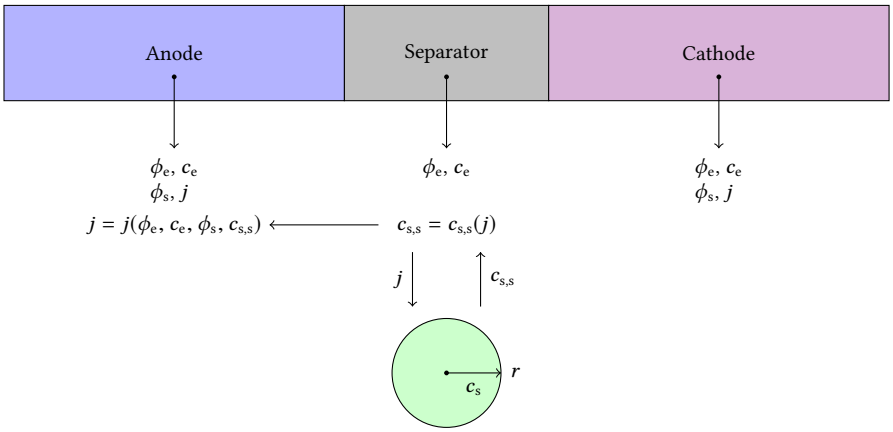

Fig. 1.5. Schematic representation of the P2D model and the flow of quantities between macro- and micro-scales. At the macroscale (cell level), there are four variables: c_e and ϕ_e are the lithium ion concentration and electric potential associated with the electrolyte phase, ϕ_s denotes the electric potential of the solid phase, and j is the interfacial flux between the active material particle and electrolyte. The interfacial flux j depends on the above mentioned three macroscale variables and also the surface lithium concentration $c_{s,s}$ in the active material particle, which is in turn a function of j through the microscale diffusion problem in the particle.

microstructure, numerous modeling works have been developed to extend the P2D model for example in terms of the electrochemical–mechanical interaction [15–17].

The P2D model is in essence a multiscale approach, but the microscale consideration is restricted to the simple case of a spherical particle. Besides the particle microstructure representation, more complicated random microstructures were considered in other studies [18, 19] so that more accurate effective transport properties and interfacial flux can be obtained from the microscale simulation. Du et al. [18] applied the volume averaging method [20, 21] to the microscale electrochemical governing equations and derived the macroscale homogenized equations with closure terms that are solved on microscale representative elementary volumes. From the numerical simulation data of representative elementary volumes, a fitted effective transport coefficient was used to replace Bruggeman's approximation, and a surrogate model was built to give the interfacial flux as a function of macroscale field variables. Lee et al. [19] adapted the variational multiscale enrichment to Li-ion battery systems for improved battery performance predictions. Unlike conventional homogenization approaches, this method decomposes the scales without assuming scale separation and is capable of considering the transient phenomenon at the microscale.

With increasing computational power, it gradually becomes feasible to solve physics-based differential equations over the problem domain with fully-resolved microstructure, i.e., direct numerical simulation [22–24]. Since this strategy does not differentiate length scales, we will refer to it as the single-scale approach, in contrast to those multiscale models.

Such kind of approaches avoid the errors introduced by the homogenization process in the multiscale approaches, at the expense of higher computational cost especially when the domain spans length scales of a few orders of magnitude.

1.4 Proposed numerical approaches

For fiber-based battery electrodes, a particle representation as in the P2D model is apparently infeasible. Compared to a particle, a fiber has two extra dimensions of length and orientation on top of the radius. Thus using a single fiber to simplify the microstructure is also not representative. Regarding the single-scale simulation, the fibers make the simulation of physics-based differential equations extremely difficult in terms of discretizing the geometry of the embedded fibers and the associated matrix. Also, the cost of solving a large system of linearized equations further discourages the single-scale approach. A possible strategy is to adopt a multiscale approach as in those by Du et al. [18] and Lee et al. [19], if simulating the electrochemical processes by solving physics-based equations is desired.

Different from these existing multiscale models, we propose to develop a FE^2 framework that features well-defined microscale problems and information exchanges between macro- and micro-scales in Chapters 3 and 4. This study is however preceded by an efficient preliminary estimation of electrode capacity based on the fiber arrangement. Details about these two approaches are as follows.

1.4.1 Fiber-arrangement-based estimation

We first use an efficient numerical approach for characterizing fiber-based battery electrodes, including estimating the percolation threshold, electronic conductivity, and utilization of the active material. Specifically, we use Monte Carlo method [25] to randomly distribute fibers and generate numerical samples of representative volume elements (RVEs). The connection between fibers is detected for the purposes of determining the percolation threshold, calculating the electronic conductivity with further employment of the resistor network model [26, 27], and identifying optimal conductive material fiber content for the maximum capacity.

The above-described method does not need to solve physics-based differential equations and thus the computational cost is relatively low. This preliminary investigation could serve as a reference for results by solving physics-based governing equations for example using the following FE^2 multiscale method.

1.4.2 FE^2 method

The FE^2 method has been developed and used in a wide range from mechanical problems [28–31] to transport problems [32–34] with the aim of addressing heterogeneous materials spanning several orders of magnitude. The method consists of solving the governing equations at the macro- and micro-scales. The macroscale constitutive relations are numerically obtained from the microscale problem that is defined at each integration point of the macroscale mesh. Because of the well-defined boundary conditions based on the downscaled macroscale quantities, the microscale problem can well mimic the real material responses at the microscale.

The theoretical extension of the FE^2 method to battery systems has been investigated by Salvadori et al. [35, 36] who defined a complex multiscale scheme involving multiple physics phenomena at different time- and length-scales. At variance with their approach, we address the problem in a simper manner. First, we consider transient diffusion problem over a two-phase medium and separately predict the field variable within each phase. Second, we consider the electrochemical processes occurring in the electrolyte without interaction with the active material that is simply assumed as ion-transport-blocking obstacles.

The FE^2 simulation can provide accurate results up to the extent of direct numerical simulations that fully resolve the microstructure. As the microscale simulation resolves an RVE with random morphology, the FE^2 method is actually a general approach for batteries with a generic microstructure.

1.5 Scope and outline

This thesis attempts to develop modeling frameworks for evaluating electrode properties and solving multi-physics problems in batteries. In accordance with the approaches outlined above, we first report the numerical study of electrochemical property estimation of fiber-based battery electrodes in Chapter 2. Next we present the work related to the FE^2 multiscale method in Chapters 3 and 4. In summary, we restrict our focus to three major parts:

- numerical approaches allowing for the estimation of the percolation threshold, effective electronic conductivity, and capacity from the fiber arrangement of fiber-based battery electrodes (Chapter 2);
- a FE^2 framework to solve the two-equation model of transient diffusion in two-phase media (Chapter 3);
- a FE^2 framework to simulate the ionic transport processes in porous battery separators (Chapter 4).

References

[1] A. Etiemble, N. Besnard, A. Bonnin, J. Adrien, T. Douillard, P. Tran-Van, L. Gautier, J.-C. Badot, E. Maire, and B. Lestriez, *Multiscale morphological characterization of process induced heterogeneities in blended positive electrodes for lithium–ion batteries,* Journal of Materials Science **52**, 3576 (2016).

[2] E. C. Self, E. C. McRen, R. Wycisk, and P. N. Pintauro, *$LiCoO_2$-Based Fiber Cathodes for Electrospun Full Cell Li-ion Batteries,* Electrochimica Acta **214**, 139 (2016).

[3] H.-W. Lu, L. Yu, W. Zeng, Y.-S. Li, and Z.-W. Fu, *Fabrication and Electrochemical Properties of Three-Dimensional Structure of $LiCoO_2$ Fibers,* Electrochemical and Solid-State Letters **11**, A140 (2008).

[4] Y. Gu, D. Chen, and X. Jiao, *Synthesis and Electrochemical Properties of Nanostructured $LiCoO_2$ Fibers as Cathode Materials for Lithium-Ion Batteries,* Journal of Physical Chemistry B **109**, 17901 (2005).

[5] E. S. Pampal, E. Stojanovska, B. Simon, and A. Kilic, *A review of nanofibrous structures in lithium ion batteries,* Journal of Power Sources **300**, 199 (2015).

[6] N. Arun, V. Aravindan, S. Jayaraman, N. Shubha, W. C. Ling, S. Ramakrishna, and S. Madhavi, *Exceptional performance of a high voltage spinel $LiNi_{0.5}Mn_{1.5}O_4$ cathode in all one dimensional architectures with an anatase TiO_2 anode by electrospinning,* Nanoscale **6**, 8926 (2014).

[7] Volvo Car, *Tomorrow's volvo car: Body panels serve as the car battery,* Accessed: 2020-03-25.

[8] J. P. Thomas and M. A. Qidwai, *The design and application of multifunctional structure-battery materials systems,* JOM **57**, 18 (2005).

[9] S. Leijonmarck, T. Carlson, G. Lindbergh, L. E. Asp, H. Maples, and A. Bismarck, *Solid polymer electrolyte-coated carbon fibres for structural and novel micro batteries,* Composites Science and Technology **89**, 149 (2013).

[10] L. E. Asp, *Multifunctional composite materials for energy storage in structural load paths,* Plastics, Rubber and Composites **42**, 144 (2013).

[11] P. Liu, E. Sherman, and A. Jacobsen, *Design and fabrication of multifunctional structural batteries,* Journal of Power Sources **189**, 646 (2009).

[12] L. E. Asp, M. Johansson, G. Lindbergh, J. Xu, and D. Zenkert, *Structural battery composites: A review,* Functional Composites and Structures **1**, 042001 (2019).

[13] M. Doyle, T. F. Fuller, and J. Newman, *Modeling of galvanostatic charge and discharge of the Lithium/polymer/insertion cell,* Journal of The Electrochemical Society **140**, 1526 (1993).

[14] J. Newman and K. E. Thomas-Alyea, *Electrochemical systems* (John Wiley & Sons, 2012).

[15] S. Golmon, K. Maute, and M. L. Dunn, *Numerical modeling of electrochemical-mechanical interactions in lithium polymer batteries,* Computers & Structures **87**, 1567 (2009).

[16] B. Wu and W. Lu, *A consistently coupled multiscale mechanical–electrochemical battery model with particle interaction and its validation,* Journal of the Mechanics and Physics of Solids **125**, 89 (2019).

[17] Y. Bai, Y. Zhao, W. Liu, and B.-X. Xu, *Two-level modeling of lithium-ion batteries,* Journal of Power Sources **422**, 92 (2019).

[18] W. Du, N. Xue, W. Shyy, and J. R. R. A. Martins, *A surrogate-based multi-scale model for mass transport and electrochemical kinetics in Lithium-ion battery electrodes,* Journal of The Electrochemical Society **161**, E3086 (2014).

[19] S. Lee, A. M. Sastry, and J. Park, *Study on microstructures of electrodes in lithium-ion batteries using variational multi-scale enrichment,* Journal of Power Sources **315**, 96 (2016).

[20] S. Whitaker, *The Method of Volume Averaging* (Springer Netherlands, 1999).

[21] W. Shyy, S. S. Thakur, H. Ouyang, J. Liu, and E. Blosch, *Computational Techniques for Complex Transport Phenomena* (Cambridge University Press, 1997).

[22] G. M. Goldin, A. M. Colclasure, A. H. Wiedemann, and R. J. Kee, *Three-dimensional particle-resolved models of Li-ion batteries to assist the evaluation of empirical parameters in one-dimensional models,* Electrochimica Acta **64**, 118 (2012).

[23] R. Fang, P. Farah, A. Popp, and W. A. Wall, *A monolithic, mortar-based interface coupling and solution scheme for finite element simulations of lithium-ion cells,* International Journal for Numerical Methods in Engineering **114**, 1411 (2018).

[24] W. Mai, M. Yang, and S. Soghrati, *A particle-resolved 3D finite element model to study the effect of cathode microstructure on the behavior of lithium ion batteries,* Electrochimica Acta **294**, 192 (2019).

[25] H. Ma and X.-L. Gao, *A three-dimensional Monte Carlo model for electrically conductive polymer matrix composites filled with curved fibers,* Polymer **49**, 4230 (2008).

[26] M. Jagota and N. Tansu, *Conductivity of Nanowire Arrays under Random and Ordered Orientation Configurations,* Scientific Reports **5**, 10219 (2015).

[27] A. Abbaspour, J.-L. Luo, and K. Nandakumar, *Three-dimensional random resistor-network model for solid oxide fuel cell composite electrodes,* Electrochimica Acta **55**, 3944 (2010).

[28] V. Kouznetsova, W. A. M. Brekelmans, and F. P. T. Baaijens, *An approach to micro-macro modeling of heterogeneous materials,* Computational Mechanics **27**, 37 (2001).

[29] C. Miehe, *Strain-driven homogenization of inelastic microstructures and composites based on an incremental variational formulation,* International Journal for Numerical Methods in Engineering **55**, 1285 (2002).

[30] C. Miehe, *Computational micro-to-macro transitions for discretized micro-structures of heterogeneous materials at finite strains based on the minimization of averaged incremental energy,* Computer Methods in Applied Mechanics and Engineering **192**, 559 (2003).

[31] M. Geers, V. Kouznetsova, and W. Brekelmans, *Multi-scale computational homogenization: Trends and challenges,* Journal of Computational and Applied Mathematics **234**, 2175 (2010).

[32] I. Özdemir, W. A. M. Brekelmans, and M. G. D. Geers, *Computational homogenization for heat conduction in heterogeneous solids,* International Journal for Numerical Methods in Engineering **73**, 185 (2007).

[33] I. Özdemir, W. Brekelmans, and M. Geers, *FE^2 computational homogenization for the thermo-mechanical analysis of heterogeneous solids,* Computer Methods in Applied Mechanics and Engineering **198**, 602 (2008).

[34] A. Sengupta, P. Papadopoulos, and R. L. Taylor, *A multiscale finite element method for modeling fully coupled thermomechanical problems in solids,* International Journal for Numerical Methods in Engineering **91**, 1386 (2012).

[35] A. Salvadori, E. Bosco, and D. Grazioli, *A computational homogenization approach for Li-ion battery cells: Part 1 – formulation,* Journal of the Mechanics and Physics of Solids **65**, 114 (2014).

[36] A. Salvadori, D. Grazioli, and M. G. D. Geers, *Governing equations for a two-scale analysis of Li-ion battery cells,* International Journal of Solids and Structures **59**, 90 (2015).

2

Active material utilization and capacity of fiber-based battery electrodes

Abstract

Electrospun nanofibers have recently been considered for the production of battery electrodes. To give insights on how this electrode architecture perform and to suggest effective design solutions, we propose a computational model to evaluate percolation threshold, effective conductivity, and capacity of fiber-based electrodes. We employ electrodes composed of conductive and active material nanofibers dispersed in an electrolyte matrix. Percolation threshold, identified as the minimum content of conductive fibers to form an electronically-conductive network, is determined by Monte Carlo methods, while effective conductivity is calculated by an equivalent resistor network model. Capacity evaluation is based on the identification of active material fibers that are accessible to electrons (i.e., those connected with the electronically-conductive network). When a constraint is applied to the total fiber content, an optimal active-conductive material ratio is determined that allows to maximize the active material utilization and the electrode capacity. Furthermore, we study fiber orientation effects on these electrochemical quantities. We find that fiber orientation has a strong impact on the percolation threshold and this reflects on the active material utilization. For a given total (active and conductive) fiber content, the more the fiber orientation deviates from the ideal isotropic distribution, the lower the utilization of active material fibers. This is of special interest for practical applications where geometrical constraints on fiber orientation arise, as in the case of electrospun fibers deposited on a substrate.

keywords: fiber-based composite electrode, percolation threshold, resistor network model, optimal active-conductive material ratio, fiber orientation effect

Parts of this chapter have been published in Zhuo et al. [1].

2.1 Introduction

Electrospun nanofibers improve the electrochemical performance of a battery cell when used in electrodes [2–4] due to increased surface-to-volume ratio, shorter transport paths, and enhanced intercalation kinetics [5, 6] compared to the traditional conductive material particle morphology. Numerical simulations of the electrochemical processes taking place in traditional battery electrodes at the microstructural level require the solution of sets of coupled differential equations and are computationally demanding [7]. In addition to this, the microstructural analysis of fiber-based electrodes requires the discretization of each fiber, increasing the computational burden to such an extent that the solution of the problem becomes too expensive to be tackled for practical purposes. Here we propose a numerical approach that allows the estimation of effective conductivity and capacity from the fiber arrangement.

For improved battery performance, a new avenue has been opened up: changing the electrode material morphology from particle to nanofiber. Metallic [8] or carbonaceous [9–12] fibers are employed to enhance the electronic conductivity of battery electrodes. Experimental studies show that conductive material fibers ("conductive fibers" will be used for conciseness hereafter) help achieve electrode percolation using less conductive material [8, 10] and improve the electrolyte ionic conductivity by creating preferential paths for ionic transport along their surfaces [10]. The production of fibers for battery applications is not limited to conductive materials. Thanks to electrospinning, a wide range of anode [2, 13, 14] and cathode [2, 15] active materials can nowadays be prepared in fiber form and used in battery cells [16, 17]. The reduced dimensions of nanofibers ensure shorter diffusion paths and higher surface-to-volume ratio relative to the traditional morphology, leading to improved capacity, higher charge/discharge rate capabilities, and extended cycle life of the electrodes [15, 18–20]. The combination of active and conductive materials in fiber form was proposed by Liu et al. [21] for structural battery applications. This novel design, although not fully realized in their experiments, has provided a new direction for the development of multi-functional fiber-based electrodes and some of its features will be investigated in Section 2.3.

The essential components of traditional lithium-ion battery electrodes are active material particles, conductive material additives, and electrolyte. Active material particles act as lithium sources/reservoirs and their amount determines the maximum electrode capacity. Conductive material additives provide pathways for electron transport between current collectors and active material particles, while the electrolyte is where ionic transport takes place. The lithium ions and electrons should meet at the active material-electrolyte interface to allow lithium insertion into the active material [22]. Due to the limiting supply of electrons and ions, the active material is often not fully utilized [22, 23], as suggested by the fact that the experimentally measured effective capacity is usually smaller than the theoretical

capacity [15, 24]. The conductive material (usually carbon black powder) is required to form a conductive network [25] throughout the electrode, i.e., a minimum amount of conductive material (related to the percolation threshold) is required in electrode design. However, a relative excess of conductive material decreases the capacity with limited improvement on the rate capabilities as reported in Ref. [26].

In traditional electrodes [23], the overall performance depends on the synergy among all their components. By way of example, one of the factors influencing electrode performance is the weight/volume ratio between active and conductive materials—experimental evidence indicates that this ratio impacts on the capacity of particle-based electrodes [26]. It is reasonable to expect qualitative analogies between particle-based and fiber-based electrodes. Indications regarding the quantitative contributions of the various components in a fiber-based electrode architecture are however not yet available, thus hindering the investigation of innovative electrode designs that could for instance allow the full utilization of the available active material.

Two types of models are usually considered to simulate electrochemical processes in particle-based electrodes. The first type regards the porous electrode as a homogenized macroscopic domain and makes use of a simplified representation of the microstructure for the evaluation of local fields (one such model is the pseudo two-dimensional model developed by Newman [27]); the second type simulates electrochemical processes by directly resolving the particle/pore microstructure [7]. Newman's model is computationally efficient but cannot be directly applied to fiber-based electrodes if investigations concerning the effect of fiber arrangement are targeted. Full scale simulations are also not suitable for fiber-based electrodes because parametric studies would require a significant computational effort due to the discretization of each fiber. These models are therefore deemed unsuited for fiber-based electrode architectures, and a simpler yet effective computational approach, discussed in Section 2.2, is preferred. This approach allows us to effectively explore a wide range of electrode configurations in terms of fiber content and distribution at a relatively low computational cost. Instead of simulating electrochemical processes through the solution of the governing equations, we rely on the identification of electronically-conductive fiber networks and active material fibers ("active fibers" will be used for conciseness hereafter) accessible to electrons to estimate electrode properties such as percolation threshold, electronic conductivity, and volumetric/gravimetric electrode capacity.

The percolation threshold of the composite electrode is evaluated by the two Monte Carlo methods described in Section 2.2.1. A comparison of their results in Section 2.3.1 leads to a new explanation regarding the value chosen as the percolation threshold. The analysis is then extended considering fiber orientation effects in a three-dimensional setting in Section 2.3.4. Next, the effective conductivity is determined through an equivalent resistor network model (Section 2.2.2) and discussed in Section 2.3.2 for a three-dimensional

isotropic distribution. We also investigate the fiber orientation effect on the effective electronic conductivity in a three-dimensional setting (Section 2.3.4). This allows us to extend the two-dimensional results reported by Jagota and Tansu [28] and to realistically mimic the layer-by-layer fiber arrangement typical of electrospun fibers (which is only possible in a three-dimensional setting). Finally, with the goal to determine the optimal active-conductive material ratio, we assume in Section 2.2.3 that the electrode capacity is contributed by the effective active fibers that are connected to the percolated conductive fiber network. This leads to the results in Section 2.3.3 where we identify the active-conductive material ratio that maximizes the capacity at a given total fiber content. Our predictions in Section 2.3.3 show a good qualitative agreement with the optimal ratio experimentally identified by Guzmán et al. [26] for particle-based electrodes. This result confirms that fiber-based electrodes can be used in place of traditional electrodes as also shown by the electrode design application discussed in Section 2.3.3.

2.2 Computational model and methods

The fiber-based electrode under investigation is composed of conductive fibers and active fibers dispersed in either a solid polymer electrolyte (as in the conceptual design by Liu et al. [21]) or a liquid electrolyte [15]. The electrolyte is however neglected in our model because it is considered as a medium that holds fibers in place but does not contribute to the electronic conductivity and capacity. The effective electronic conductivity of the composite electrode is assumed to be exclusively contributed by the conductive fiber network since the electronic conductivity of active materials [29] is several orders of magnitude smaller than that of conductive materials [4, 30, 31]. The fibers are idealized as spherocylinders of length l and diameter d as shown in Fig. 2.1, with aspect ratio l/d.

Jayaraman et al. [17] have experimentally detected interconnected nanofibers in electrospun fiber mats for electrode applications. To the best of our knowledge, a reliable quantification of the number and spatial configuration of such fibers and those that are not interconnected can only be obtained by means of dedicated experimental investigations as it is very much dependent on the manufacturing conditions. These difficulties make a thorough investigation of generic electrospun fiber mats not viable. Moreover, the generation of interconnected fiber ensembles is characterized by a computational burden significantly lower compared to that of non-interconnected fiber ensembles, and it allows to explore a wider range of fiber arrangements. Accordingly, we employ the soft-core assumption [32, 33] to generate interconnected fiber configurations.

We generate a unit cubic simulation box with faces parallel to the coordinate planes to represent the microstructural volume of the composite electrode. Each fiber is specified by

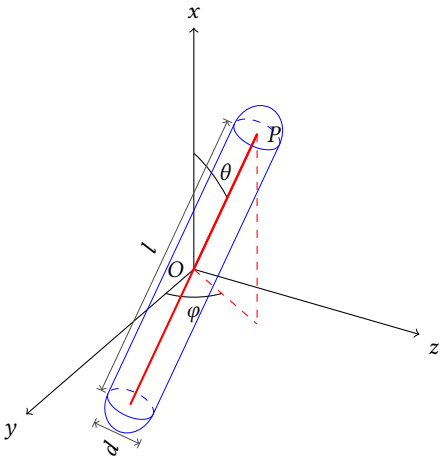

Fig. 2.1. For a fiber of length l and diameter d, a spherical coordinate system is attached to its middle point O and its end point P is uniquely determined by two orientation angles θ and φ. The fiber is represented as a three-dimensional spherocylinder with the red line as the axial line.

its middle point and two orientation angles as shown in Fig. 2.1. Fiber middle points O are assumed to be uniformly distributed in the simulation box, and their coordinates are three independent random numbers from the standard uniform distribution. The two orientation angles are the polar angle θ with respect to the x axis and the azimuthal angle φ with respect to the y axis. We choose the azimuthal angle φ from a uniform distribution over the interval $[0, 360^\circ]$. As for the polar angle θ, we have considered two cases: θ from 0 to the limit angle θ_m (case I), and θ from θ_m to 90° (case II). In both cases, the limit values are included, and θ_m takes on a value between 0 and 90°. The angle θ_m in case I indicates the degree of fiber alignment along the x direction [34]: when $\theta_m = 90^\circ$, the fibers are isotropically distributed in three dimensions (scenario A); as θ_m goes to 0, the fibers are completely aligned along the x direction (scenario B). In case II, the angle θ_m is related to the degree of fiber alignment on planes perpendicular to the x direction: when $\theta_m = 0$, the three-dimensional isotropic state (scenario A) is recovered; when $\theta_m = 90^\circ$, the fibers are isotropically distributed over planes parallel to the yoz plane (scenario C).

The isotropic fiber distribution (scenario A) will serve as reference in Section 2.3.4 to study the effect of fiber orientation when compared to the other distributions. Fibers aligned along one direction (scenario B) are known to maximize material properties in that direction (for example, the electronic conductivity in two- [28] and three- [34] dimensional settings). This fiber distribution can be obtained by electrospinning [35, 36]. The planar fiber distribution (scenario C) corresponds to the case of electrospun fibers deposited on a substrate with a layer-like fiber arrangement in the thickness direction [35]. Layer-by-layer

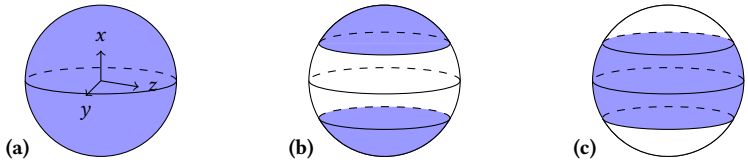

Fig. 2.2. Fiber end point distribution for scenario A (a), case I (b) and case II (c). The blue surface area represents the region where the fiber end points can be dispersed.

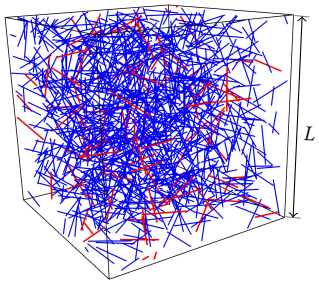

Fig. 2.3. Virtual model of a fiber-based composite electrode with conductive (blue) and active (red) fibers.

stacked fibers have been fabricated to serve as battery electrodes [12, 13, 35–37].

For the three-dimensional isotropic fiber distribution (scenario A), the values of the polar angle θ are chosen such that the fiber end points P (Fig. 2.1) uniformly cover the surface of a sphere as shown in Fig. 2.2a [32, 38]. Likewise, for the fiber distributions in cases I and II, the polar angles θ are generated in such a way that every differential area on the restricted sphere surface, i.e., the blue area in Fig. 2.2b (case I) and c (case II), has the same probability of being a fiber end point. Specific details on the generation of the angle θ are in 2.A.

We insert conductive and active fibers into the simulation box by means of the random sequential adsorption algorithm (RSA) [39]. Because of the soft-core assumption, the fibers can overlap, and their position is independent of the position of previously-generated fibers. Fibers intersecting the box boundaries are dealt with using the periodicity assumption. Figure 2.3 shows a realization of an isotropic fiber distribution (scenario A) using two species of fibers.

A fiber-based electrode consists of active fibers, conductive fibers, and the electrolyte filling the volume surrounding the fibers. The three components occupy volumes V_a, V_c and V_e, respectively, and these quantities are related through the relation

$$V_a + V_c + V_e \simeq V, \tag{2.1}$$

with V the volume of the entire electrode. Equation (2.1) is an approximation that does

not account for the volume shared by interconnected fibers (remember that the soft-core assumption holds). Since the interconnected volume is negligible compared to the total fiber volume [32], the error introduced is ignored in the following derivations. Dividing Eq. (2.1) by the electrode volume V, we obtain the relation

$$\phi_a + \phi_c + \phi_e = 1 \tag{2.2}$$

between the volume fraction of each component where

$$\phi_a = \frac{V_a}{V}, \quad \phi_c = \frac{V_c}{V}, \quad \text{and} \quad \phi_e = \frac{V_e}{V}$$

represent the volume fraction of active fibers, conductive fibers, and electrolyte, respectively. The relation between volume fraction ϕ and fiber number N is approximated as

$$\phi = \frac{N\pi l d^2}{4L^3}, \tag{2.3}$$

where L is the box edge length (Fig. 2.3).

In the following, we first present methods to evaluate percolation threshold (Section 2.2.1) and electronic conductivity (Section 2.2.2). In the simulations, only the conductive fibers are considered. Conventional Monte Carlo methods and an equivalent resistor network model are used to calculate percolation threshold and conductivity, respectively. In Section 2.2.3, the two species of fibers are taken into account to evaluate the electrode capacity. We introduce the effective ratio and detail the approach to calculate it, which requires identification of percolation threshold in the first step.

2.2.1 Monte Carlo methods

Fiber-like inclusions are widely employed to enhance thermal [40, 41], electronic [42–44], and ionic conductivity [45] of solid polymers. In the fiber-based electrodes considered in this study, the conductive fibers serve to enhance the electronic conductivity. We use conventional Monte Carlo methods to determine the minimum amount of conductive fibers (i.e., percolation threshold) for electronic conductivity of the electrode.

The effective electronic conductivity of a fiber-based composite depends on its fiber content. When the fiber content is low, the response of the hosting matrix prevails and the composite behaves like an insulator; when the fiber content is sufficiently high, the composite behaves as an electronic conductor. The fiber content at which the insulator-conductor transition occurs is known as percolation threshold or critical fiber volume fraction [42, 46, 47]. This corresponds to the first formation of an interconnected fiber network along a specific direction as manifested by the sharp change of effective properties (the electronic conductivity

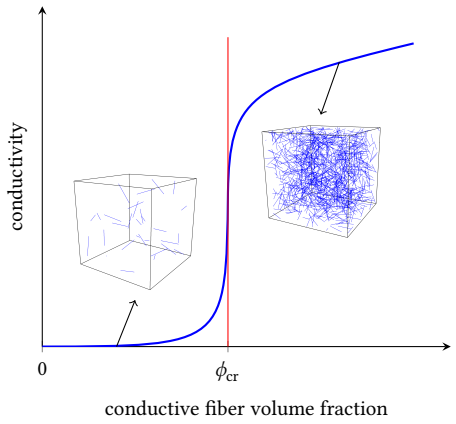

Fig. 2.4. Schematic of conductivity increase at percolation threshold ϕ_{cr}.

in our case) highlighted in Fig. 2.4. Since no interconnected network forms when the fiber content is below the percolation threshold, any evaluation of effective conductivity and capacity is subordinate to the identification of such a transition value. The methods employed to determine the percolation threshold are described in this section.

We assume electrons only travel across connected fibers and ignore electron hopping, also known as tunneling effect [48, 49], between geometrically-separated fibers. Fibers i and j are connected if they satisfy the condition

$$h \leq \frac{d_i + d_j}{2}, \tag{2.4}$$

where d_α represent the diameter of fiber α $(= i, j)$, and h is the shortest distance between the axial line segments. A robust algorithm to calculate the shortest distance between two line segments can be found in Ref. [50]. To determine if an interconnected fiber network exists, the fibers in the box that satisfy condition (2.4) are grouped into the same cluster. If a cluster extending between two opposite faces of the simulation box exists, the box is defined as being percolated along the direction perpendicular to those faces. The fiber cluster is then identified as the percolated fiber network.

A widely-used method (called method A in the following) to calculate the percolation threshold works by computing the percolation probability, namely the likelihood of getting percolated, for different fiber contents. Consider a simulation box containing N fibers. We evaluate percolation of the box by grouping the fibers into clusters. Two integer indexes in the range $[1, N]$ are attached to each fiber: the first (i) identifies the fiber, the second (j) identifies the cluster it belongs to. The same value $(j = i)$ is assigned to the two indexes

when a box is generated. Then, fiber i is checked against fiber j (with j from $i+1$ to N). If these two fibers satisfy the connection criterion (2.4), the smaller cluster index from fiber i and j is assigned to all the fibers detected as connected with either fiber i or j. At the end of this procedure, we check if two fibers with the same cluster index are identified at two opposite faces of the box. If so, at least one connected fiber network across the box exists and we thus consider the box percolated.

We then create m_A simulation boxes with the same fiber number N but different fiber configurations. For each box we evaluate its percolation using the algorithm previously described. The count of successfully percolated boxes is denoted as n, and thus the percolation probability is calculated as n/m_A. The more the trials m_A, the closer the probability n/m_A to the theoretical probability, according to the law of large numbers. The number of trials m_A is identified when increasing m_A does not change the percolation probability n/m_A (details are provided in Section 2.3.1).

By changing the fiber number N and repeating the procedure, we can establish a relation between percolation probability and the fiber number N. The choice of the fiber number N is a trial-and-error procedure that aims to the production of a set of dense data points spanning the percolation probability range $[0, 1]$. The fiber number corresponding to a percolation probability of 0.5 is chosen as the percolation threshold [51–54], and the reason behind this choice is discussed in Section 2.3.1.

Method A is computationally expensive. A cheaper method (called method B) is described next [43]. We insert the conductive fibers one at a time and, after each insertion, check whether the box percolates as follows. Each newly added fiber i is checked against all previously inserted fibers. If a connected fiber cluster is identified, we stop and define the number of the fibers added until this point as the critical fiber number N_{cr} at percolation. The same procedure is repeated m_B times and the percolation threshold is taken as the mean value of the m_B critical fiber numbers. The number of samples m_B is chosen so that negligible changes in the average critical fiber number are observed with further increase of m_B (details are provided in Section 2.3.1). Note that each new simulation is independent and starts with an empty simulation box. Method A and B are compared in Section 2.3.1 to discuss their equivalence.

2.2.2 Resistor network model

The effective conductivity of the composite depends on many factors such as the fiber content, fiber distribution, fiber resistance, and the connection conditions between fibers. The resistivity of the box is determined by means of the traditional resistor network model [28, 55], and conductivity is determined as its reciprocal.

For a given percolated simulation box with N conductive fibers, its resistance along a

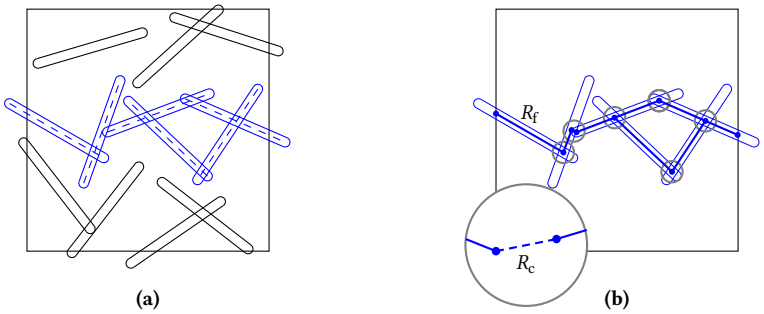

Fig. 2.5. A connected fiber network (a) is converted to an equivalent resistor network (b). We use R_f to represent resistance of fiber segments and R_c for contact resistance of two connected fibers.

coordinate axis direction is calculated by applying an electric potential difference between the two opposite box faces perpendicular to that direction and measuring the current flowing through the box along it. To this end, the simulation box is considered as a resistor network with each resistor representing either a fiber resistance or a contact resistance between two fibers. The resistance of a fiber segment is proportional to its length via

$$R_f = \varrho \frac{l}{S}, \tag{2.5}$$

where ϱ is the resistivity of the conductive fibers, and l and S are the fiber segment length and cross-sectional area, respectively. Each contact resistance R_c is given a constant value [33, 56].

The equivalent resistor network is constructed from the connected fiber cluster, as illustrated in Fig. 2.5. The procedure starts by generating junction nodes from the percolated fiber cluster (for each pair of connected fibers in the cluster, the two closest points on the respective axial line segments are converted to two nodes). A contact resistor element is then added between these two nodes, and each node is recorded on its host fiber. For each fiber in the percolated cluster, the segment between any two adjacent nodes is transformed into a fiber resistor element. We do not take into account all other fibers not connected with the percolated cluster. Finally, any intersection between a fiber in the cluster and the two opposite faces of interest on the simulation box is also converted into a junction node on the fiber. For the remaining surfaces, there is no current flowing through them and their intersection points with the fibers are ignored.

For a typical contact resistor or fiber resistor element e, defined from node a to b, the current I^e flowing through it is proportional to the nodal potential difference $U_a^e - U_b^e$ according to Ohm's law:

$$I^e = \frac{U_a^e - U_b^e}{R^e}, \tag{2.6}$$

where R^e is the resistance of the resistor element and e represents an arbitrary resistor element in the whole resistor network. If the current flowing out of the first (respectively second) node is denoted as I_a^e (respectively I_b^e), the elemental matrix form of Ohm's law is expressed as

$$\begin{bmatrix} I_a^e \\ I_b^e \end{bmatrix} = \frac{1}{R^e} \begin{bmatrix} 1 & -1 \\ -1 & 1 \end{bmatrix} \begin{bmatrix} U_a^e \\ U_b^e \end{bmatrix} \tag{2.7}$$

or, in index form,

$$I_i^e = K_{ij}^e U_j^e \tag{2.8}$$

where i and j takes on the value of either a or b. Now we use a global node numbering system (from 1 to n) to denote all the n nodes in the resistor network. Assembling Eq. (2.7) over all resistor elements yields the system of equations

$$\mathbf{KU} = \mathbf{I}, \tag{2.9}$$

where $\mathbf{U} = [U_1, U_2, ..., U_n]^{\mathrm{T}}$ stands for the nodal electric potential, $\mathbf{I} = [I_1, I_2, ..., I_n]^{\mathrm{T}}$ is the current flowing out of each node, and the global coefficient matrix $\mathbf{K}$ is expressed as

$$\mathbf{K} = \sum_{e=1}^{N_\mathrm{e}} K_{ij}^e, \tag{2.10}$$

where N_e is the number of resistor elements and the sum is to be understood as the assembly operator.

Kirchhoff's current law states that the sum of the currents flowing into a node is equal to the sum of the currents flowing out of that node. In our simulations, we do not apply current to the nodes (the right-hand side of Eq. (2.9) is therefore equal to zero). However, a potential difference ΔU is applied between nodes on two opposite boundary surfaces. By solving the system of linear equations (2.9), we obtain the electric potential on each node, and the current flowing through each element can be calculated according to Eq. (2.6). The total electrical current I_eff passing through the resistor network is determined by summing up the currents in the resistors directly connected to either of the opposite boundaries. The effective resistance R_eff of the simulation box (resistor network) is calculated by

$$R_\mathrm{eff} = \frac{\Delta U}{I_\mathrm{eff}}, \tag{2.11}$$

and hence the effective resistivity

$$\varrho_\mathrm{eff} = R_\mathrm{eff} \frac{A}{L}, \tag{2.12}$$

where A is the cross-sectional area of the box, and L is the length of the box side. The effective

conductivity of the simulation box

$$\sigma_{\text{eff}} = \frac{1}{\varrho_{\text{eff}}} = \frac{I_{\text{eff}} L}{\Delta U A} \tag{2.13}$$

is defined as the reciprocal of the effective resistivity.

Finally, note that we generate n_c configurations and use the average of n_c conductivities as the conductivity of the simulation box containing N conductive fibers. The configuration number n_c is determined when the average and deviation of n_c conductivities tend to stabilize as n_c increases.

2.2.3 Effective ratio of active material

This section evaluates the active material utilization and electrode capacity. The active material is the source (or reservoir) of lithium and basically determines the capacity of the electrode. The active material is usually not fully exploited [22, 23] as indicated by the fact that the exerimentally-determined effective gravimetric capacity q_{eff} is typically smaller than the theoretical gravimetric capacity q_{th} of the active material. For example, for a fibrous lithium cobalt oxide ($LiCoO_2$)-based cathode, the experimetally-determined gravimetric capacity ranges from 114 to 128 mAh g^{-1} at 0.1 C-rate [15], while the theoretical (reversible) gravimetric capacity of $LiCoO_2$ is approximately 140 mAh g^{-1} [57]. Values between 89 and 137 mAh g^{-1} have also been reported in Ref. [24] for electrospun $LiCoO_2$ wires tested at 0.37 C-rate. These experimental results are affected by factors such as ionic diffusion in the electrolyte, lithium diffusion in the active material, electronic conductivity, and number of charge/discharge cycles. Here we focus on a single limiting factor: the active material access to electrons.

Recall that lithium insertion/extraction at the battery electrodes occurs through reactions that can be generalized as [58]

$$a\,\mathrm{A} + n\,e^- \leftrightarrows b\,\mathrm{B}, \tag{2.14a}$$

$$c\,\mathrm{C} - n\,e^- \leftrightarrows d\,\mathrm{D}, \tag{2.14b}$$

where a molecules of A take up n electrons e^- to form b molecules of B at one electrode (2.14a) and similarly at the other (2.14b). Equations (2.14a) and (2.14b) express the reduction and oxidation reaction, respectively, and they indicate that electrons are needed for the reaction to occur.

We define the active fibers as being effective in contributing to the capacity if they are connected to the percolated conductive fiber network. The connection criterion between an active fiber and a conductive fiber is the same as the one between conductive fibers in

Eq. (2.4). The total electrode effective capacity

$$C = q_{\text{th}}\, \rho_{\text{a}}\, V_{\text{a}}^{\text{eff}} \tag{2.15}$$

is expressed as a function of the volume $V_{\text{a}}^{\text{eff}}$ of effective active material, the mass density ρ_{a} of active material, and the theoretical gravimetric capacity q_{th} (mAh g^{-1}) of the active material. The effective gravimetric capacity

$$q_{\text{eff}} = \frac{C}{\rho_{\text{a}}\, V_{\text{a}}} = q_{\text{th}}\, \frac{V_{\text{a}}^{\text{eff}}}{V_{\text{a}}} \tag{2.16}$$

is usually expressed in terms of unit mass of the electrode active material [58] with V_{a} the volume of total active material. We can then introduce the effective ratio

$$r = \frac{q_{\text{eff}}}{q_{\text{th}}} = \frac{V_{\text{a}}^{\text{eff}}}{V_{\text{a}}} \tag{2.17}$$

which ranges from 0 to 1 by definition.

Here we do not model the entire fiber-based electrode; instead, we study a cubic simulation box. In the box, all active fibers have the same size. The effective ratio can therefore be simplified as

$$r = \frac{N_{\text{a}}^{\text{eff}}}{N_{\text{a}}}, \tag{2.18}$$

where $N_{\text{a}}^{\text{eff}}$ is the number of effective active fibers connected to the conductive fiber network and N_{a} is the total number of active fibers.

Due to the soft-core assumption, existing fibers have no influence on the placement of a new fiber. Each active fiber has therefore the same probability of getting connected with the percolated conductive fiber network, if formed. Consequently, the effective ratio does not depend on the content of active fibers: it solely depends on the conductive fibers. The procedure to calculate the effective ratio for a given conductive fiber content is described next and more details are provided in 2.B.

We first generate a simulation box with N conductive fibers and N_{a} active fibers. The number of active fibers connected to the percolated conductive fiber network is counted as $N_{\text{a}}^{\text{eff}}$, and the effective ratio is calculated according to Eq. (2.18). In the case of no percolated conductive fiber network, the effective ratio is set to be 0. The effective ratio associated with this specific conductive fiber configuration has a definite value that corresponds to the theoretical probability; as more active fibers are included, the effective ratio calculated gets closer to this value, and, when converged, the corresponding number of active fibers is indicated by N_{a}. The effective ratio calculated in this fashion is valid for a single configuration with N conductive fibers.

We then generate n_c simulation boxes with the same number of conductive fibers but different spatial configurations and calculate their corresponding effective ratios. Finally, the average effective ratio of n_c different realizations is taken as the effective ratio for N conductive fibers. When no percolated conductive fiber network exists, a null effective ratio is considered towards the calculation of the average effective ratio. The box number n_c is identified when the average and deviation of n_c effective ratios tend to stabilize as n_c increases. By changing the number of conductive fibers, we repeat the procedure described above to correlate the effective ratio to the number N of conductive fibers.

2.3 Results and discussions

Carbon nanofibers with high electronic conductivity can be synthesized with diameter in the 100–200 nm range, length in the 5–20 µm range, and aspect ratio in the 10–500 range [10, 59]. Electrospun $LiCoO_2$ fibers can be produced with an average diameter of 80–100 nm [18]. In our simulation, active and conductive fibers have diameter $d = 100$ nm and length $l = 2.4$ µm. These values, consistent with those of the fibers produced by Showa Denko [59], have been chosen to obtain fibers with aspect ratio $l/d = 24$, which is the value reported in Ref. [43]. A simulation box size with edge length $L = 10$ µm, which is about five times (cf. 4–6 times used in Ref. [60]) larger than the fiber length, has been employed; the box size choice is also discussed in Section 2.3.1. For convenience, the edge length of the simulation box is set to one unit; the fibers are therefore scaled with respect to the box size: fiber length is $l = 0.24$ units and diameter $d = 0.01$ units. For the sake of conciseness, we omit "unit" when referring to these quantities in the following. Box size and fiber diameter will not change in the following apart from the discussion on aspect ratio effects.

In this section, we first evaluate the percolation threshold (Section 2.3.1) using two approaches and compare the results to reveal the connection between them. Although the electronic conductivity of isotropic fiber distributions has been extensively studied in the past [32, 42, 47], we show simulation results in Section 2.3.2 as the basis for the study of fiber orientation effects in Section 2.3.4. The electrode capacity is studied and results are reported in Section 2.3.3. In the first three sections, fibers are distributed isotropically. The results are used as a reference to study the effect of fiber orientation on percolation threshold, effective conductivity, and the effective ratio in Section 2.3.4.

2.3.1 Percolation threshold

Here we present results obtained with the two methods described in Section 2.2.1. The percolation probabilities obtained with method A for increasing numbers N of conductive fibers are indicated by the red circles in Fig. 2.6b. Each symbol represents the result of

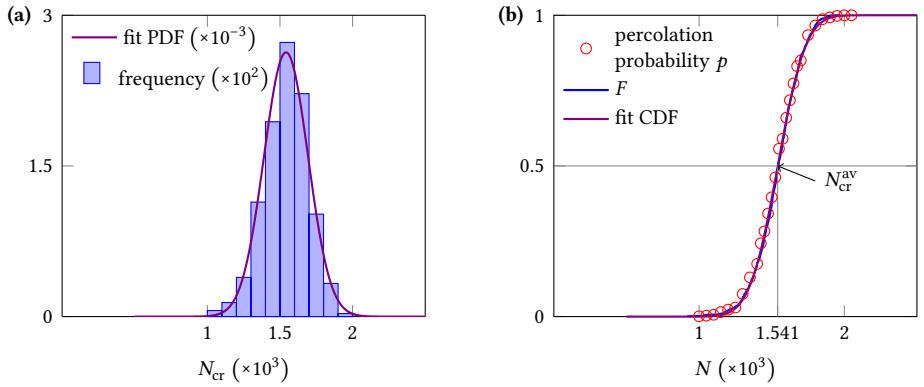

Fig. 2.6. Comparison of results between method A and B. Subfigure (a) shows histogram and fit (to normal distribution) probability density function of the 1000 critical fiber numbers N_{cr} from method B. Subfigure (b) shows the percolation probability at different conductive fiber numbers N from method A, the empirical cumulative probability $F(N)$ by Eq. (2.19), and the fit cumulative distribution function of the 1000 critical fiber numbers N_{cr} from method B.

$m_A = 1000$ conductive fiber configurations (with $m_A = 2000$ the difference is negligible). Method B is then employed and we identify $m_B = 1000$ critical fiber numbers N_{cr}. We then plot the histogram of the 1000 samples as shown in Fig. 2.6a and calculate the corresponding empirical cumulative distribution function

$$F(N) = \frac{\text{count of } N_{cr} \leq N}{m_B}, \tag{2.19}$$

where m_B is the total count of N_{cr} (blue line in Fig. 2.6b). By definition, $F(N)$ can be interpreted as the probability of $N_{cr} < N$. As suggested by the histogram and $F(N)$, the critical fiber number N_{cr} is likely to follow a normal distribution; hence, we fit the 1000 critical fiber numbers to a normal distribution (mean value of 1542 and standard deviation of 152 obtained for this specific case). The fit probability density function and the cumulative distribution function (CDF) are plotted in Fig. 2.6a and 2.6b, respectively. The perfect agreement between empirical and fit cumulative distributions confirms that fitting to the normal distribution is accurate (with $m_B = 2000$ the difference in average and deviation is negligible).

Figure 2.6b shows that the percolation probability plot (red circles, method A) agrees perfectly with the empirical cumulative distribution function (blue line, method B). This is because they are equivalent from the statistical point of view. The cumulative probability of $N_{cr} \leq N$ has exactly the same meaning as the percolation probability for N fibers: for m_B critical fiber numbers N_{cr}, trials of $N_{cr} \leq N$ in method B can be counted as successful percolation samples at the given fiber number N in method A, while trials of $N_{cr} > N$ can be viewed as samples not being percolated. The total number of trials m_B is intepreted as the

sample number m_A.

The average value N_{cr}^{av} of critical fiber numbers in method B is used as the percolation threshold in Refs. [32, 43]. This choice is reasonable since the statistical average is representative and easy to calculate. Method A is used in Refs. [51–54, 61], where the fiber number with 0.5 percolation probability was taken as the percolation threshold, but different arguments are provided by the authors to support their choices. For example, Chen et al. [51] show that this value leads to the best agreement with experiments, while Schilling et al. [52] refer to a previous study about percolation transition in fluids where it was shown that there exists a common crossing point between curves obtained for different box sizes at a percolation probability just below 0.5 [62]. Nevertheless, from the comparison with method B, we now provide statistical insights into the 0.5 percolation probability. As can be seen from the probability density function and the cumulative distribution function in Fig. 2.6, the average N_{cr}^{av} corresponds to the cumulative probability of 0.5 in method B, namely the percolation probability of 0.5 in method A (see equivalence in previous paragraph). In other words, if we randomly insert N_{cr}^{av} conductive fibers in the simulation box, the percolation probability is 0.5. The equivalence provides a new understanding behind the choice of the fiber number with 0.5 percolation probability as the percolation threshold for method A: it corresponds to the statistical average.

In Fig. 2.6, the sample number m_B in method B is the same as the number m_A of runs to get a single red circle point in method A, and calculating all the data points in method A is a trial-and-error process. In terms of the computational burden, method B is advantageous and is hence employed in this study. Nevertheless, the application of method B is restricted to the RSA algorithm and is not applicable to other approaches (*e.g.*, Metropolis Monte Carlo algorithm [63]). Method A is therefore more versatile and can be used irrespective of the fiber generation method.

The percolation threshold in terms of volume fraction (i.e., the average critical fiber volume fraction) can be expressed as

$$\phi_{cr}^{av} = \frac{N_{cr}^{av} \pi l d^2}{4L^3} \tag{2.20}$$

according to Eq. (2.3). From now on we shall omit the superscript "av" in the notation of the average percolation threshold.

The cumulative probability curve in Fig. 2.6b shows a gradual transition from 0 to 1, due to the finite size of the simulation box. The width of the transition zone is characterized by the deviation of variable N_{cr} according to statistics. Fig. 2.7 shows the transition zone becomes steeper and steeper as the box size increases, i.e., the deviation of N_{cr} decreases and the distribution of N_{cr} concentrates more and more on its mean value—the percolation threshold. In the limit of an infinite box, the transition curve tends to a step function.

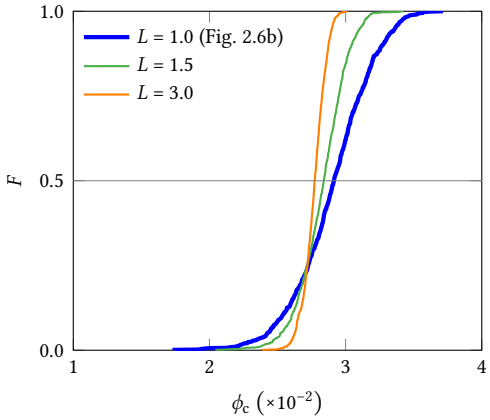

Fig. 2.7. Empirical cumulative distribution function F at different box sizes L as a function of the conductive fiber volume fraction ϕ_c. The fiber size is kept fixed (length $l = 0.24$, diameter $d = 0.01$).

Figure 2.7 also shows that the average of N_{cr} (corresponding to $F(N) = 0.5$) decreases with the box size. According to the classic percolation theory [46, 64], the percolation threshold ϕ_{cr} of a finite-size box depends on the box size and follows the power law

$$(\phi_{cr} - \phi_{cr}^{\infty}) \propto L^{-c}, \tag{2.21}$$

where ϕ_{cr}^{∞} is the percolation threshold of an infinite system and c is a positive constant. In the main plot of Fig. 2.8, the percolation threshold ϕ_{cr} is shown for different edge lengths. It is found that $c = 1.59$ results in the best straight line fit of ϕ_{cr} against L^{-c} as shown in the inset plot, indicating the convergence of the percolation threshold to the asymptotic value of an infinite system. The power law relation can be used to extrapolate the asymptotic percolation threshold ϕ_{cr}^{∞}. In this case, the linear fit (inset diagram) gives $\phi_{cr}^{\infty} = 0.0274$, which is about 5% lower than the maximum value of 0.0291 for the smallest box ($L = 1.0$).

To validate our simulation results, the percolation threshold is shown as a function of the aspect ratio of the conductive fibers in Fig. 2.9. The percolation thresholds (blue circles) are calculated from the average critical fiber number via Eq. (2.20) and the aspect ratio is changed by varying the diameter of the conductive fibers while keeping the box edge length equal to 1 and fiber length equal to 0.24. The plot marked with triangles are the critical volume fractions obtained from the simulation of three-dimensional systems with randomly oriented soft-core sticks in Ref. [32]; the remaining plots with squares and diamonds are experimental and simulated results for isotropic silver nanowire-polystyrene composites in Ref. [65]. It can been seen that our simulation results agree well with these results and the

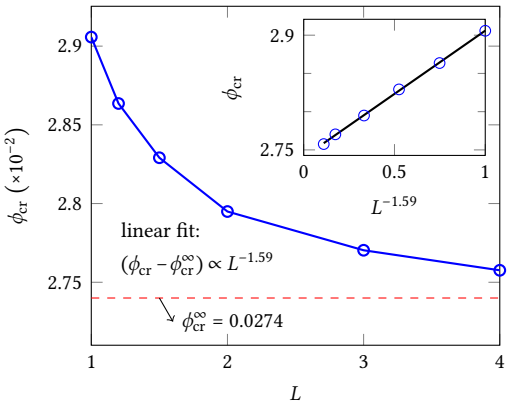

Fig. 2.8. Percolation threshold ϕ_{cr} (average critical fiber volume fraction) versus the simulation box size L. The power law fit of ϕ_{cr} against the box size gives the critical fiber volume fraction of an infinite box ϕ_{cr}^{∞}.

results can be fit using the power law

$$\phi_{cr} = c_0 \left(\frac{l}{d}\right)^{-c_1} \tag{2.22}$$

with $c_0 = 0.6621$ and $c_1 = 1$. The exponent $c_1 = 1$ indicates an inversely proportional relation between ϕ_{cr} and the aspect ratio l/d. This inverse relation is also theoretically derived in Ref. [32] and the author obtained a constant $c_0 = 0.6$

Our simulation results in Fig. 2.9 are obtained with $L = 1.0$. Given the good agreement with published data, the relative error introduced by the finite box size (5% in Fig. 2.8) is acceptable. We have therefore used a unit size simulation box in the following simulations.

The percolation threshold discussed in this section is measured along one direction (x direction), but we have also checked the other two directions and found that there basically is no difference between them for the isotropic fiber distribution case. This can also be seen in Fig. 2.18: the percolation threshold calculated along x and y directions coincide in the isotropic state when $\theta_m = 90°$ in case I and $\theta_m = 0°$ in case II. Same arguments hold for conductivity and effective ratio.

2.3.2 Effective conductivity

Next we show the effective conductivity determined by the resistor network model at different conductive fiber volume fractions; the results here are obtained under the isotropic distribution and, together with Fig. 2.19, provide a reference for conductivities when constraints on fiber orientation apply. For convenience, we assume that the contact resistance R_c between

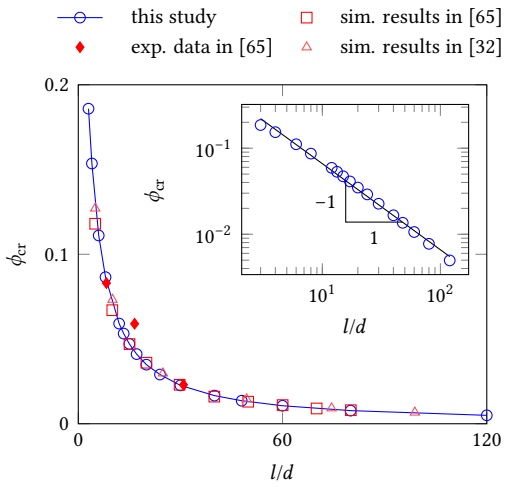

Fig. 2.9. The main plot shows the percolation threshold ϕ_{cr} versus the aspect ratio l/d and a good agreement between our simulation results and results from references. The inset diagram presents the percolation threshold against the aspect ratio in logarithmic scale and a linear fit of the data points suggesting a power law dependence of the percolation threshold on the effect ratio.

any two connected fibers is a constant value (this has been suggested in Refs. [33, 56]). The fiber segment resistance R_f is proportional to the length of the segment (2.5). We perform our simulations with $\varrho/S = 1\ \Omega/\text{unit}$ and choose $R_c = 1.5\ \text{k}\Omega$ so that the contact resistance R_c is much higher than the fiber resistance R_f (this assumption is in agreement with Refs. [28, 33, 56]). The effective conductivity calculated via Eq. (2.13) is then normalized using the contact resistance:

$$\sigma_N = \sigma_{eff} R_c. \tag{2.23}$$

A potential difference of $\Delta U = 1\text{V}$ is applied between nodes on the left- and right-hand surfaces (both surfaces are perpendicular to the x direction in Fig. 2.1). Figure 2.10 shows the electric potential maps for different fiber distributions. The electric potential increases linearly from the left- to the right-hand side surface, suggesting a well dispersed fiber network.

Figure 2.11 shows the conductivity at different conductive fiber volume fractions. For each volume fraction value, the simulation is repeated 100 times and the average conductivity is used (no significant differences are observed in the average value with more simulation runs). It is shown that the conductivity increases exponentially with the volume fraction. The inset diagram is a log-log plot of the normalized conductivity σ_N as a function of the volume fraction of conductive fibers reduced by the percolation threshold. The data points can be fit by a straight line, excluding the first two points, thus suggesting a power law

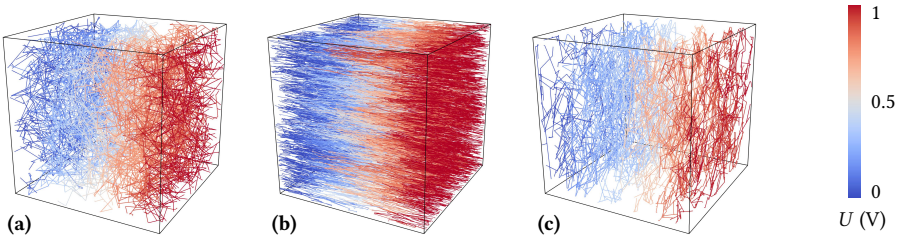

Fig. 2.10. Electric potential distribution of the equivalent resistor network for (a) scenario A (isotropic fiber distribution), (b) scenario B (fibers aligned along the x direction), and (c) scenario C (fibers perpendicular to the x direction) as described in Section 2.2. The potential of all nodes on the left surface is set to zero, while an electric potential equal to 1 V is applied to all nodes on the right surface.

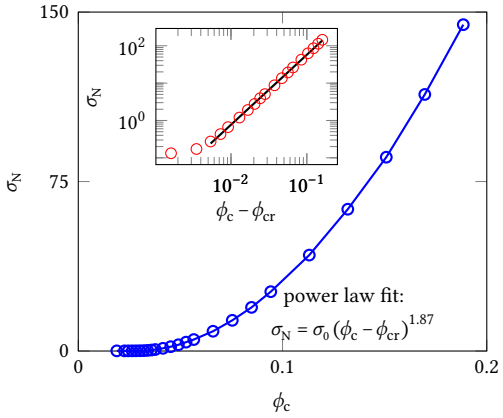

Fig. 2.11. The main plot shows the normalized conductivity $\sigma_N = \sigma_{eff} R_c$ against conductive fiber volume fraction ϕ_c. In the inset plot, the relation between σ_N and $\phi_c - \phi_{cr}$ is shown in logarithmic scale and the linear fit indicates a power law dependence of σ_N on $\phi_c - \phi_{cr}$ (ϕ_{cr} is the percolation threshold).

dependence of the conductivity on the difference between the volume fraction ϕ_c and the percolation threshold ϕ_{cr} of the type

$$\sigma_N = \sigma_0(\phi_c - \phi_{cr})^{\alpha}, \tag{2.24}$$

where $\sigma_0 = 4343.91$ and $\alpha = 1.87$ for this example. Equation (2.24) is a generally accepted form of dependency of the conductivity on the volume fraction of conductive fibers, and the exponent 1.87 agrees well with values (around 2) reported in the literature [32, 42, 47].

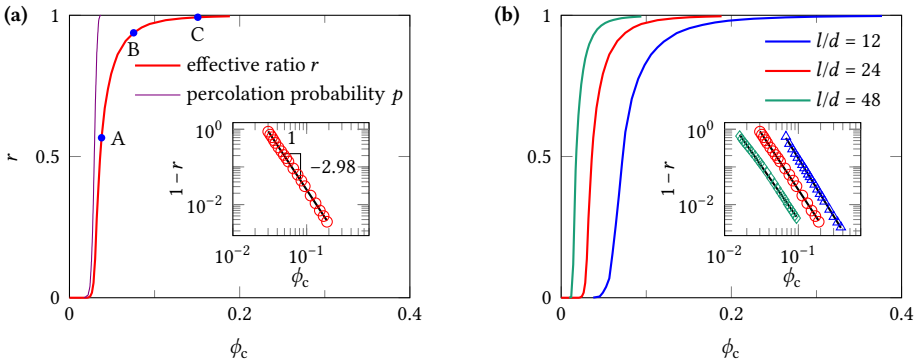

Fig. 2.12. (a) The main plot shows the effective ratio r versus the conductive fiber volume fraction ϕ_c and the percolation threshold. The inset graph presents data relating $1 - r$ to ϕ_c, and the linear fit indicates a power law relation between r and ϕ_c. Conductive and active fibers have the same size and their aspect ratios l/d are 24. Marks A, B, and C refer to the conductive fiber volume fractions in Fig. 2.20. (b) The main plot shows the effective ratio r at two more aspect ratios (12 and 48). The inset diagram also presents the data in a logarithmic scale and the linear fits suggest a power law dependence of the effective ratio on the conductive fiber volume fraction at different aspect ratios.

2.3.3 Effective active material and capacity

The percolation threshold and conductivity evaluation discussed in the previous sections only involved conductive fibers. In this section, the active fibers and their interaction with the conductive fibers will be studied for electrode capacity evaluation. To this end, we first start with results related to the utilization of the active material (effective ratio of active fibers).

Effective ratio of active fibers

Figure 2.12a shows the effective ratio and the percolation probability curves as function of the conductive fiber volume fraction. The percolation probability curve is steeper than the effective ratio curve and divides the diagram into two regions: below the percolation threshold (on the left-hand side of the percolation probability curve) the effective ratio is zero because of the absence of a percolated conductive fiber network; above the percolation threshold, the effective ratio increases sharply with the conductive fiber volume fraction. Here the effective ratio is computed as the average value of $n_c = 100$ different conductive fiber configurations, and for each configuration more than $N_a = 10000$ active fibers are used.

Figure 2.9 shows that the percolation threshold depends on the aspect ratio. Likewise, the aspect ratio affects the effective ratio in Fig. 2.12b. Here the aspect ratio l/d is changed by varying the fiber diameter d while keeping the fiber length l unchanged (active and conductive fibers have the same size). The higher the aspect ratio, the lower the conductive

fiber volume fraction around which the sharp increase of effective ratio occurs. This is consistent with higher aspect ratio fibers resulting into a smaller percolation threshold.

The effective ratio is influenced by the relative size of active and conductive fibers (Fig. 2.13). This is demonstrated by 1) changing the lengths of all active fibers ($l_a = 2\,l_c$ and $l_a = 0.5\,l_c$) while keeping their diameters fixed, and 2) by changing the diameters of all active fibers ($d_a = 1.5\,d_c$ and $d_a = 0.5\,d_c$) while keeping their lengths fixed, where the subscripts a and c indicate active an conductive fibers, respectively. The four cases are compared with the reference case in which the active and conductive fibers have the same length and diameter. It is found that the larger (either in length and diameter) the active fiber, the higher the effective ratio. In other words, for an assigned conductive fiber volume fraction, bigger active fibers should be preferred to increase the effective ratio and, consequently, the electrode capacity.

These predictions contrast with the usually observed electrode performance enhancement associated with dimension reduction of active materials [66]. The reason is that the appropriateness of our conclusions is subordinate to the validity of the soft-core assumption and to the suitability of the criteria used to discern if the active fibers are effective or not (the active fiber-conductive fiber network connection is described in Section 2.2.3). In particular, our predictions are suitable for electrodes composed by nanofibers and undergoing quasi-static charge/discharge processes. Under these conditions the solid-state diffusion in the active fibers is not a rate-limiting factor, and the fiber dimensions can be increased as long as concentration gradients inside the fibers remain negligible. The lithium insertion/extraction into/from the active fibers is thus guaranteed if they are accessible to electrons.

In general, electronic and ionic pathways must form continuous interconnections between all the regions of the battery, so that electrons and ions can reach the same place in the active electrode material at the same moment [22]. The description of transport processes in active material and electrolyte is required to determine if such pathways exist, and it is crucial to evaluate the effective capacity when processes occur at finite rates. To the best of our knowledge, however, numerical tools that allow to perform simulations of porous electrodes made up by large fiber ensembles are currently unavailable. For this reason, we use the simplified approach described in Section 2.2.3 and draw conclusions that are suitable for quasi-static and low-rate loading conditions.

When the active and conductive fibers have the same size, the inset curves in Fig. 2.12 suggest the power law relationship

$$r = 1 - a\phi_c^b \tag{2.25}$$

between effective ratio r and conductive fiber volume fraction ϕ_c (only valid when $\phi_c > \phi_{cr}$). The average relative error, considering all data points, is around 1% for all the three aspect

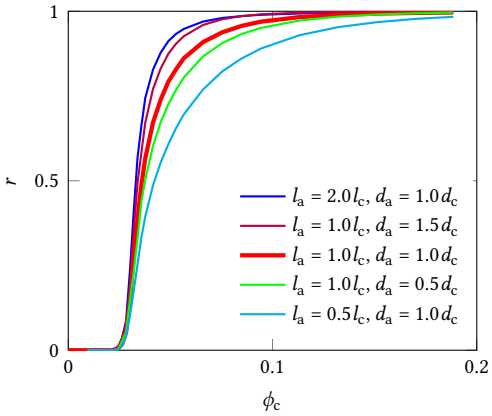

Fig. 2.13. Effective ratios r versus conductive fiber volume fraction ϕ_c when active fibers and conductive fibers have different sizes. The length (diameter) of active fibers and conductive fibers are denoted by l_a (d_a) and l_c (d_c), respectively.

ratios. When active and conductive fibers have different lengths or diameters (Fig. 2.13), the power law relation fails to fit the effective ratio curve with an average relative error larger than 10%. The error mainly originates from the wide discrepancy between the fit values and simulated results at conductive fiber volume fractions slightly above the percolation threshold.

Volumetric and gravimetric capacities

In electrode design, a certain volume fraction should always be dedicated to the electrolyte ϕ_e (see relation (2.2)). When solid polymer electrolytes (SPEs) are used, they provide conductive paths for lithium ions and structural support. Since SPEs are usually characterized by poor ionic conductivity [67], high volume fractions of fibers might not be an optimal design choice as the paths for ions moving in the electrolyte become entangled and the distance for ions to cover becomes longer, thus reducing the performance of the battery. If the electrolyte is liquid, a polymer binder might be needed to ensure the structural integrity of the electrode [23, 26]; both liquid electrolyte and polymer binder however limit the volume available for active and conductive materials. In view of these considerations, we evaluate the capacity of the electrode with a fixed electrolyte volume fraction ϕ_e. This constraint leads to a fixed total volume fraction of the two fiber species,

$$\phi_t = \phi_a + \phi_c = 1 - \phi_e \tag{2.26}$$

which takes a value between 0 and 1.

The expression of the effective capacity in Eq. (2.16) takes into account only the mass

of the active material, neglecting battery components such as polymer binders, electronic conductivity enhancers, and electrolyte [68]. Nevertheless, these inactive materials contribute to the overall electrode performance in terms of mass, volume, and overall electrochemical response [23, 26]. For this reason, it seems appropriate to divide the total electrode effective capacity (Eq. (2.15)) by the volume or mass of the entire electrode to define effective volumetric capacity

$$q_{\text{vol}}^{\text{eff}} = \frac{C}{V} = q_{\text{th}}\, \rho_{\text{a}}\, \phi_{\text{a}}^{\text{eff}} = q_{\text{th}}\, \rho_{\text{a}}\, (\phi_{\text{t}} - \phi_{\text{c}})\, r \tag{2.27}$$

and effective gravimetric capacity

$$q_{\text{gra}}^{\text{eff}} = \frac{C}{\rho_{\text{a}} V_{\text{a}} + \rho_{\text{c}} V_{\text{c}} + \rho_{\text{e}} V_{\text{e}}} = \frac{q_{\text{th}}\, \rho_{\text{a}}\, (\phi_{\text{t}} - \phi_{\text{c}})\, r}{\rho_{\text{e}} + (\rho_{\text{a}} - \rho_{\text{e}})\, \phi_{\text{t}} - (\rho_{\text{a}} - \rho_{\text{c}})\, \phi_{\text{c}}}, \tag{2.28}$$

where $\rho_{\text{a}} V_{\text{a}} + \rho_{\text{c}} V_{\text{c}} + \rho_{\text{e}} V_{\text{e}}$ is the total electrode mass (i.e., the sum of mass density multiplied by the volumes of active material, conductive material, and electrolyte), and

$$\phi_{\text{a}}^{\text{eff}} = \frac{V_{\text{a}}^{\text{eff}}}{V} = \frac{V_{\text{a}}}{V}\, r = \phi_{\text{a}}\, r = (\phi_{\text{t}} - \phi_{\text{c}})\, r \tag{2.29}$$

is the volume fraction of the effective active material, obtained considering the definition of its volume from (2.17).

Definitions (2.27) and (2.28) show that, for a specific set of material properties and a given total fiber content ϕ_{t}, the volumetric and gravimetric capacities depend on the conductive fiber volume fraction ϕ_{c} and on the effective ratio r; since r is actually a function of ϕ_{c} (Fig. 2.12a), the conductive fiber volume fraction ϕ_{c} is the only design variable, and these capacities depends on it in a nonlinear fashion. To illustrate the actual dependency, we consider two electrode designs that differ for the choice of the active material ($LiCoO_2$ and lithium iron phosphate ($LiFePO_4$)). The properties of $LiCoO_2$ [15, 24, 69] and $LiFePO_4$ [70, 71], together with those of vapor grown carbon fibers (VGCFs) forming the conductive network and the solid polymer electrolyte embedding both families of fibers are listed in Table 2.1.

Figure 2.14 shows the volumetric and gravimetric capacities for the two active materials at two total fiber volume fractions. Since $q_{\text{th}}\, \rho_{\text{a}}$ is larger for $LiCoO_2$ than for $LiFePO_4$ (see Table 2.1), the volumetric capacity $q_{\text{vol}}^{\text{eff}}$ for $LiCoO_2$ is always larger than that for $LiFePO_4$. The scenario is however different for the gravimetric capacity $q_{\text{gra}}^{\text{eff}}$: at $\phi_{\text{t}} = 0.188$, $q_{\text{gra}}^{\text{eff}}$ is higher for $LiCoO_2$ than for $LiFePO_4$, while the opposite happens at a higher fiber content $\phi_{\text{t}} = 0.471$. These observations indicate that electrode design optimization depends not only on the targeted capacity ($q_{\text{vol}}^{\text{eff}}$ or $q_{\text{gra}}^{\text{eff}}$) but also on the combination of geometrical features and material parameters of both active and inactive components.

The maximum capacity that the composite electrode can achieve is identified by the peak point of the capacity plot in Fig. 2.14, and the conductive fiber volume fraction related to

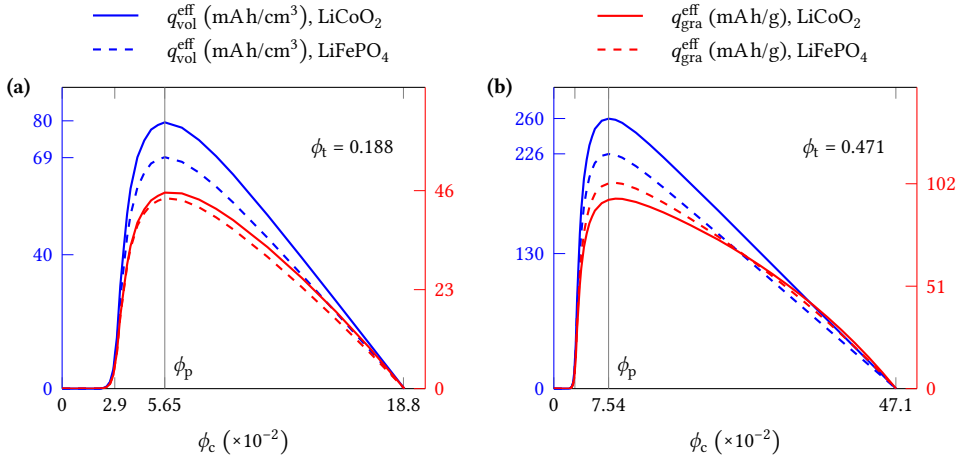

Fig. 2.14. Volumetric capacity q_{vol}^{eff} (Eq. (2.27)) and gravimetric capacity q_{gra}^{eff} (Eq. (2.28)) versus conductive fiber volume fraction ϕ_c at total fiber volume fraction $\phi_t = 0.188$ (a) and 0.471 (b). The optimal conductive fiber volume fraction ϕ_p corresponds to the maximum capacity. The effective ratio r is from Fig. 2.12a at aspect ratio 24. Solid lines denote $LiCoO_2$, while dashed lines are $LiFePO_4$. Material parameters of active materials, conductive materials, and solid polymer electrolyte can be found in Table 2.1.

it is defined as the optimal conductive fiber volume fraction ϕ_p. This quantity is another critical parameter to consider in electrode design, in addition to the percolation threshold ϕ_{cr}. Figure 2.14 shows that while ϕ_p differs for different total fiber contents ϕ_t, it is almost the same at a given ϕ_t for q_{vol}^{eff} and q_{gra}^{eff} (the position of the peak differs by 0.6% at most in terms of the capacity) and is independent of the active material considered.

We now study how ϕ_p changes with the total fiber content ϕ_t. Here we focus on cases in which lengths and diameters of active fibers are equal to those of the conductive fibers and consider three aspect ratios ($l/d = 12,\ 24,\ 48$). At each aspect ratio, the effective ratio r is approximated by Eq. (2.25) with the parameters obtained by fitting the corresponding curve in Fig. 2.12b. Finally, we determine ϕ_p by equating to zero the derivative of expression (2.27) with respect to ϕ_c (details can be found in 2.C). Using this method, we can plot ϕ_p as a function of the total fiber volume fraction (varied in the interval $[0.1,\ 0.9]$) as shown in Fig. 2.15a. The corresponding capacities q_{vol}^{eff} and q_{gra}^{eff} are then calculated from Eqs. (2.27) and (2.28) for $LiCoO_2$ (Fig. 2.15b). As ϕ_t increases, the optimal conductive fiber volume fraction ϕ_p grows and the increase is more drastic at a lower aspect ratio: ϕ_p ranges between 0.07 and 0.14 for $l/d = 12$, between 0.05 and 0.09 for $l/d = 24$, and between 0.03 and 0.05 for $l/d = 48$. The percolation thresholds ϕ_{cr} are also shown here in the same color as ϕ_p. The higher the aspect ratio, the lower ϕ_{cr} and the lower ϕ_p. The volumetric capacity increases with ϕ_t in an approximately linear fashion, while the gravimetric capacity rises sharply at small values of ϕ_t and then grows gently with ϕ_t. We can also see that at a higher aspect

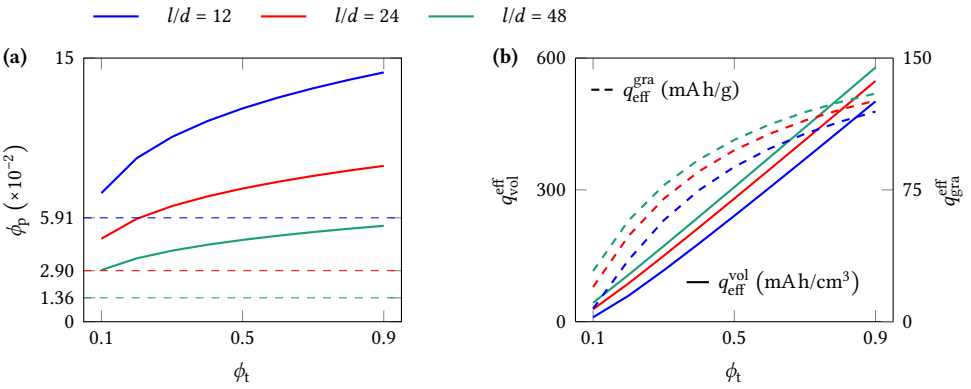

Fig. 2.15. Optimal conductive fiber volume fraction ϕ_p (a) and the volumetric capacity q_{vol}^{eff} and gravimetric capacity q_{gra}^{eff} (b) versus total fiber volume fraction ϕ_t at three different aspect ratios l/d. The dashed horizontal line in (a) denotes the percolation threshold ϕ_{cr}. Material parameters for the active material ($LiCoO_2$), conductive material, and solid polymer electrolyte can be found in Table 2.1.

ratio, the capacities q_{vol}^{eff} and q_{gra}^{eff} are larger. Section 2.3.3 completes the discussion of these results.

Comparison with particle-based electrodes

Here we provide a qualitative comparison between our numerical predictions of fiber-based electrodes and experimental studies of particle-based electrodes. Guzmán et al. [26] experimentally investigated the role of active-conductive material weight ratio on the performance (e.g., capacity at different charge/discharge rates and mechanical integrity) of particle-based electrodes. $LiFePO_4$ and carbon Super P were used as active and conductive material, respectively. The authors considered active-conductive material weight ratios in the range between 74/26 and 94/6, and they observed that the electrode performance was maximized with the 86/14 ratio. We assume the active material $LiFePO_4$ in fiber form and use VGCFs that better fit in our computational model. To perform a qualitative comparison between our predictions and the results by Guzmán et al. [26], we employ the active-conductive weight ratio defined as

$$\frac{M_a}{M_c} = \frac{V_a\,\rho_a}{V_c\,\rho_c} = \frac{(\phi_t - \phi_p)\,\rho_a}{\phi_p\,\rho_c}\,, \tag{2.30}$$

where ϕ_p is the optimal conductive fiber volume fraction for a given total fiber content ϕ_t as described in Section 2.3.3, and ρ_a and ρ_c are the densities of the active material $LiFePO_4$ and conductive VGCFs, respectively.

Figure 2.16 shows the active-conductive material weight ratio corresponding to the optimal conductive fiber volume fraction in Fig. 2.15a as a function of the total fiber content at three fiber aspect ratios (length and diameter are the same for all fibers). The active-

Table 2.1. Material parameters.

Component	Material	Symbol	Quantity	Reference	Value
active fibers	$LiCoO_2$	q_{LiCoO_2}	gravimetric capacity[a]	[57]	140.0 mA h/g
		ρ_{LiCoO_2}	density	[72]	5.0 g/cm^3
	$LiFePO_4$	q_{LiFePO_4}	gravimetric capacity	[73]	169.0 mA h/g
		ρ_{LiFePO_4}	density	[73]	3.6 g/cm^3
conductive fibers	VGCF	ρ_{VGCF}	density	[59, 74]	2.0 g/cm^3
electrolyte	1 M salt, SPE	ρ_{SPE}	density	[75]	1.2 g/cm^3

[a] This value refers to the reversible capacity only.

conductive weight ratio monotonically increases with ϕ_t and, for increasingly higher aspect ratios, the curves shift upwards and their slopes become steeper. Since the optimal conductive fiber volume fraction depends less and less on the total fiber content when the aspect ratio increases—Fig. 2.15a shows that the total variation of ϕ_p with ϕ_t reduces by a factor of three when the aspect ratio changes from 12 to 48—more active fibers can be introduced in the system. This follows from the progressive reduction of the percolation threshold with increasingly high aspect ratio, also showed in Fig. 2.15a. We observe that the active-conductive material weight ratio basically falls in the range of values explored by Guzmán et al. [26] (for particle-based electrodes) when the aspect ratio is equal to 12 and 24, providing a qualitative validation for our results. In addition, the total fiber content corresponding to the intersect between each curve and the optimal active-conductive weight ratio (86/14 according to Guzmán et al. [26]) progressively shifts from 0.15 to 0.55 when the aspect ratio changes from 48 to 12. Roughly speaking, since reduced active-conductive weight ratios are found for reduced aspect ratios, our results suggest that the more the geometry of fibers approaches that of particles, the smaller the optimal active-conductive weight ratio becomes. This is in agreement with common design practice of $LiFePO_4$-carbon Super P particle-based electrodes, as they are usually assembled with active-conductive material weight ratio ranging between 80/20 and 86/14 [26].

Practical application

We now show how the tools just described can be used to design fiber-based electrodes. To this end, we refer to the guidelines provided by the European Commission for batteries devoted to automotive applications [76]. The target is a battery cell with a volumetric energy density $E_v = 750$ W h/L and a gravimetric energy density $E_g = 350$ W h/kg. Estimates of the volumetric and gravimetric energy densities can be obtained by multiplying q_{vol}^{eff} and q_{gra}^{eff} (Fig. 2.15b) by the average electrode potential. With the purpose to provide an illustrative

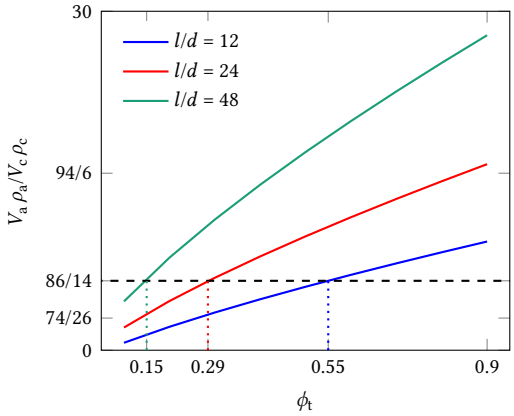

Fig. 2.16. Active ($LiFePO_4$)-conductive (VGCF) material weight ratio versus total fiber volume fraction ϕ_t at three different aspect ratios l/d. The optimal active-conductive material weight ratio for particle-based electrode making use of the same active material [26] is indicated by the dashed horizontal line.

example, we focus on a cell consisting of a $LiCoO_2$ fiber-based electrode and a lithium metal counter electrode. We consider an average potential of 3.8 V according to the data reported by Nitta et al. [57]. For simplicity, our evaluation is limited to the contribution of the fiber-based electrode (the contributions of the counter electrode and the separator on the overall cell volume, weight, and capacity should be considered in real applications). Figure 2.17 shows that in the worst case ($l/d = 12$) the targeted volumetric and gravimetric energy densities are obtained with ϕ_t equal to 0.43 and 0.54, respectively, and thus the higher fiber content allows to satisfy both criteria. The volume fraction that has to be dedicated to the conductive fibers (ϕ_p) is then determined from Fig. 2.15a and equals 0.11 and 0.12, respectively. The volume fraction occupied by the active fibers in the two configurations is determined from Eq. (2.26) (0.31 and 0.42, respectively). Figure 2.17 shows that when the aspect ratio increases, the fiber content needed to meet the targets reduces. Specifically, ϕ_t shifts to 0.34 and 0.40 for the volumetric and gravimetric energy density, respectively, when $l/d = 48$.

2.3.4 Effect of fiber orientation

This section studies the effect of fiber orientation on percolation threshold, effective conductivity, and effective ratio. We consider the two fiber distribution cases described in Section 2.2 and report results in the x and y directions. Results in the z direction are the same as those in the y direction because of the uniformly distributed azimuthal angle φ over the interval $[0, 360°]$ (this is also verified by results not reported here).

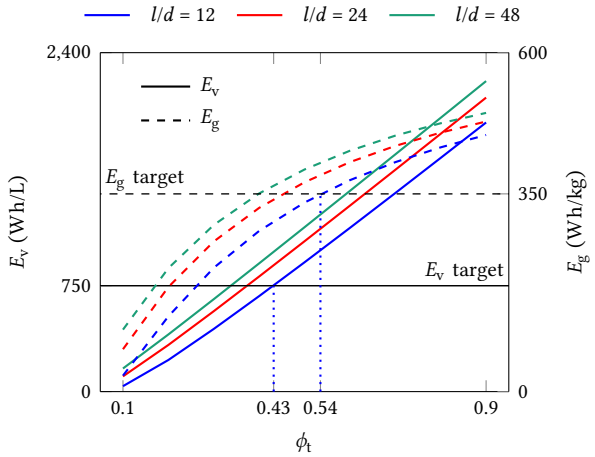

Fig. 2.17. Volumetric and gravimetric energy densities versus total fiber volume fraction ϕ_t at three different aspect ratios l/d. The two horizontal lines are the energy density targets provided by the European Commission for batteries in automotive applications [76].

On percolation threshold

Figure 2.18 shows the percolation threshold (average of $m_B = 1000$ samples) versus the limit angle θ_m for fiber distribution cases I and II. In both cases, the percolation threshold is smaller along the fiber alignment direction (x direction in case I, y direction in case II) than along directions perpendicular to it, irrespective of θ_m.

Figure 2.18a shows that the percolation thresholds in case I along the x and y directions decrease monotonically with θ_m and eventually converge to the same value, marked by the cross, for the isotropic distribution ($\theta_m = 90°$). For small θ_m values, the conductive fibers are basically aligned along the x direction and parallel to each other. Under these circumstances, a connected fiber network is unlikely to form along either the x or y direction. The maximum percolation threshold along the x direction at $\theta_m = 0$ is three times larger than the isotropic value (0.029), while the maximum percolation threshold along the y direction at $\theta_m = 5°$ is roughly nine times larger than the isotropic value. Although the percolation threshold along the x direction shows a minimum at $\theta_m = 70°$, its value is only 4% lower than the isotropic value. It is therefore safe to conclude that the percolation threshold along the x direction plateaus for $\theta_m > 45°$, without significant loss of accuracy.

In case II (Figure 2.18b), the percolation thresholds along the x and y directions start from the isotropic value and increase with θ_m. When $\theta_m = 90°$ (scenario C), all fibers are perpendicular to the x direction and isotropically distributed on planes parallel to the yoz plane. This situation prevents the conductive fibers to form a connected network and thus leads to a percolation threshold increase: the percolation threshold at $\theta_m = 85°$ in the x

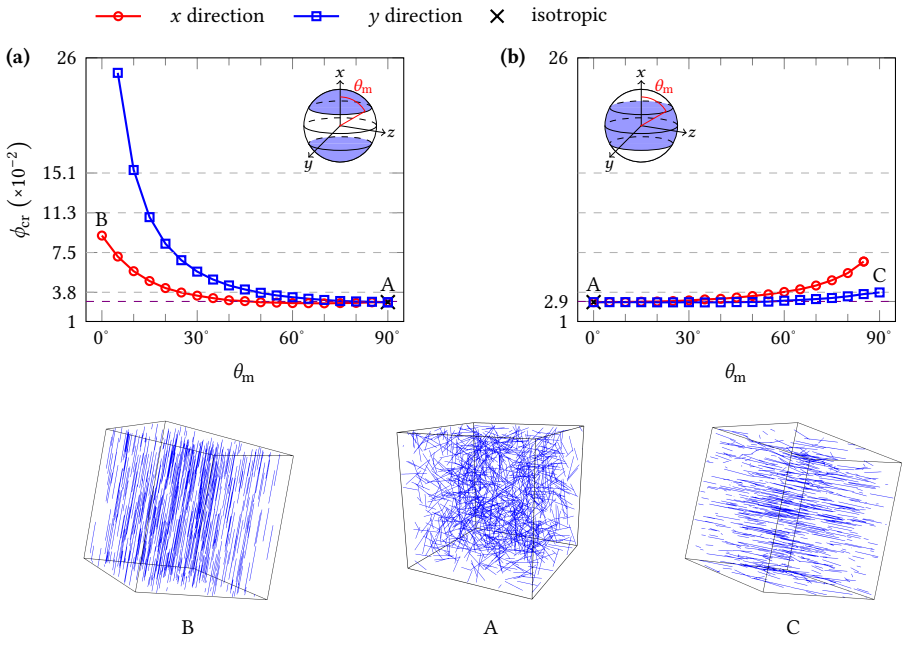

Fig. 2.18. Percolation threshold ϕ_{cr} versus limit angle θ_m with respect to the x axis for case I $0 < \theta < \theta_m$ (a) and case II $\theta_m < \theta < 90°$ (b). The crosses show the percolation threshold of the three-dimensional isotropic fiber distribution (the same in the x and y directions), and the isotropic values in (a) and (b) are the same. Dashed horizontal lines represent the isotropic percolation threshold (0.029) and the four conductive fiber volume fractions (0.0377, 0.0754, 0.1131, 0.1508) in Figs. 2.19 and 2.20. A, B, and C correspond to scenarios A, B, and C in Section 2.2 and Fig. 2.10, respectively.

direction is about two and half times larger than the isotropic value, while a 30% increase, compared to the isotropic value, is observed along the y direction.

We conclude that the percolation threshold is minimized at the isotropic fiber distribution. However, the percolation threshold change in case I is more pronounced than that in case II along both the x and y directions. In particular, when fibers are progressively constrained on planes perpendicular to the x direction (case II, Fig. 2.18b), the percolation threshold increase along the x direction is limited compared to the increase along the x direction when fibers are progressively aligned along the x direction (case I, Fig. 2.18a). A twofold and threefold increase is observed with respect to the isotropic value in the two cases, respectively. Furthermore, the percolation threshold increase along the x direction in case II is pronounced from $\theta_m > 40°$ onwards (Fig. 2.18b). This is relevant to fiber-based electrodes produced by electrospinning. As fibers are deposited on a substrate that can be identified with the yoz plane, our results suggest that it is beneficial to introduce some degree of randomness along the out-of-plane direction (x direction) for percolation in that direction.

In Fig. 2.18, the percolation thresholds along the x and y directions coincide when θ_m approaches 90° and 0° in case I and case II, respectively. This confirms that fibers are distributed uniformly and isotropically in the simulation box in these two limit cases, and that they are representative of the isotropic fiber distribution. As the isotropic values highlighted in Figs. 2.18a and b coincide, the isotropic distributions (scenario A) in case I and case II are (in average) equivalent. The same arguments hold for effective conductivity and effective ratio.

On effective conductivity

Figure 2.19 shows the effective conductivity against θ_m for case I and case II at three conductive fiber volume fractions (0.0754, 0.1131, and 0.1508). Here the conductivity is the normalized conductivity σ_N (Eq. (2.23)) divided by σ_{iso}, i.e., σ_N of the three-dimensional isotropic fiber distribution for each conductive fiber volume fraction.

In Fig. 2.19a, the conductivities along the x and y directions approach zero at small θ_m values (highly aligned fibers). This is because the percolation thresholds at small θ_m values (Fig. 2.18a) are higher than the conductive fiber content. As θ_m increases, the conductivity along the x direction increases and shows the existence of a maximum. This indicates that a certain degree of alignment improves the conductivity along the alignment direction (this is for instance beneficial to applications that only require unidirectional conduction). A higher degree of alignment seems to be preferable at higher conductive fiber content: the higher the fiber volume fraction, the smaller the limit angle θ_m to attain the maximum conductivity (θ_m shifts from 55° to 45° as the fiber volume fraction increases from 0.0754 to 0.1508). Moreover, the conductivity enhancement that can be achieved by aligning fibers along a specific direction is more appreciable at a higher fiber volume fraction, as suggested

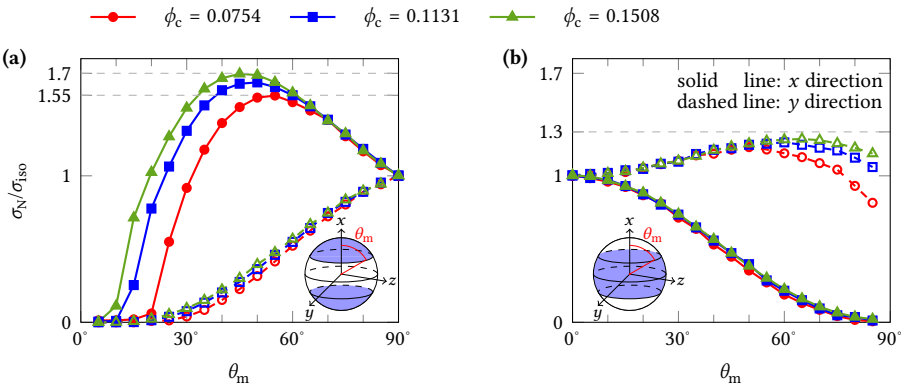

Fig. 2.19. Conductivity σ_N normalized by isotropic conductivities σ_{iso} versus limit angle θ_m with respect to the x axis for case I (a) and case II (b) at three different conductive fiber volume fractions ϕ_c. Note that σ_{iso} for the three conductive fiber volume fractions are different (Fig. 2.11). However, for each conductive fiber volume fraction, the isotropic conductivities σ_{iso} measured in the x and y directions are the same and the isotropic values in (a) and (b) are the same.

by the larger normalized conductivity (σ_N/σ_{iso} increases from 1.55 to 1.70 when the fiber volume fraction increases from 0.0754 to 0.1508). The peak value has also been observed in a two-dimensional setting [28, 77], and our results generalize that observation to a three-dimensional setting. The conductivity along the y direction increases monotonically with θ_m, and the variation patterns basically coincide for the three volume fractions. As θ_m increases to 90°, the conductivities along the x and y directions converge to the isotropic value.

For the second fiber distribution case (Fig. 2.19b), the conductivities along the x and y directions equal the isotropic value at $\theta_m = 0$. The conductivity along the y direction mirrors the trend of the conductivity along the x direction for case I in Fig. 2.19a: the conductivity improvement, compared to the isotropic value with the same conductive fiber content, is larger at a higher fiber volume fraction. For each conductive fiber volume fraction, the peak conductivity ($\sigma_N/\sigma_{iso} = 1.3$ at most) is smaller than the peak value in case I, suggesting that the fiber alignment effect is more pronounced when fibers are aligned along a specific direction (the x direction in case I) than fibers aligned along a random direction on a plane (the y direction is representative of any random direction on yoz plane in case II). However, the conductivity along the x direction decreases monotonically with θ_m, regardless of the fiber volume fraction. Since the electronic conduction in the electrode thickness direction (the x direction in case II) is crucial to battery rate performance [57], these observations suggest that the weaker the constraint on fiber orientation in electrospun fiber-based electrodes, the better the electrode performance.

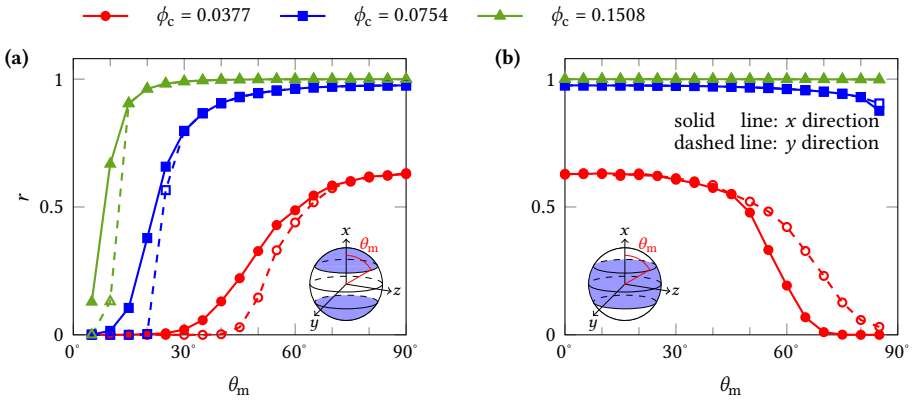

Fig. 2.20. Effective ratios r in the x and y directions versus limit angle θ_m with respect to the x axis at three different conductive fiber volume fractions ϕ_c for case I (a) and case II (b). For each conductive fiber volume fraction, the effective ratio for the three-dimensional isotropic distribution is calculated to be the same in the x and y directions, and the isotropic values in (a) and (b) are the same.

On the effective ratio

Fig. 2.20 shows the influence of fiber orientation on the effective ratio for three specific conductive fiber volume fractions—0.0377, 0.0754, and 0.1508, denoted by A, B, and C, respectively, in Fig. 2.12a. For non-isotropic fiber distributions, the effective ratio along the x direction is calculated by counting the active fibers connected with the percolated conductive fiber networks along the x direction, while the effective ratio along the y direction is defined as the fraction of the active fibers connected to percolated fiber networks along the y direction. Note that both fibers follow the same distribution in terms of fiber middle points and orientations.

In case I (Fig. 2.20a), the effective ratio increases from zero to the isotropic value at $\theta_m = 90°$; this holds true for both the x and y directions at each conductive fiber volume fraction. However, the transition starts at a larger θ_m value for the y direction, irrespective of the conductive fiber volume fraction. Since the percolation threshold along the x direction is always smaller than that along the y direction (Fig. 2.18a), the percolated fiber network will first form along the x direction as θ_m increases (percolation threshold decreases). The percolated cluster along the x direction is usually different from the one along the y direction and involves more fibers; this results in a higher effective ratio along the x direction. Above a certain value of the limit angle θ_m, the two percolated fiber clusters along the x and y directions merge into a bigger one, as indicated by the coincidence of effective ratios along the x and y directions. As a higher conductive fiber volume fraction meets the percolation threshold at a lower θ_m value (Fig. 2.18a), the transition of the effective ratio, either in the x or y directions, occurs at a smaller θ_m value; moreover, the transition of the effective ratio is

also sharper and the coincidence between the effective ratios in the x and y directions occurs earlier.

The arguments just exposed apply also to case II in Fig. 2.20b, with a few peculiarities. First, the plots in Fig. 2.20b appears mirrored compared to Fig. 2.20a, with r maximum at $\theta_m = 0°$ (isotropic value). Second, two of the three specific conductive fiber volume fractions are above the percolation threshold curves in Fig. 2.18b; for this reason also the trends of the corresponding effective ratios versus θ_m differ. Figure 2.18b shows that the conductive fiber volume fractions 0.0754 and 0.1508 are larger than the percolation threshold irrespective of θ_m (Fig. 2.18b), while the volume fraction 0.0377 exceeds the percolation threshold only for a limited interval of θ_m (above $\theta_m = 55°$ in the x direction, and above $\theta_m = 85°$ in the y direction). It follows that the effective ratios shown in Fig. 2.20b for $\phi_c = 0.0754$ and $\phi_c = 0.1508$ are basically constant and equal to the isotropic value along both x and y directions (apart from a 10% reduction for $\phi_c = 0.0754$ starting from $\theta_m = 50°$), while a transition from the isotropic value ($\theta_m = 0°$) towards a value that approaches zero ($\theta_m = 90°$) is clearly visible for $\phi_c = 0.0377$ (analogous to those observed in Fig. 2.20a).

Since the fraction of effective active fibers is subordinate to the presence of a percolated conductive fiber network, the impact of fiber orientation on the percolation threshold reflects on the effective ratio. The isotropic fiber distribution minimizes the percolation threshold and maximizes the effective ratio. At a given conductive fiber content, the larger the deviation from an isotropic distribution, the larger the reduction of the effective ratio. However, Figure 2.20 shows that the impact of fiber orientation reduces as the conductive fiber content increases. This means that the conductive fiber volume fraction that guarantees full utilization of the active material ($r = 1$, Fig. 2.12a) also makes the active material utilization insensible to fiber orientation constraints, thus providing an extremely useful information for fiber-based electrode design.

2.4 Conclusions

We have proposed a three-dimensional computational tool to estimate key effective properties (electronic percolation threshold, electronic conductivity, and capacity) of fiber-based electrodes. It is demonstrated that the percolation probability curve is equivalent to the cumulative distribution curve of the critical conductive fiber number (Fig. 2.6). The equivalence offers a statistically-rooted explanation that justifies the selection of the conductive fiber volume fraction with 0.5 percolation probability as the percolation threshold. Furthermore, we show that volumetric and gravimetric capacities (Fig. 2.14) are maximized at a specific (optimal) active-conductive material ratio. The corresponding optimal conductive fiber content is higher than the percolation threshold (Fig. 2.15); however, an excess of conductive

material lowers the capacities, in agreement with experimental studies performed on particle-based electrodes [26]. Since the electronic conductivity increases monotonically with the conductive fiber content (Fig. 2.11), we conclude that the trade-off between energy and power requirements, that is known to characterize particle-based electrode design, emerges also from our analysis on fiber-based electrodes.

Our results show that constraints on fiber orientation impact the effective properties. The isotropic fiber distribution leads to the lowest percolation threshold (Fig. 2.18) and to the highest active material utilization (effective ratio, Fig. 2.20) for a given conductive fiber content. Nevertheless, this does not apply to the electronic conductivity: the highest conductivity can be achieved in the direction along which fibers are aligned to a certain degree (the x direction in Fig. 2.19a, the y or z direction in Figs. 2.19b). We conclude that restrictions on fiber orientation must be considered for the design optimization of electrodes according to capacity (active material utilization) and power (electronic conductivity) requirements. Fiber orientation therefore represents an additional (compared to particle-based electrodes) degree of freedom in electrode design that can be exploited to strike a balance between electrode capacity and power density. In addition, the isotropic fiber distribution is significantly advantageous to active material utilization only when the conductive fiber content is small, while a limited effect on the active material utilization is observed at higher conductive fiber contents (Fig. 2.20). This suggests that when constraints on fiber orientation apply, the active materials utilization changes more drastically with the conductive fiber content. An interesting design question thus arises for applications where fiber orientation is constrained: can we still identify an optimal active-conductive fiber ratio to maximize the capacity when the total fiber content is fixed (similar to Fig. 2.14 for isotropic fiber distribution)?

These observations are of interest for electrospun fiber-based electrodes [3], where fibers are deposited on a substrate, and structural batteries [21], where preferential fiber orientations can be desirable to attain specific mechanical performance.

2.A Random fiber generation

(1) For a three-dimensional isotropic fiber distribution (scenario A), the polar angle θ is taken as

$$\theta = \cos^{-1}(1 - \text{rand}) \tag{2.31}$$

where rand represents a uniformly distributed random number in the interval [0, 1] (rand has the same meaning in the following).
(2) For a general fiber distribution in case I, we determine the polar angle θ by solving

$$1 - \cos\theta = (1 - \cos\theta_\text{m})\ \text{rand}, \tag{2.32}$$

where θ_m is between 0 and 90°. When $\theta_\text{m} = 90°$, Eq. (2.32) turns into (2.31).
(3) For a general fiber distribution in case II, the equation to solve for θ is

$$1 - \cos\theta = 1 - \cos\theta_\text{m} + \cos\theta_\text{m}\ \text{rand}, \tag{2.33}$$

where θ_m is between 0 and 90°. When $\theta_\text{m} = 0$, Eq. (2.33) turns into (2.31).

2.B Effective ratio determination

We claim that the effective ratio is independent of the active fiber content and only depends on the conductive fiber content. This is a consequence of the soft-core assumption: since fibers can overlap, the position of each fiber in the simulation box is independent from that of any other fiber. We verify this claim by means of the procedure reported below.

1. We generate a conductive fiber configuration with N fibers.
2. We generate n_a configurations by augmenting the conductive fiber configuration in step 1 with N_a active fibers.
3. The effective ratio for each of the n_a configurations is determined via Eq. (2.18); r indicates the average value of the n_a effective ratios.
4. We repeat steps 2–3 100 times changing the number N_a of active fibers. We find that, when n_a is large enough (1000 in our simulations), the average effective ratio values r are the same at different values of N_a. Therefore, for a fixed conductive fiber configuration, the effective ratio does not depend on the number N_a of active fibers.
5. We generate 100 configurations with N conductive fibers and repeat steps 2–4. For all the configurations the effective ratio does not depend on the specific number of active

fibers.

6. We further repeat all the previous steps for different numbers N of conductive fibers and obtained the same results.

As an alternative to the above procedure, for each conductive fiber configuration we suggest to use $N_a \geq 10000$ and $n_a = 1$ as done in Section 2.2.3.

2.C Peak capacity determination

As stated in Section 2.3.3, the optimal conductive fiber volume fractions ϕ_p for the volumetric and gravimetric capacities are almost the same. Here we just detail how to calculate ϕ_p for the volumetric capacity. When the effective ratio r in Eq. (2.27) is approximated by the power law fit (2.25) (this approximation is best suited when conductive and active fibers have the same size) we obtain that

$$q_{vol}^{eff} = q_{th}\ \rho_a\ (\phi_t - \phi_c)\ (1 - a\phi_c^b). \tag{2.34}$$

Taking the derivative of both sides with respect to ϕ_c gives

$$\frac{dq_{vol}^{eff}}{d\phi_c} = q_{th}\ \rho_a\ \left[a(b+1)\phi_c^b - ab\phi_t\phi_c^{b-1} - 1\right]. \tag{2.35}$$

The optimal conductive fiber volume fraction ϕ_p can be obtained by solving

$$\frac{dq_{vol}^{eff}}{d\phi_c} = 0. \tag{2.36}$$

References

[1] M. Zhuo, D. Grazioli, and A. Simone, *Active material utilization and capacity of fiber-based battery electrodes,* Electrochimica Acta **333**, 134929 (2020).

[2] X. Zhang, L. Ji, O. Toprakci, Y. Liang, and M. Alcoutlabi, *Electrospun Nanofiber-Based Anodes, Cathodes, and Separators for Advanced Lithium-Ion Batteries,* Polymer Reviews **51**, 239 (2011).

[3] J.-W. Jung, C.-L. Lee, S. Yu, and I.-D. Kim, *Electrospun nanofibers as a platform for advanced secondary batteries: A comprehensive review,* Journal of Materials Chemistry A **4**, 703 (2016).

[4] B. Zhang, F. Kang, J.-M. Tarascon, and J.-K. Kim, *Recent advances in electrospun carbon nanofibers and their application in electrochemical energy storage,* Progress in Materials Science **76**, 319 (2016).

[5] A. S. Arico, P. Bruce, B. Scrosati, J.-M. Tarascon, and W. Van Schalkwijk, *Nanostructured materials for advanced energy conversion and storage devices,* Nature Materials **4**, 366 (2005).

[6] W. Li, L. Zeng, Y. Wu, and Y. Yu, *Nanostructured electrode materials for lithium-ion and sodium-ion batteries via electrospinning,* Science China Materials **59**, 287 (2016).

[7] R. Fang, P. Farah, A. Popp, and W. A. Wall, *A monolithic, mortar-based interface coupling and solution scheme for finite element simulations of lithium-ion cells,* International Journal for Numerical Methods in Engineering **114**, 1411 (2018).

[8] S. Ahn, Y. Kim, K. J. Kim, T. H. Kim, H. Lee, and M. H. Kim, *Development of high capacity, high rate lithium ion batteries utilizing metal fiber conductive additives,* Journal of Power Sources **81**, 896 (1999).

[9] M.-S. Wu, J.-T. Lee, P.-C. J. Chiang, and J.-C. Lin, *Carbon-nanofiber composite electrodes for thin and flexible lithium-ion batteries,* Journal of Materials Science **42**, 259 (2007).

[10] C. Fongy, S. Jouanneau, D. Guyomard, and B. Lestriez, *Carbon nanofibers improve both the electronic and ionic contributions of the electrochemical performance of composite electrodes,* Journal of Power Sources **196**, 8494 (2011).

[11] I. Cho, J. Choi, K. Kim, M.-H. Ryou, and Y. M. Lee, *A comparative investigation of carbon black (Super-P) and vapor-grown carbon fibers (VGCFs) as conductive additives for lithium-ion battery cathodes,* RSC Advances **5**, 95073 (2015).

[12] B. N. Joshi, S. An, H. S. Jo, K. Y. Song, H. G. Park, S. Hwang, S. S. Al-Deyab, W. Y. Yoon, and S. S. Yoon, *Flexible, Freestanding, and Binder-free SnO_x-ZnO/Carbon Nanofiber Composites for Lithium Ion Battery Anodes,* ACS Applied Materials & Interfaces **8**, 9446 (2016).

[13] E. C. Self, R. Wycisk, and P. N. Pintauro, *Electrospun titania-based fibers for high areal capacity Li-ion battery anodes,* Journal of Power Sources **282**, 187 (2015).

[14] D. Damien, G. S. Anjusree, A. Sreekumaran Nair, and M. M. Shaijumon, *TiO_2 fibre/particle nanohybrids as efficient anodes for lithium-ion batteries,* RSC Advances **6**, 45802 (2016).

[15] E. C. Self, E. C. McRen, R. Wycisk, and P. N. Pintauro, *$LiCoO_2$-Based Fiber Cathodes for Electrospun Full Cell Li-ion Batteries,* Electrochimica Acta **214**, 139 (2016).

[16] N. Arun, V. Aravindan, S. Jayaraman, N. Shubha, W. C. Ling, S. Ramakrishna, and S. Madhavi, *Exceptional performance of a high voltage spinel $LiNi_{0.5}Mn_{1.5}O_4$ cathode in all one dimensional architectures with an anatase TiO_2 anode by electrospinning,* Nanoscale **6**, 8926 (2014).

[17] S. Jayaraman, V. Aravindan, P. Suresh Kumar, W. Chui Ling, S. Ramakrishna, and S. Madhavi, *Exceptional Performance of $TiNb_2O_7$ Anode in All One-Dimensional Architecture by Electrospinning,* ACS Applied Materials & Interfaces **6**, 8660 (2014).

[18] H.-W. Lu, L. Yu, W. Zeng, Y.-S. Li, and Z.-W. Fu, *Fabrication and Electrochemical Properties of Three-Dimensional Structure of $LiCoO_2$ Fibers,* Electrochemical and Solid-State Letters **11**, A140 (2008).

[19] Y. Gu, D. Chen, and X. Jiao, *Synthesis and Electrochemical Properties of Nanostructured $LiCoO_2$ Fibers as Cathode Materials for Lithium-Ion Batteries,* Journal of Physical Chemistry B **109**, 17901 (2005).

[20] E. S. Pampal, E. Stojanovska, B. Simon, and A. Kilic, *A review of nanofibrous structures in lithium ion batteries,* Journal of Power Sources **300**, 199 (2015).

[21] P. Liu, E. Sherman, and A. Jacobsen, *Design and fabrication of multifunctional structural batteries,* Journal of Power Sources **189**, 646 (2009).

[22] N. J. Dudney and J. Li, *Using all energy in a battery,* Science **347**, 131 (2015).

[23] H. Zheng, R. Yang, G. Liu, X. Song, and V. S. Battaglia, *Cooperation between Active Material, Polymeric Binder and Conductive Carbon Additive in Lithium Ion Battery Cathode,* Journal of Physical Chemistry C **116**, 4875 (2012).

[24] Y. Mizuno, E. Hosono, T. Saito, M. Okubo, D. Nishio-Hamane, K. Oh-ishi, T. Kudo, and H. Zhou, *Electrospinning Synthesis of Wire-Structured $LiCoO_2$ for Electrode Materials of High-Power Li-Ion Batteries,* Journal of Physical Chemistry C **116**, 10774 (2012).

[25] C. T. Cherian, J. Sundaramurthy, M. V. Reddy, P. Suresh Kumar, K. Mani, D. Pliszka, C. H. Sow, S. Ramakrishna, and B. V. R. Chowdari, *Morphologically Robust $NiFe_2O_4$ Nanofibers as High Capacity Li-Ion Battery Anode Material,* ACS Applied Materials & Interfaces **5**, 9957 (2013).

[26] G. Guzmán, J. Vazquez-Arenas, G. Ramos-Sánchez, M. Bautista-Ramírez, and I. González, *Improved performance of $LiFePO_4$ cathode for Li-ion batteries through percolation studies,* Electrochimica Acta **247**, 451 (2017).

[27] J. Newman and K. E. Thomas-Alyea, *Electrochemical systems* (John Wiley & Sons, 2012).

[28] M. Jagota and N. Tansu, *Conductivity of Nanowire Arrays under Random and Ordered Orientation Configurations,* Scientific Reports **5**, 10219 (2015).

[29] M. Park, X. Zhang, M. Chung, G. B. Less, and A. M. Sastry, *A review of conduction phenomena in Li-ion batteries,* Journal of Power Sources **195**, 7904 (2010).

[30] M. H. Al-Saleh and U. Sundararaj, *A review of vapor grown carbon nanofiber/polymer conductive composites,* Carbon **47**, 2 (2009).

[31] M. H. Kjell, E. Jacques, D. Zenkert, M. Behm, and G. Lindbergh, *PAN-based carbon fiber negative electrodes for structural lithium-ion batteries,* Journal of the Electrochemical Society **158**, A1455 (2011).

[32] M. Foygel, R. D. Morris, D. Anez, S. French, and V. L. Sobolev, *Theoretical and computational studies of carbon nanotube composites and suspensions: Electrical and thermal conductivity,* Physical Review B **71**, 104201 (2005).

[33] R. M. Mutiso, M. C. Sherrott, A. R. Rathmell, B. J. Wiley, and K. I. Winey, *Integrating Simulations and Experiments To Predict Sheet Resistance and Optical Transmittance in Nanowire Films for Transparent Conductors,* ACS Nano **7**, 7654 (2013).

[34] W. S. Bao, S. A. Meguid, Z. H. Zhu, and M. J. Meguid, *Modeling electrical conductivities of nanocomposites with aligned carbon nanotubes,* Nanotechnology **22**, 485704 (2011).

[35] J. H. Wendorff, S. Agarwal, and A. Greiner, *Electrospinning: Materials, Processing, and Applications*, 1st ed. (John Wiley & Sons, 2012).

[36] D. Li, Y. Wang, and Y. Xia, *Electrospinning Nanofibers as Uniaxially Aligned Arrays and Layer-by-Layer Stacked Films,* Advanced Materials **16**, 361 (2004).

[37] C. Kim, K. S. Yang, M. Kojima, K. Yoshida, Y. J. Kim, Y. A. Kim, and M. Endo, *Fabrication of Electrospinning-Derived Carbon Nanofiber Webs for the Anode Material of Lithium-Ion Secondary Batteries,* Advanced Functional Materials **16**, 2393 (2006).

[38] A. I. A. Abd El-Rahman and C. L. Tucker, III, *Mechanics of Random Discontinuous Long-Fiber Thermoplastics–Part I: Generation and Characterization of Initial Geometry,* Journal of Applied Mechanics **80**, 051007 (2013).

[39] Y. Pan, L. Iorga, and A. A. Pelegri, *Analysis of 3D random chopped fiber reinforced composites using FEM and random sequential adsorption,* Computation Materials Science **43**, 450 (2008).

[40] K. I. Winey, T. Kashiwagi, and M. Mu, *Improving electrical conductivity and thermal properties of polymers by the addition of carbon nanotubes as fillers,* MRS Bulletin **32**, 348 (2007).

[41] H. Chen, V. V. Ginzburg, J. Yang, Y. Yang, W. Liu, Y. Huang, L. Du, and B. Chen, *Thermal conductivity of polymer-based composites: Fundamentals and applications,* Progress in Polymer Science **59**, 41 (2016), topical Volume Hybrids.

[42] F. Dalmas, R. Dendievel, L. Chazeau, J.-Y. Cavaillé, and C. Gauthier, *Carbon nanotube-filled polymer composites. numerical simulation of electrical conductivity in three-dimensional entangled fibrous networks,* Acta Materialia **54**, 2923 (2006).

[43] H. Ma and X.-L. Gao, *A three-dimensional Monte Carlo model for electrically conductive polymer matrix composites filled with curved fibers,* Polymer **49**, 4230 (2008).

[44] W. Bauhofer and J. Z. Kovacs, *A review and analysis of electrical percolation in carbon nanotube polymer composites,* Composites Science and Technology **69**, 1486 (2009).

[45] W. Liu, N. Liu, J. Sun, P.-C. Hsu, Y. Li, H.-W. Lee, and Y. Cui, *Ionic Conductivity Enhancement of Polymer Electrolytes with Ceramic Nanowire Fillers,* Nano Letters **15**, 2740 (2015).

[46] A. Aharony and D. Stauffer, *Introduction to percolation theory* (Taylor & Francis, 2003).

[47] R. M. Mutiso and K. I. Winey, *Electrical properties of polymer nanocomposites containing rod-like nanofillers,* Progress in Polymer Science **40**, 63 (2015).

[48] N. Hu, Y. Karube, C. Yan, Z. Masuda, and H. Fukunaga, *Tunneling effect in a polymer/carbon nanotube nanocomposite strain sensor,* Acta Materialia **56**, 2929 (2008).

[49] C. Li, E. T. Thostenson, and T.-W. Chou, *Dominant role of tunneling resistance in the electrical conductivity of carbon nanotube-based composites,* Applied Physics Letters **91**, 223114 (2007).

[50] D. Eberly, *Robust computation of distance between line segments,* (2015).

[51] Y. Chen, S. Wang, F. Pan, and J. Zhang, *A numerical study on electrical percolation of polymer-matrix composites with hybrid fillers of carbon nanotubes and carbon black,* J. Nanomater. **2014** (2014), 10.1155/2014/614797.

[52] T. Schilling, M. A. Miller, and P. van der Schoot, *Percolation in suspensions of hard nanoparticles: From spheres to needles,* EPL **111**, 56004 (2015).

[53] X. Zeng, X. Xu, P. M. Shenai, E. Kovalev, C. Baudot, N. Mathews, and Y. Zhao, *Characteristics of the Electrical Percolation in Carbon Nanotubes/Polymer Nanocomposites,* Journal of Physical Chemistry C **115**, 21685 (2011).

[54] M. Soto, M. Esteva, O. Martínez-Romero, J. Baez, and A. Elías-Zúñiga, *Modeling Percolation in Polymer Nanocomposites by Stochastic Microstructuring,* Materials **8**, 6697 (2015).

[55] A. Abbaspour, J.-L. Luo, and K. Nandakumar, *Three-dimensional random resistor-network model for solid oxide fuel cell composite electrodes,* Electrochimica Acta **55**, 3944 (2010).

[56] L.-P. Simoneau, J. Villeneuve, C. M. Aguirre, R. Martel, P. Desjardins, and A. Rochefort, *Influence of statistical distributions on the electrical properties of disordered and aligned carbon nanotube networks,* Journal of Applied Physics **114**, 114312 (2013).

[57] N. Nitta, F. Wu, J. T. Lee, and G. Yushin, *Li-ion battery materials: Present and future,* Materials Today **18**, 252 (2015).

[58] C. Julien, A. Mauger, A. Vijh, and K. Zaghib, *Lithium Batteries: Science and Technology*, 1st ed. (Springer, 2016).

[59] S. D. Group, *Vapor grown carbon fiber,* .

[60] M. Dixit, H. Meyer, and T. Schilling, *Connectivity percolation in suspensions of attractive square-well spherocylinders,* Phys. Rev. E **93**, 012116 (2016).

[61] H. Meyer, P. Van der Schoot, and T. Schilling, *Percolation in suspensions of polydisperse hard rods: Quasi universality and finite-size effects,* Journal of Chemical Physics **143**, 044901 (2015).

[62] J. Škvor, I. Nezbeda, I. Brovchenko, and A. Oleinikova, *Percolation Transition in Fluids: Scaling Behavior of the Spanning Probability Functions,* Physical Review Letters **99**, 127801 (2007).

[63] M. A. Miller, *On structural correlations in the percolation of hard-core particles,* Journal of Chemical Physics **131**, 066101 (2009).

[64] S. Wang and A. Ogale, *Continuum space simulation and experimental characterization of electrical percolation behavior of particulate composites,* Composites Science and Technology **46**, 93 (1993).

[65] S. I. White, R. M. Mutiso, P. M. Vora, D. Jahnke, S. Hsu, J. M. Kikkawa, J. Li, J. E. Fischer, and K. I. Winey, *Electrical Percolation Behavior in Silver Nanowire-Polystyrene Composites: Simulation and Experiment,* Advanced Functional Materials **20**, 2709 (2010).

[66] M. J. Armstrong, C. O'Dwyer, W. J. Macklin, and J. D. Holmes, *Evaluating the performance of nanostructured materials as lithium-ion battery electrodes,* Nano Research **7**, 1 (2014).

[67] L. Long, S. Wang, M. Xiao, and Y. Meng, *Polymer electrolytes for lithium polymer batteries,* Journal of Materials Chemistry A **4**, 10038 (2016).

[68] D. Deng, *Li-ion batteries: Basics, progress, and challenges,* Energy Sci Eng. **3**, 385 (2015).

[69] Y. Gu, D. Chen, X. Jiao, and F. Liu, *$LiCoO_2$-MgO coaxial fibers: co-electrospun fabrication, characterization and electrochemical properties,* Journal of Materials Chemistry **17**, 1769 (2007).

[70] O. Toprakci, H. A. Toprakci, L. Ji, G. Xu, Z. Lin, and X. Zhang, *Carbon Nanotube-Loaded Electrospun $LiFePO_4$/Carbon Composite Nanofibers As Stable and Binder-Free Cathodes for Rechargeable Lithium-Ion Batteries,* ACS Applied Materials & Interfaces **4**, 1273 (2012).

[71] V. H. Nguyen, E. M. Jin, and H.-B. Gu, *Synthesis and electrochemical properties of $LiFePO_4$-graphite nanofiber composites as cathode materials for lithium ion batteries,* Journal of Power Sources **244**, 586 (2013).

[72] *$LiCoO_2$ Crystal Structure: Datasheet from "PAULING FILE Multinaries Edition–2012" in SpringerMaterials,* .

[73] B. Wu, Y. Ren, and N. Li, *$LiFePO_4$ Cathode Material,* in *Electric Vehicles: The Benefits and Barriers*, edited by S. Soylu (IntechOpen, 2011) Chap. 11, pp. 199–216.

[74] D. Burton, P. Lake, and A. Palmer, *Carbon Nanofiber Applications & Properties,* .

[75] D. Grazioli, O. Verners, V. Zadin, D. Brandell, and A. Simone, *Electrochemical-mechanical modeling of solid polymer electrolytes: Impact of mechanical stresses on Li-ion battery performance,* Electrochimica Acta **296**, 1122 (2019).

[76] European Commission, *Become competitive in the global battery sector to drive e-mobility and stationary storage forward,* (2016).

[77] F. Du, J. E. Fischer, and K. I. Winey, *Effect of nanotube alignment on percolation conductivity in carbon nanotube/polymer composites,* Physical Review B **72**, 121404 (2005).

3

FE^2 multiscale framework for the two-equation model of transient heat conduction in two-phase media

Abstract

In the study of transient heat conduction in heterogeneous two-phase media, the local thermal non-equilibrium condition calls for the use of a two-equation model to appropriately describe different temperatures in the two phases. We propose for the two-equation model a FE^2 multiscale framework that is capable of addressing nonlinear conduction problems. The FE^2 framework consists of volume-averaged macroscale equations, well-defined microscale problems, and the information exchange between the two scales. Compared to a traditional FE^2 method for the one-equation model, the proposed FE^2 framework introduces an additional source term at the macroscale that is upscaled from the microscale interfacial heat transfer. At variance with the tangent matrices (i.e., effective conductivity) of the heat flux, the tangent matrices of the interfacial heat transfer depend on the microscopic length scale. The proposed FE^2 framework is validated against full-scale simulations, and several numerical examples are employed to demonstrate its potential.

keywords: FE^2 method, computational homogenization, two-equation model, transient heat conduction, interfacial heat transfer

3.1 Introduction

The need for a two-equation model to describe the transient heat conduction process in a two-phase medium has long been recognized, especially when the local equilibrium condition breaks down [1–8]. Although computationally efficient, the conventional volume averaging method [1, 9–11] is often limited to linear problems due to the complexity in solving the closure problems for effective transport properties and the interfacial heat transfer coefficient. Here we propose a FE^2 multiscale framework for the two-equation model of transient heat conduction in a two-phase medium that allows for nonlinear transport problems.

Transient transport phenomena in heterogeneous materials have been traditionally addressed with the one-equation model, in which only one macroscale variable is defined on a homogenized volume originally consisting of multiple phases (for simplicity, we restrict the study to a two-phase medium). The one-equation model is suited to the local equilibrium assumption—averaged temperatures of the two phases are close or even the same—that usually holds when their transport properties are sufficiently close and the microscopic length scale is adequately small for fast heat transfer. However, when these conditions do not hold and there is net heat transfer from one phase to the other, the local equilibrium will break down. One such case is when there is a significant heat generation in any of the two phases (as discussed in Section 3.5.1, Kuwahara et al. [3], and Kaviany [12]) or, analogously, a kinetic reaction source in the biofilm phase in porous media in environmental engineering applications [5, 6]. Another scenario leading to equilibrium breakdown is when there is a great disparity of conductivity between the two phases (as discussed in Section 3.5.1 and Mahmoudi and Karimi [13]). A more general description is required for the separate treatment of average values in the two phases and the explicit description of the interfacial heat transfer [1, 3, 7, 8, 14, 15]. This general strategy is termed the two-equation model, named after the work by Quintard et al. [1, 2].

The two-equation model is also required when the two phases are characterized by different physics. By way of example, in lithium-ion battery cells [16, 17], electrodes consist of active materials, electrolyte, and conductive materials. During the (dis)charging process, lithium ions diffuse and migrate in the electrolyte, while lithium diffuses in the active material. The quantities of concern in the two phases, the concentration of lithium ions in the electrolyte and concentration of lithium in the active material, differ in the physical meaning, and their values are generally not equal [16, 17]. They are connected through the consistence of mass flux between the two phases ensured by chemical reactions occurring on the interface, described for example by the Butler-Volmer equation [16].

Traditionally, the two-equation model is solved analytically. Homogenized diffusion equations are first derived at the macroscale via the volume averaging method [11, 18]. The so-called closure problems are then defined on the averaging volume at the microscale and

solved for the effective transport coefficients and interfacial heat transfer coefficient needed in the homogenized equations [1, 9, 19]. Despite of computational efficiency, this method is restricted to linear conduction problems and impaired by accuracy concerns due to many simplification assumptions.

Instead of analytically solving homogenized equations, an accurate and straightforward method is to perform a single-scale numerical simulation (also called direct numerical simulation in some fields). A single-scale simulation resolves the microscale geometry and therefore is quite accurate; the price for accuracy is the computational cost that could be as high as rendering the simulation infeasible especially when the problem domain spans spatial scales of several orders of magnitude. To avoid the significant simulation cost attached to a fully resolved domain and retain the same level of accuracy, a multiscale computational technique, called the FE^2 method, has been developed and successfully employed in applications ranging from mechanical equilibrium problems [20–26] to transport problems [27–29].

Existing works [27–31] using the FE^2 method are however applied to the one-equation model as they consider one homogenized variable defined on the representative volume element (RVE) and use the effective material properties (stiffness, conductivity) of the whole RVE that may consist of multiple phases. These frameworks cannot offer separate information for each phase (refer to Section 3.3.5), as needed in applications requiring a two-equation model. To this end, this study proposes a FE^2 two-scale framework (Section 3.3) as well as its implementation (Section 3.4) for the two-equation model setting.

3.2 Single-scale description

The composite under consideration consists of two phases—the matrix (β phase) and the inclusion (σ phase)—as shown in Fig. 3.1a. The two phases possess different transport properties. Physical quantities associated with β phase and σ phase are distinguished by the subscripts β and σ, respectively. Transient heat conduction in the two-phase medium is governed by

$$c_\beta \frac{\partial u_\beta}{\partial t} + \boldsymbol{\nabla} \cdot \mathbf{h}_\beta = r_\beta \quad \text{in} \quad V_\beta \times [0, t_{\text{end}}] \quad \text{and} \tag{3.1a}$$

$$c_\sigma \frac{\partial u_\sigma}{\partial t} + \boldsymbol{\nabla} \cdot \mathbf{h}_\sigma = r_\sigma \quad \text{in} \quad V_\sigma \times [0, t_{\text{end}}], \tag{3.1b}$$

where c, u, $\mathbf{h}$, and r represent, respectively, volumetric heat capacity, temperature, heat flux, and the given volumetric heat source. The heat flux is described by Fourier's law and

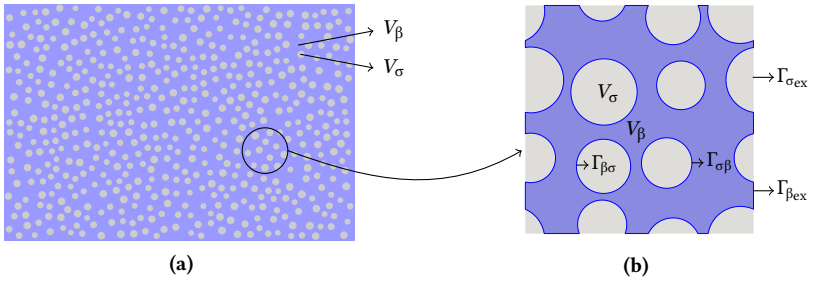

Fig. 3.1. (a) A two-phase medium consisting of the blue matrix (β phase occupying V_β) and gray inclusions (σ phase occupying V_σ) possessing different transport properties. (b) Microscopic representative volume element (RVE). The RVE boundary Γ_{ex} is divided into two parts, each associated with a phase, such that $\Gamma_{ex} = \Gamma_{\beta ex} \cup \Gamma_{\sigma ex}$ with $\Gamma_{\beta ex} \cap \Gamma_{\sigma ex} = \varnothing$. The interface between the two phases is represented by two coinciding boundaries $\Gamma_{\beta\sigma}$ and $\Gamma_{\sigma\beta}$ belonging to the β and σ phases, respectively.

expressed as

$$\mathbf{h}_\beta = -k_\beta(u_\beta)\boldsymbol{\nabla} u_\beta, \tag{3.2a}$$

$$\mathbf{h}_\sigma = -k_\sigma(u_\sigma)\boldsymbol{\nabla} u_\sigma, \tag{3.2b}$$

where the thermal conductivity for each phase is generally temperature dependent.

Across the interface between the two phases, we consider the temperature continuity condition (i.e., $u_\beta = u_\sigma$). These two governing equations can be readily solved by a standard finite element program. Specifically, each phase will be discretized and a common node will be used at the interface. This solution strategy is referred to as the single-scale approach, and it will be used as a reference for the proposed multiscale approach.

3.3 Multiscale framework

This section outlines the FE^2 two-scale computational framework where the governing equations at the two scales and the corresponding information-passing procedures are described. In the remainder of the paper, we use lower case letters to represent microscale quantities while upper case letters refer to macroscale quantities. For example, the microscale temperature is denoted by u, while U represents the macroscale temperature.

3.3.1 Macroscale problem

The macroscale governing equations are derived by volume-averaging the single-scale formulation presented in the previous section over a representative volume element. With reference to the RVE (Fig. 3.1b), applying the volume average operator (3.76) to Eq. (3.1a)

yields

$$c_\beta \frac{\partial \langle u_\beta \rangle}{\partial t} + \langle \nabla \cdot \mathbf{h}_\beta \rangle = \langle r_\beta \rangle \quad \text{in} \quad V_\beta \times [0, t_{\text{end}}]. \tag{3.3}$$

The volume-averaged temperature $\langle u_\beta \rangle$ is expressed in terms of the intrinsic average $\bar{u}_\beta$ which is defined as the macroscale temperature U_β:

$$\langle u_\beta \rangle = \epsilon_\beta \bar{u}_\beta = \epsilon_\beta U_\beta, \tag{3.4}$$

where ϵ_β is the volume fraction of the β phase. The volume-averaged flux divergence is split into two surface integrals (Fig. 3.1b):

$$\langle \nabla \cdot \mathbf{h}_\beta \rangle = \frac{1}{V} \int_{V_\beta} \nabla \cdot \mathbf{h}_\beta \, \mathrm{d}V = \frac{1}{V} \int_{\Gamma_{\beta\text{ex}}} \mathbf{h}_\beta \cdot \mathbf{n}_{\beta\text{ex}} \, \mathrm{d}A + \frac{1}{V} \int_{\Gamma_{\beta\sigma}} \mathbf{h}_\beta \cdot \mathbf{n}_{\beta\sigma} \, \mathrm{d}A, \tag{3.5}$$

where $\Gamma_{\beta\text{ex}}$ and $\Gamma_{\beta\sigma}$ represent the RVE boundary contributed by the β phase and the interface with the σ phase, respectively, $\mathbf{n}_{\beta\text{ex}}$ is the outward-pointing unit vector normal to $\Gamma_{\beta\text{ex}}$, and $\mathbf{n}_{\beta\sigma}$ is the unit vector normal to $\Gamma_{\beta\sigma}$ pointing from the β phase to the σ phase. The volume-averaged heat source in the right-hand side of Eq. (3.3) is defined as the macroscale heat source

$$R_\beta = \langle r_\beta \rangle, \tag{3.6}$$

where the volumetric heat source r_β is a given quantity.

Substituting Eqs. (3.4) to (3.6) into Eq. (3.3) yields

$$c_\beta \epsilon_\beta \frac{\partial U_\beta}{\partial t} + \frac{1}{V} \int_{\Gamma_{\beta\text{ex}}} \mathbf{h}_\beta \cdot \mathbf{n}_{\beta\text{ex}} \, \mathrm{d}A = R_\beta - \frac{1}{V} \int_{\Gamma_{\beta\sigma}} \mathbf{h}_\beta \cdot \mathbf{n}_{\beta\sigma} \, \mathrm{d}A. \tag{3.7}$$

The heat outflow through the RVE boundary $\Gamma_{\beta\text{ex}}$ can be regarded as the divergence of the heat flux at a macroscale point:

$$\frac{1}{V} \int_{\Gamma_{\beta\text{ex}}} \mathbf{h}_\beta \cdot \mathbf{n}_{\beta\text{ex}} \, \mathrm{d}A = \nabla \cdot \mathbf{H}_\beta, \tag{3.8}$$

and the heat transfer from the β phase to the σ phase can be defined as the heat sink, or negative heat source, at a macroscale point:

$$\frac{1}{V} \int_{\Gamma_{\beta\sigma}} \mathbf{h}_\beta \cdot \mathbf{n}_{\beta\sigma} \, \mathrm{d}A = -Q_\beta. \tag{3.9}$$

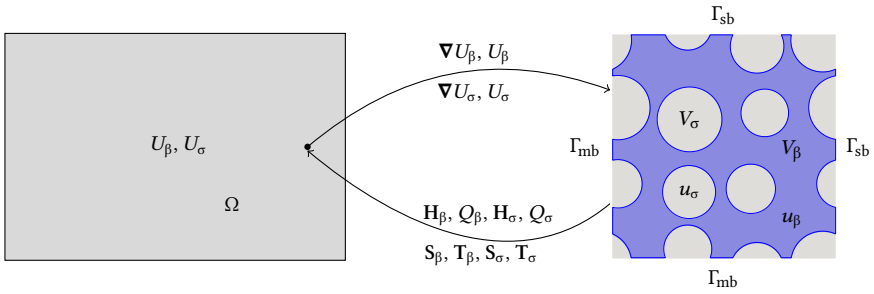

Fig. 3.2. Homogenized domain at the macroscale, RVE at the microscale, and information exchange between macro- and micro-scales. Macroscale temperatures U_β and U_σ, and their gradients ∇U_β and ∇U_σ are downscaled as boundary conditions for the microscale RVE problem. The homogenized fluxes $\mathbf{H}_\beta$ and $\mathbf{H}_\sigma$ (Eq. (3.30)), volumetric interfacial heat transfer Q_β (Eq. (3.9)) and Q_σ (Eq. (3.13)), and their dependencies $\mathbf{S}_\beta$, $\mathbf{S}_\sigma$, $\mathbf{T}_\beta$, and $\mathbf{T}_\sigma$ (Eq. (3.31)) on the macroscale quantities $\mathbf{X}$ (Eq. (3.14)) are then transferred back to the macroscale problem. Panel (b) shows also the boundaries used for the enforcement of periodic boundary conditions in the FE analysis of the RVE: left and bottom edges are denoted as the master boundaries Γ_{mb}, while the right and upper edges are considered as the slave boundaries Γ_{sb}.

Macroscale equation (3.7) can thus be expressed as

$$c_\beta \epsilon_\beta \frac{\partial U_\beta}{\partial t} + \nabla \cdot \mathbf{H}_\beta = R_\beta + Q_\beta \quad \text{in} \quad \Omega \times [0, t_{\text{end}}], \tag{3.10a}$$

where Ω denotes the homogenized domain shared by both phases at the macroscale as shown in Fig. 3.2a. Likewise, we can derive the macroscale equation for the σ phase as

$$c_\sigma \epsilon_\sigma \frac{\partial U_\sigma}{\partial t} + \nabla \cdot \mathbf{H}_\sigma = R_\sigma + Q_\sigma \quad \text{in} \quad \Omega \times [0, t_{\text{end}}], \tag{3.10b}$$

where the macroscale temperature

$$U_\sigma = \bar{u}_\sigma = \frac{\langle u_\sigma \rangle}{\epsilon_\sigma} \tag{3.11}$$

represents the intrinsic average of the temperature of the σ phase, the macroscale heat source

$$R_\sigma = \langle r_\sigma \rangle \tag{3.12}$$

is the volume average of the given heat source r_σ, and the additional macroscale heat source

$$Q_\sigma = -\frac{1}{V} \int_{\Gamma_{\sigma\beta}} \mathbf{h}_\sigma \cdot \mathbf{n}_{\sigma\beta} \, \mathrm{d}A \tag{3.13}$$

is caused by the interfacial heat transfer.

The macroscale heat fluxes ($\mathbf{H}_\beta$ and $\mathbf{H}_\sigma$) and the macroscale heat sources (Q_β and Q_σ) due to interfacial heat transfer in the macroscale governing equation (3.10) are obtained through the microscale computation. As schematically shown in Fig. 3.2, the macroscale solution U_β and U_σ and their gradients at an integration point are downscaled to define the microscale problem; the macroscale heat fluxes and sources as well as their tangents are then computed from the microscale solution and upscaled. Moreover, in the microscale simulation the temperature continuity condition ($u_\beta = u_\sigma$) is enforced across the interface, and thus the flux continuity naturally holds: $Q_\beta + Q_\sigma = 0$.

3.3.2 Downscaling

The boundary conditions enforced at the microscale level are obtained by downscaling macroscale quantities at each integration point of the macroscale mesh: temperature U_β and U_σ, and their gradients $\boldsymbol{\nabla} U_\beta$ and $\boldsymbol{\nabla} U_\sigma$, respectively. For conciseness, these quantities are stored in a column vector as

$$\mathbf{X} = \begin{bmatrix} (\boldsymbol{\nabla} U_\beta)^{\mathrm{T}} & U_\beta & (\boldsymbol{\nabla} U_\sigma)^{\mathrm{T}} & U_\sigma \end{bmatrix}^{\mathrm{T}}. \tag{3.14}$$

3.3.3 Microscale problem

The microscale problem is defined on an RVE (Fig. 3.2b) associated with a macroscale integration point. At variance with the single-scale description (3.1), the governing equations at the microscale neglect the time evolution terms and consider the steady-state thermal equilibrium [27, 30], in view of the relatively small RVE size. The governing equations are thus expressed as

$$\boldsymbol{\nabla} \cdot \mathbf{h}_\beta = b_\beta \quad \text{in } V_\beta \text{ and} \tag{3.15a}$$

$$\boldsymbol{\nabla} \cdot \mathbf{h}_\sigma = b_\sigma \quad \text{in } V_\sigma, \tag{3.15b}$$

where the constitutive relations for heat fluxes $\mathbf{h}_\beta$ and $\mathbf{h}_\sigma$ are the same as in Eq. (3.2). The two source terms b_β and b_σ are different from the given source terms r_β and r_σ in the single-scale equation (3.1). The prescribed heat sources (r_β and r_σ) are included in the macroscale governing equation (3.10) in an average sense—R_β in Eq. (3.6) and R_σ in Eq. (3.12)—and will be indirectly reflected at the microscale through the enforcement of consistent temperatures across the two scales as expressed by Eq. (3.23). The two terms b_β and b_σ actually reflect unknown heat sources caused by enforcing the constraint (3.23), acting as constraint forces and regardless of the given heat sources r_β and r_σ.

Next, the microscale boundary conditions are derived from the macroscale quantities $\mathbf{X}$ (Eq. (3.14)). By convention in the FE^2 analysis, the microscale temperature profiles $u_\beta(\mathbf{x})$

and $u_\sigma(\mathbf{x})$, with $\mathbf{x}$ as the position vector, can be decomposed into a spatially linear field (first two terms) and a fluctuation filed (the last term):

$$u_\beta = U_\beta + \boldsymbol{\nabla} U_\beta \cdot (\mathbf{x} - \mathbf{x}_{\mathrm{ra}}) + \tilde{u}_\beta, \tag{3.16a}$$

$$u_\sigma = U_\sigma + \boldsymbol{\nabla} U_\sigma \cdot (\mathbf{x} - \mathbf{x}_{\mathrm{rb}}) + \tilde{u}_\sigma, \tag{3.16b}$$

where $\mathbf{x}_{\mathrm{ra}}$ and $\mathbf{x}_{\mathrm{rb}}$ are reference points.

In the FE^2 analyses of mechanical problems [23, 32], it is a common practice to assume that the macroscale deformation gradient at a point is equal to the volume average of the microscale counterpart over the whole RVE defined on that point. This assumption, connecting the macro- and micro-scales, is known as the averaging theorem [33]. Likewise, in the FE^2 analysis of heat conduction [27], the macroscale temperature gradient is usually assumed to be equal to the volume average of the microscale temperature gradient. The transfer of temperature gradient for the one-equation model [27] is as straightforward as the strain transfer. However, it requires special consideration in the two-equation model since there are two macroscale temperature gradients—$\boldsymbol{\nabla} U_\beta$ and $\boldsymbol{\nabla} U_\sigma$. Here we propose the following relations as an equivalent for the assumption described above:

$$\frac{1}{V} \int_{\Gamma_{\mathrm{ex}}} u_\beta \mathbf{n}_{\mathrm{ex}} \, \mathrm{d}A = \boldsymbol{\nabla} U_\beta, \tag{3.17a}$$

$$\frac{1}{V} \int_{\Gamma_{\mathrm{ex}}} u_\sigma \mathbf{n}_{\mathrm{ex}} \, \mathrm{d}A = \boldsymbol{\nabla} U_\sigma, \tag{3.17b}$$

where $\mathbf{n}_{\mathrm{ex}}$ is the outward-pointing normal vector to the RVE boundary Γ_{ex} and the surface integral is over the whole RVE boundary $\Gamma_{\mathrm{ex}} = \Gamma_{\beta\mathrm{ex}} \cup \Gamma_{\sigma\mathrm{ex}}$ (Fig. 3.1b). The surface integral is equivalent to the previously mentioned volume integral via the divergence theorem but is preferred especially when holes/voids exist in the RVE [24, 34, 35]. Here, the σ phase regions act as holes for the β phase, and vice versa.

Substituting Eq. (3.16a) into Eq. (3.17a) results in

$$\frac{1}{V} \int_{\Gamma_{\mathrm{ex}}} u_\beta \mathbf{n}_{\mathrm{ex}} \, \mathrm{d}A = \boldsymbol{\nabla} U_\beta + \frac{1}{V} \int_{\Gamma_{\mathrm{ex}}} \tilde{u}_\beta \mathbf{n}_{\mathrm{ex}} \, \mathrm{d}A \,. \tag{3.18}$$

In the derivation, $\mathbf{n}_{\mathrm{ex}}$ should be evaluated at every point on the whole RVE boundary including the portion for the σ phase ($\Gamma_{\sigma\mathrm{ex}}$) although u_β is only defined in the β phase. This procedure is necessary because the σ phase is the complementary voids of the β phase in the RVE. To the void phase σ we can attach fictitious u_β values and null conductivity, analogous to null stiffness in mechanical problems [24, 35]. Comparison of Eq. (3.18) with Eq. (3.17a)

yields

$$\int_{\Gamma_{ex}} \tilde{u}_\beta \mathbf{n}_{ex} \, d\Gamma = 0, \tag{3.19a}$$

Similarly, for the σ phase we arrive at

$$\int_{\Gamma_{ex}} \tilde{u}_\sigma \mathbf{n}_{ex} \, d\Gamma = 0. \tag{3.19b}$$

Constraints (3.19) are enforced by means of periodic boundary conditions [23, 24, 36]. For the two-phase composition of the RVE boundary, we assume the nomenclature reported in Fig. 3.2b to identify master and slave portions of the boundary. The periodic boundary conditions are therefore stated as

$$\tilde{u}_\beta(\mathbf{x}_{mb}) = \tilde{u}_\beta(\mathbf{x}_{sb}), \tag{3.20a}$$
$$\tilde{u}_\sigma(\mathbf{x}_{mb}) = \tilde{u}_\sigma(\mathbf{x}_{sb}), \tag{3.20b}$$

where $\mathbf{x}_{mb}$ represents an arbitrary point on the master boundary Γ_{mb} and its counterpart on the slave boundary Γ_{sb} is denoted as $\mathbf{x}_{sb}$. Substituting Eq. (3.20) into Eq. (3.16) leads to

$$u_\beta(\mathbf{x}_{mb}) - u_\beta(\mathbf{x}_{sb}) - \boldsymbol{\nabla} U_\beta \cdot (\mathbf{x}_{mb} - \mathbf{x}_{sb}) = 0, \tag{3.21a}$$
$$u_\sigma(\mathbf{x}_{mb}) - u_\sigma(\mathbf{x}_{sb}) - \boldsymbol{\nabla} U_\sigma \cdot (\mathbf{x}_{mb} - \mathbf{x}_{sb}) = 0. \tag{3.21b}$$

The temperature continuity condition at the two-phase interface is also enforced and expressed as

$$\left[u_\beta\right]_{\Gamma_{\beta\sigma}} - \left[u_\sigma\right]_{\Gamma_{\sigma\beta}} = 0. \tag{3.22}$$

Moreover, from the definition of the macroscale temperatures in Eqs. (3.4) and (3.11), we have two additional constraints:

$$\bar{u}_\beta - U_\beta = 0, \tag{3.23a}$$
$$\bar{u}_\sigma - U_\sigma = 0. \tag{3.23b}$$

These two extra requirements are necessary for the solution of the microscale problem as they 1) allow to objectively determine unique microscale solutions for each phase (the reference points in Eq. (3.16) are not determined), and 2) enforce the consistency of the stored heat in each phase between the macro- and micro-scales. This last aspect is fundamental: enforcing the heat consistency constraint indirectly applies the heat source to the microscale governing

equation (3.15), which is only explicitly implemented in the macroscale equation (3.10).

3.3.4 Upscaling

To close the information exchange loop, the homogenized fluxes $\mathbf{H}_\beta$ and $\mathbf{H}_\sigma$ and their tangent matrices are calculated from the microscale solution and upscaled to the macroscale computation (Fig. 3.2). The homogenized fluxes are calculated as the volume averages of the corresponding microscale heat fluxes:

$$\mathbf{H}_\beta = \frac{1}{V}\int_{V_\beta} \mathbf{h}_\beta \,\mathrm{d}V\,, \tag{3.24a}$$

$$\mathbf{H}_\sigma = \frac{1}{V}\int_{V_\beta} \mathbf{h}_\sigma \,\mathrm{d}V\,. \tag{3.24b}$$

For the sake of numerical implementation, the volume integrals are often transformed into surface integrals. The right-hand side of Eq. (3.24a) is reformulated as

$$\begin{aligned}\frac{1}{V}\int_{V_\beta} \mathbf{h}_\beta \,\mathrm{d}V &= \frac{1}{V}\int_{V_\beta} \left[\boldsymbol{\nabla}\cdot\left(\mathbf{x}\,\mathbf{h}_\beta\right) - \mathbf{x}\boldsymbol{\nabla}\cdot\mathbf{h}_\beta\right]\mathrm{d}V \\ &= \frac{1}{V}\int_{\Gamma_{\beta\mathrm{ex}}} \mathbf{x}\,\mathbf{h}_\beta\cdot\mathbf{n}_{\beta\mathrm{ex}}\,\mathrm{d}A + \left(\frac{1}{V}\int_{\Gamma_{\beta\sigma}} \mathbf{x}\,\mathbf{h}_\beta\cdot\mathbf{n}_{\beta\sigma}\,\mathrm{d}A - \frac{1}{V}\int_{V_\beta} \mathbf{x}\,b_\beta\,\mathrm{d}V\right),\end{aligned} \tag{3.25}$$

where the divergence theorem and the microscale governing equation (3.15a) are used in the derivation. The last two terms in the bracket of Eq. (3.25) approximate to each other and can be neglected. The demonstration is as follows. Applying volume integral to Eq. (3.15a) yields

$$\frac{1}{V}\int_{V_\beta} \left(\boldsymbol{\nabla}\cdot\mathbf{h}_\beta - b_\beta\right)\mathrm{d}V = 0 = \frac{1}{V}\int_{\Gamma_{\beta\mathrm{ex}}} \mathbf{h}_\beta\cdot\mathbf{n}_{\beta\mathrm{ex}}\,\mathrm{d}A + \frac{1}{V}\int_{\Gamma_{\beta\sigma}} \mathbf{h}_\beta\cdot\mathbf{n}_{\beta\sigma}\,\mathrm{d}A - \frac{1}{V}\int_{V_\beta} b_\beta\,\mathrm{d}V\,. \tag{3.26}$$

The first term in the right-hand side of Eq. (3.26) actually vanishes. According to the periodic boundary condition (3.21a), we evaluate $\mathbf{h}_\beta\cdot\mathbf{n}_{\beta\mathrm{ex}}$ at the master boundary to be the opposite of that at the corresponding slave boundary. This is called the anti-periodic normal flux boundary condition [27] and its enforcement through Lagrange multipliers is detailed in Section 3.4.2. Therefore, the last two terms in Eq. (3.26) should cancel out each other. Multiplying them by a position vector gives

$$\frac{1}{V}\int_{\Gamma_{\beta\sigma}} \mathbf{x}_\mathrm{c}\,\mathbf{h}_\beta\cdot\mathbf{n}_{\beta\sigma}\,\mathrm{d}A = \frac{1}{V}\int_{V_\beta} \mathbf{x}_\mathrm{c}\,b_\beta\,\mathrm{d}V\,, \tag{3.27}$$

where $\mathbf{x}_\mathrm{c}$ denotes the geometry center of the RVE. The unknown heat source b_β due to the constraint (3.23a) is uniform in the RVE domain because a single Lagrange multiplier is used

to impose the constraint (3.23a). Therefore, the right-hand term in Eq. (3.27) is equal to the last term in Eq. (3.25)

$$\frac{1}{V}\int_{V_\beta} \mathbf{x}_c\, b_\beta \,\mathrm{d}V = \frac{1}{V}\int_{V_\beta} \mathbf{x}\, b_\beta \,\mathrm{d}V\,. \tag{3.28}$$

In view of Eqs. (3.27) and (3.28), the subtraction in the bracket of Eq. (3.25) is calculated as

$$\frac{1}{V}\int_{\Gamma_{\beta\sigma}} \mathbf{x}\,\mathbf{h}_\beta\cdot\mathbf{n}_{\beta\sigma}\,\mathrm{d}A - \frac{1}{V}\int_{V_\beta} \mathbf{x}\, b_\beta \,\mathrm{d}V = \frac{1}{V}\int_{\Gamma_{\beta\sigma}} (\mathbf{x}-\mathbf{x}_c)\,\mathbf{h}_\beta\cdot\mathbf{n}_{\beta\sigma}\,\mathrm{d}A\,. \tag{3.29}$$

Due to the relatively small RVE size, the right-hand term in Eq. (3.29) can be assumed to be null and thus ignored, which has also been numerically validated in our simulations. The above derivations also apply to the σ phase, and hence the macroscale heat fluxes in Eq. (3.24) can be expressed in terms of surface integrals as

$$\mathbf{H}_\beta = \frac{1}{V}\int_{\Gamma_{\beta\mathrm{ex}}} \mathbf{x}\,\mathbf{h}_\beta\cdot\mathbf{n}_{\beta\mathrm{ex}}\,\mathrm{d}A\,, \tag{3.30a}$$

$$\mathbf{H}_\sigma = \frac{1}{V}\int_{\Gamma_{\sigma\mathrm{ex}}} \mathbf{x}\,\mathbf{h}_\sigma\cdot\mathbf{n}_{\sigma\mathrm{ex}}\,\mathrm{d}A\,. \tag{3.30b}$$

The volumetric interfacial heat transfer Q_β and Q_σ are calculated according to Eqs. (3.9) and (3.13). Moreover, the dependencies

$$\mathbf{S}_\beta = \frac{\delta\mathbf{H}_\beta}{\delta\mathbf{X}}, \quad \mathbf{T}_\beta = \frac{\delta Q_\beta}{\delta\mathbf{X}}, \tag{3.31a}$$

$$\mathbf{S}_\sigma = \frac{\delta\mathbf{H}_\sigma}{\delta\mathbf{X}}, \quad \mathbf{T}_\sigma = \frac{\delta Q_\sigma}{\delta\mathbf{X}} \tag{3.31b}$$

of these quantities with respect to the macroscale quantities $\mathbf{X}$ (Eq. (3.14)) are also passed back to the macroscale.

3.3.5 Comparison with one-equation model

The obvious similarity between the structures of the one- and two-equation models calls for a simple comparison. Adding Eqs. (3.10a) and (3.10b) together results in

$$c\frac{\partial U}{\partial t} + \boldsymbol{\nabla}\cdot\mathbf{H} = R_\beta + R_\sigma, \tag{3.32}$$

where the volumetric heat capacity

$$c = c_\beta\epsilon_\beta + c_\sigma\epsilon_\sigma \tag{3.33}$$

represents the volume-averaged heat capacity, the homogenized temperature is the total thermal energy over the volume-averaged heat capacity

$$U = \frac{c_\beta \epsilon_\beta U_\beta + c_\sigma \epsilon_\sigma U_\sigma}{c}, \tag{3.34}$$

and the macroscale heat flux $\mathbf{H}$ is equal to

$$\mathbf{H} = \mathbf{H}_\beta + \mathbf{H}_\sigma. \tag{3.35}$$

Comparing the preceding equations with those in the one-equation model in Özdemir et al. [27], it can be seen that the volume-averaged heat capacity c and the macroscale heat flux $\mathbf{H}$ (substituting Eq. (3.24) into Eq. (3.35)) have the same meanings as defined in Özdemir et al. [27]. The macroscale temperature in Özdemir et al. [27] is not defined with an explicit meaning, but from this comparison we know it has exactly the same meaning as U in Eq. (3.34), i.e., the total thermal energy over the volume-averaged heat capacity, and not the volume-averaged temperature

$$U = \epsilon_\beta U_\beta + \epsilon_\sigma U_\sigma. \tag{3.36}$$

However, if the heat capacities of the two phases are the same ($c_\beta = c_\sigma$), the macroscale temperature (Eq. (3.34)) of the one-equation model reduces to the volume-averaged temperature.

Because of the equivalence, the one-equation model can be considered as a special case of the two-equation model.

3.4 Implementation of the multiscale framework

This section provides the numerical implementation of the FE^2 framework: the finite element implementation of the macroscale and microscale problems and the numerical procedures for the calculation of the upscaled quantities. All vectors are column vectors by default.

3.4.1 Finite element method for macroscale problem

According to standard finite element procedures [37], the weak form of the macroscale governing equation (3.10) is expressed as

$$\int_\Omega c_\beta \epsilon_\beta \frac{\partial U_\beta}{\partial t}\,\delta U_\beta \,\mathrm{d}V - \int_\Omega \boldsymbol{\nabla}\,\delta U_\beta \cdot \mathbf{H}_\beta \,\mathrm{d}V - \int_\Omega \left(Q_\beta + R_\beta\right)\delta U_\beta \,\mathrm{d}V + \int_{\partial\Omega} \overline{H}_\beta\,\delta U_\beta \,\mathrm{d}\Gamma = 0, \tag{3.37a}$$

$$\int_\Omega c_\sigma \epsilon_\sigma \frac{\partial U_\sigma}{\partial t}\,\delta U_\sigma \,\mathrm{d}V - \int_\Omega \boldsymbol{\nabla}\,\delta U_\sigma \cdot \mathbf{H}_\sigma \,\mathrm{d}V - \int_\Omega \left(Q_\sigma + R_\sigma\right)\delta U_\sigma \,\mathrm{d}V + \int_{\partial\Omega} \overline{H}_\sigma\,\delta U_\sigma \,\mathrm{d}\Gamma = 0, \tag{3.37b}$$

where δU_β and δU_σ are variations of field variables, $\overline{H}_\beta$ and $\overline{H}_\sigma$ are prescribed heat fluxes at the macroscale boundaries $\partial\Omega$, and R_β and R_σ are calculated from given microscale heat sources via Eqs. (3.6) and (3.12).

The macroscale heat fluxes $\mathbf{H}_\beta$ and $\mathbf{H}_\sigma$ and the heat sources Q_β and Q_σ due to interfacial heat transfer at an integration point are calculated from the microscale problem solution and generally depend on temperatures U_β and U_σ. Because of the coupling of the two governing equations, they are solved simultaneously; therefore, each node in the spatial discretization has two degrees of freedom, one for U_β and the other for U_σ.

A standard finite element approximation is used to discretize the field variables. The temperature fields $U_\beta(\mathbf{x})$ and $U_\sigma(\mathbf{x})$ at an arbitrary point $\mathbf{x}$ are approximated by interpolating between nodal values in such a way

$$U_\beta(\mathbf{x}) = \mathbf{N}(\mathbf{x})\,\mathbf{U}_\beta \quad \text{and} \quad U_\sigma(\mathbf{x}) = \mathbf{N}(\mathbf{x})\,\mathbf{U}_\sigma, \tag{3.38}$$

where

$$\mathbf{N} = \begin{bmatrix} N_1(\mathbf{x}) & N_2(\mathbf{x}) & \cdots & N_{n_\mathrm{m}}(\mathbf{x}) \end{bmatrix} \tag{3.39}$$

collects the shape functions associated with the n_m nodes of the discretized macroscale domain, and vectors $\mathbf{U}_\beta$ and $\mathbf{U}_\sigma$ contain nodal unknowns. Similarly, the variations of the field variables are expressed as

$$\delta U_\beta\,(\mathbf{x}) = \mathbf{N}(\mathbf{x})\;\delta\mathbf{U}_\beta \quad \text{and} \quad \delta U_\sigma\,(\mathbf{x}) = \mathbf{N}(\mathbf{x})\;\delta\mathbf{U}_\sigma\,. \tag{3.40}$$

Substituting Eqs. (3.38) and (3.40) into the weak form (3.37), the weak statement in matrix

notation is rewritten as

$$\mathbf{F}_\beta = \int_\Omega c_\beta \epsilon_\beta \mathbf{N}^\mathrm{T}\mathbf{N}\frac{\Delta \mathbf{U}_\beta}{\Delta t}\,\mathrm{d}V - \int_\Omega \mathbf{B}^\mathrm{T}\mathbf{H}_\beta\,\mathrm{d}V - \int_\Omega \left(Q_\beta + R_\beta\right)\mathbf{N}^\mathrm{T}\,\mathrm{d}V + \int_{\partial\Omega} \overline{H}_\beta \mathbf{N}^\mathrm{T}\,\mathrm{d}\Gamma = \mathbf{0}, \quad (3.41a)$$

$$\mathbf{F}_\sigma = \int_\Omega c_\sigma \epsilon_\sigma \mathbf{N}^\mathrm{T}\mathbf{N}\frac{\Delta \mathbf{U}_\sigma}{\Delta t}\,\mathrm{d}V - \int_\Omega \mathbf{B}^\mathrm{T}\mathbf{H}_\sigma\,\mathrm{d}V - \int_\Omega \left(Q_\sigma + R_\sigma\right)\mathbf{N}^\mathrm{T}\,\mathrm{d}V + \int_{\partial\Omega} \overline{H}_\sigma \mathbf{N}^\mathrm{T}\,\mathrm{d}\Gamma = \mathbf{0}, \quad (3.41b)$$

where the matrix

$$\mathbf{B} = \boldsymbol{\nabla}\mathbf{N} = \begin{bmatrix} \dfrac{\partial N_1}{\partial x_1} & \dfrac{\partial N_2}{\partial x_1} & \cdots & \dfrac{\partial N_{n_\mathrm{m}}}{\partial x_1} \\ \dfrac{\partial N_1}{\partial x_2} & \dfrac{\partial N_2}{\partial x_2} & \cdots & \dfrac{\partial N_{n_\mathrm{m}}}{\partial x_2} \end{bmatrix} \quad (3.42)$$

contains derivatives of the shape functions, and the backward Euler method is used for the discretization of the time derivative terms in Eq. (3.37). In Eq. (3.41), the temperature increments $\Delta\mathbf{U}_\beta$ and $\Delta\mathbf{U}_\sigma$ are evaluated between the current time step and the last converged time step, and Δt denotes the time step size; the macroscale fluxes $\mathbf{H}_\beta$ and $\mathbf{H}_\sigma$ and the heat sources Q_β and Q_σ are approximated by the values of the current time step.

We now collect the two sets of discrete equations in Eq. (3.41) and the two field variables in the following arrays

$$\mathbf{F} = \begin{bmatrix} \mathbf{F}_\beta \\ \mathbf{F}_\sigma \end{bmatrix} \quad \text{and} \quad \mathbf{U} = \begin{bmatrix} \mathbf{U}_\beta \\ \mathbf{U}_\sigma \end{bmatrix}, \quad (3.43)$$

respectively. The Newton-Raphson iteration procedure is then employed to solve the system of discrete equations

$$\mathbf{F}\left(\mathbf{U}_n\right) = \mathbf{0}$$

at the current time step n ($t = t_n$). The system of linearized equations at iteration step k is expressed as

$$\mathbf{K}\left(\mathbf{U}_n^{k+1} - \mathbf{U}_n^k\right) + \mathbf{F}\left(\mathbf{U}_n^k\right) = \mathbf{0}, \quad (3.44)$$

where the global tangent matrix $\mathbf{K}$ is evaluated at iteration step k as

$$\mathbf{K} = \left[\frac{\partial \mathbf{F}}{\partial \mathbf{U}_n}\right]_k = \begin{bmatrix} \mathbf{K}_{\beta\beta} & \mathbf{K}_{\beta\sigma} \\ \mathbf{K}_{\sigma\beta} & \mathbf{K}_{\sigma\sigma} \end{bmatrix}_k. \quad (3.45)$$

To compute the residual vector $\mathbf{F}$ in Eq. (3.41), the macroscale fluxes $\mathbf{H}_\beta$ and $\mathbf{H}_\sigma$ at each integration point are directly upscaled from the microscale problem solution and their

formulations are presented in Section 3.4.3 via Eq. (3.60); likewise, the macroscale heat sources Q_β and Q_σ are obtained through Eq. (3.62). The tangent matrix $\mathbf{K}$ is calculated from the upscaled tangent matrices $\mathbf{S}_\beta$, $\mathbf{S}_\sigma$, $\mathbf{T}_\beta$, and $\mathbf{T}_\sigma$, as demonstrated below. The four components of $\mathbf{K}$ in Eq. (3.45) can be expressed as

$$\mathbf{K}_{\beta\beta} = \frac{\partial \mathbf{F}_\beta}{\partial \mathbf{U}_\beta} = \int_\Omega \frac{c_\beta \epsilon_\beta}{\Delta t} \mathbf{N}^\mathrm{T}\mathbf{N}\,\mathrm{d}V - \int_\Omega \mathbf{B}^\mathrm{T} \frac{\partial \mathbf{H}_\beta}{\partial \mathbf{U}_\beta}\,\mathrm{d}V - \int_\Omega \mathbf{N}^\mathrm{T} \frac{\partial Q_\beta}{\partial \mathbf{U}_\beta}\,\mathrm{d}V\,, \tag{3.46a}$$

$$\mathbf{K}_{\beta\sigma} = \frac{\partial \mathbf{F}_\beta}{\partial \mathbf{U}_\sigma} = -\int_\Omega \mathbf{B}^\mathrm{T} \frac{\partial \mathbf{H}_\beta}{\partial \mathbf{U}_\sigma}\,\mathrm{d}V - \int_\Omega \mathbf{N}^\mathrm{T} \frac{\partial Q_\beta}{\partial \mathbf{U}_\sigma}\,\mathrm{d}V\,, \tag{3.46b}$$

$$\mathbf{K}_{\sigma\beta} = \frac{\partial \mathbf{F}_\sigma}{\partial \mathbf{U}_\beta} = -\int_\Omega \mathbf{B}^\mathrm{T} \frac{\partial \mathbf{H}_\sigma}{\partial \mathbf{U}_\beta}\,\mathrm{d}V - \int_\Omega \mathbf{N}^\mathrm{T} \frac{\partial Q_\sigma}{\partial \mathbf{U}_\beta}\,\mathrm{d}V\,, \tag{3.46c}$$

$$\mathbf{K}_{\sigma\sigma} = \frac{\partial \mathbf{F}_\sigma}{\partial \mathbf{U}_\sigma} = \int_\Omega \frac{c_\sigma \epsilon_\sigma}{\Delta t} \mathbf{N}^\mathrm{T}\mathbf{N}\,\mathrm{d}V - \int_\Omega \mathbf{B}^\mathrm{T} \frac{\partial \mathbf{H}_\sigma}{\partial \mathbf{U}_\sigma}\,\mathrm{d}V - \int_\Omega \mathbf{N}^\mathrm{T} \frac{\partial Q_\sigma}{\partial \mathbf{U}_\sigma}\,\mathrm{d}V\,. \tag{3.46d}$$

We express $\mathbf{X}$ in matrix form as

$$\mathbf{X} = \begin{bmatrix} \mathbf{B}\mathbf{U}_\beta \\ \mathbf{N}\mathbf{U}_\beta \\ \mathbf{B}\mathbf{U}_\sigma \\ \mathbf{N}\mathbf{U}_\sigma \end{bmatrix} \tag{3.47}$$

and thus define

$$\mathbf{\Phi}_\beta = \frac{\partial \mathbf{X}}{\partial \mathbf{U}_\beta} = \begin{bmatrix} \mathbf{B} \\ \mathbf{N} \\ \mathbf{0} \\ \mathbf{0} \end{bmatrix} \quad \text{and} \quad \mathbf{\Phi}_\sigma = \frac{\partial \mathbf{X}}{\partial \mathbf{U}_\sigma} = \begin{bmatrix} \mathbf{0} \\ \mathbf{0} \\ \mathbf{B} \\ \mathbf{N} \end{bmatrix}. \tag{3.48}$$

The tangent matrices for macroscale fluxes in Eq. (3.46) can therefore be computed as

$$\begin{aligned} \frac{\partial \mathbf{H}_\beta}{\partial \mathbf{U}_\beta} &= \mathbf{S}_\beta \mathbf{\Phi}_\beta, & \frac{\partial \mathbf{H}_\beta}{\partial \mathbf{U}_\sigma} &= \mathbf{S}_\beta \mathbf{\Phi}_\sigma, \\ \frac{\partial \mathbf{H}_\sigma}{\partial \mathbf{U}_\beta} &= \mathbf{S}_\sigma \mathbf{\Phi}_\beta, & \frac{\partial \mathbf{H}_\sigma}{\partial \mathbf{U}_\sigma} &= \mathbf{S}_\sigma \mathbf{\Phi}_\sigma, \end{aligned} \tag{3.49}$$

where matrices $\mathbf{S}_\beta$ and $\mathbf{S}_\sigma$ will be further derived in Section 3.4.3 and given in Eq. (3.71). The tangent matrices for macroscale sources in Eq. (3.46) can be computed as

$$\begin{aligned} \frac{\partial Q_\beta}{\partial \mathbf{U}_\beta} &= \mathbf{T}_\beta \mathbf{\Phi}_\beta, & \frac{\partial Q_\beta}{\partial \mathbf{U}_\sigma} &= \mathbf{T}_\beta \mathbf{\Phi}_\sigma, \\ \frac{\partial Q_\sigma}{\partial \mathbf{U}_\beta} &= \mathbf{T}_\sigma \mathbf{\Phi}_\beta, & \frac{\partial Q_\sigma}{\partial \mathbf{U}_\sigma} &= \mathbf{T}_\sigma \mathbf{\Phi}_\sigma, \end{aligned} \tag{3.50}$$

where matrices $\mathbf{T}_\beta$ and $\mathbf{T}_\sigma$ will also be derived in Section 3.4.3 via Eq. (3.72).

3.4.2 Finite element method for microscale problem

The weak form of the microscale governing equation (3.15) is

$$-\int_{V_\beta} \boldsymbol{\nabla}\,\delta u_\beta \cdot \left(-k_\beta \boldsymbol{\nabla} u_\beta\right) \mathrm{d}V + \int_{\Gamma_{\beta\mathrm{ex}} \cup \Gamma_{\beta\sigma}} \delta u_\beta\, \mathbf{h}_\beta \cdot \mathbf{n}_\beta \,\mathrm{d}\Gamma - \int_{V_\beta} \delta u_\beta\, b_\beta \,\mathrm{d}V = 0, \tag{3.51a}$$

$$-\int_{V_\sigma} \boldsymbol{\nabla}\,\delta u_\sigma \cdot \left(-k_\sigma \boldsymbol{\nabla} u_\sigma\right) \mathrm{d}V + \int_{\Gamma_{\sigma\mathrm{ex}} \cup \Gamma_{\sigma\beta}} \delta u_\sigma\, \mathbf{h}_\sigma \cdot \mathbf{n}_\sigma \,\mathrm{d}\Gamma - \int_{V_\sigma} \delta u_\sigma\, b_\sigma \,\mathrm{d}V = 0. \tag{3.51b}$$

The boundary terms on $\Gamma_{\beta_{\mathrm{ex}}} \cup \Gamma_{\beta\sigma}$ and $\Gamma_{\sigma_{\mathrm{ex}}} \cup \Gamma_{\sigma\beta}$ do not represent any prescribed Neumann boundary conditions but reflect unknown fluxes caused by the constraints of periodic boundary conditions (3.21) and temperature continuity condition (3.22) at the interface. The heat source terms containing b_β and b_σ are also not given but caused by the constraint of consistent temperatures across the macro- and micro-scales (3.23). All these constraints are enforced through the Lagrange multiplier method, and correspondingly we denote the heat fluxes due to the periodic boundary conditions (3.21) by $\lambda_{\beta,\mathrm{p}}$ and $\lambda_{\sigma,\mathrm{p}}$, the heat fluxes due to the temperature continuity condition (3.22) by $\lambda_{\beta\sigma}$ and $\lambda_{\sigma\beta}$ ($\lambda_{\sigma\beta} = -\lambda_{\beta\sigma}$), and the heat sources due to the consistent temperature constraint (3.23) by $\lambda_{\beta,\mathrm{b}}$ and $\lambda_{\sigma,\mathrm{b}}$. The weak form (3.51) is thus reformulated as

$$\int_{V_\beta} \boldsymbol{\nabla}\,\delta u_\beta \cdot \left(k_\beta \boldsymbol{\nabla} u_\beta\right) \mathrm{d}V + \int_{\Gamma_{\beta\mathrm{ex}}} \delta u_\beta\, \lambda_{\beta,\mathrm{p}} \,\mathrm{d}\Gamma + \int_{\Gamma_{\beta\sigma}} \delta u_\beta\, \lambda_{\beta\sigma} \,\mathrm{d}\Gamma - \int_{V_\beta} \delta u_\beta\, \lambda_{\beta,\mathrm{b}} \,\mathrm{d}V = 0, \tag{3.52a}$$

$$\int_{V_\sigma} \boldsymbol{\nabla}\,\delta u_\sigma \cdot \left(k_\sigma \boldsymbol{\nabla} u_\sigma\right) \mathrm{d}V + \int_{\Gamma_{\sigma\mathrm{ex}}} \delta u_\sigma\, \lambda_{\sigma,\mathrm{p}} \,\mathrm{d}\Gamma + \int_{\Gamma_{\sigma\beta}} \delta u_\sigma\, \lambda_{\sigma\beta} \,\mathrm{d}\Gamma - \int_{V_\sigma} \delta u_\sigma\, \lambda_{\sigma,\mathrm{b}} \,\mathrm{d}V = 0. \tag{3.52b}$$

The weak form (3.52) is further supplemented with the variational forms for the enforcement of the periodic boundary conditions (3.21) and temperature continuity condition (3.22):

$$\int_{\Gamma_{\beta_{\mathrm{ex}}} \cup \Gamma_{\sigma_{\mathrm{ex}}} \cup \Gamma_{\beta\sigma}} \delta\lambda\, A \,\mathrm{d}\Gamma = 0, \tag{3.53}$$

where A represents the left-hand formulations of periodic boundary conditions (3.21) and temperature continuity condition (3.22).

Inserting the discrete expressions of the field variables and their gradients into the weak

form (3.52) gives the discretized system of governing equations

$$\int_{V_\beta} \mathbf{B}^{\mathrm{T}} k_\beta \mathbf{B}\mathbf{u}_\beta \,\mathrm{d}V + \int_{\Gamma_{\beta\mathrm{ex}}} \mathbf{N}^{\mathrm{T}} \lambda_{\beta,\mathrm{p}} \,\mathrm{d}\Gamma + \int_{\Gamma_{\beta\sigma}} \mathbf{N}^{\mathrm{T}} \lambda_{\beta\sigma} \,\mathrm{d}\Gamma - \int_{V_\beta} \mathbf{N}^{\mathrm{T}} \lambda_{\beta,\mathrm{b}} \,\mathrm{d}V = \mathbf{0}, \tag{3.54a}$$

$$\int_{V_\sigma} \mathbf{B}^{\mathrm{T}} k_\sigma \mathbf{B}\mathbf{u}_\sigma \,\mathrm{d}V + \int_{\Gamma_{\sigma\mathrm{ex}}} \mathbf{N}^{\mathrm{T}} \lambda_{\sigma,\mathrm{p}} \,\mathrm{d}\Gamma - \int_{\Gamma_{\sigma\beta}} \mathbf{N}^{\mathrm{T}} \lambda_{\beta\sigma} \,\mathrm{d}\Gamma - \int_{V_\sigma} \mathbf{N}^{\mathrm{T}} \lambda_{\sigma,\mathrm{b}} \,\mathrm{d}V = \mathbf{0}. \tag{3.54b}$$

Conductivities k_β and k_σ are in general temperature dependent, and their derivatives need therefore to be considered in the calculation of the tangent matrices. The equations in Eq. (3.54) are solved in their own domains where each node has one degree of freedom, and the discretization at the interface between the two phases is conforming.

The discrete version of the constraints of the periodic boundary conditions (3.21) and temperature continuity condition (3.22) is obtained from Eq. (3.53) by means of the point collocation method [38] and expressed in Eqs. (3.79) to (3.81). The constraint (3.23) is directly discretized by inserting discrete expressions of the field variables and expressed in Eq. (3.82). These boundary conditions and constraints, listed in Eqs. (3.79) to (3.82), are expressed in matrix form as

$$\mathbf{A}\mathbf{u} + \mathbf{C}\mathbf{X} = \mathbf{0}, \tag{3.55}$$

where $\mathbf{u}$ collects all the nodal unknowns as concatenation of vectors $\mathbf{u}_\beta$ and $\mathbf{u}_\sigma$

$$\mathbf{u} = \begin{bmatrix} \mathbf{u}_\beta & \mathbf{u}_\sigma \end{bmatrix}^{\mathrm{T}}, \tag{3.56}$$

and $\mathbf{A}$ and $\mathbf{C}$ are constant coefficient matrices that can be readily obtained after sorting Eqs. (3.79) to (3.82) consistently with $\mathbf{u}$.

The Lagrange multipliers $\lambda_{\beta,\mathrm{p}}$, $\lambda_{\sigma,\mathrm{p}}$, and $\lambda_{\beta\sigma}$ representing heat fluxes on the boundaries and interface are discretized in the process of deriving Eqs. (3.79) to (3.81) and stacked together with the two scalar Lagrange multipliers $\lambda_{\beta,\mathrm{b}}$ and $\lambda_{\sigma,\mathrm{b}}$ in the vector form as $\boldsymbol{\lambda}$. The vector of Lagrange multipliers is then associated with the nodal unknowns $\mathbf{u}$ in Eq. (3.56):

$$\mathbf{w} = [\mathbf{u}\ \boldsymbol{\lambda}]^{\mathrm{T}}.$$

The system of nonlinear equations Eq. (3.54) augmented by Eq. (3.55) is solved by the Newton-Raphson iteration scheme. To this end, we assemble the first terms in Eq. (3.54a) and Eq. (3.54b) as

$$\mathbf{f} = \begin{bmatrix} \int_{V_\beta} \mathbf{B}^{\mathrm{T}} k_\beta \mathbf{B}\mathbf{u}_\beta \,\mathrm{d}V \\ \int_{V_\sigma} \mathbf{B}^{\mathrm{T}} k_\sigma \mathbf{B}\mathbf{u}_\sigma \,\mathrm{d}V \end{bmatrix}. \tag{3.57}$$

At iteration step k, the increment of the solution $\Delta\mathbf{w}^{k+1}$ can be computed from

$$\begin{bmatrix} \mathbf{K} & \mathbf{A}^{\mathrm{T}} \\ \mathbf{A} & \mathbf{0} \end{bmatrix} \begin{bmatrix} \Delta\mathbf{u} \\ \Delta\boldsymbol{\lambda} \end{bmatrix} + \begin{bmatrix} \mathbf{f} + \mathbf{A}^{\mathrm{T}}\boldsymbol{\lambda} \\ \mathbf{A}\mathbf{u} + \mathbf{C}\mathbf{X} \end{bmatrix} = \mathbf{0}, \tag{3.58}$$

where we have omitted the iteration index for clarity, and the tangent matrix

$$\mathbf{K} = \frac{\partial \mathbf{f}}{\partial \mathbf{u}}. \tag{3.59}$$

3.4.3 Upscaling of macroscale quantities

This section details the calculation of the homogenized fluxes ($\mathbf{H}_\beta$ and $\mathbf{H}_\sigma$), the macroscale heat sources (Q_β and Q_σ), and the tangent matrices ($\mathbf{S}_\beta$, $\mathbf{S}_\sigma$, $\mathbf{T}_\beta$, and $\mathbf{T}_\sigma$) based on the microscale finite element solution. By comparison of Eqs. (3.54) and (3.58), the Lagrange multipliers $\boldsymbol{\lambda}$ that pertain to the periodic boundary conditions and temperature continuity condition represent the integrals of heat fluxes over the area of influence of each node at the boundary/interface. According to Eq. (3.30), the macroscale fluxes can be calculated through Lagrange multipliers as:

$$\mathbf{H}_\beta = \frac{1}{V}\int_{\Gamma_{\beta_{\mathrm{ex}}}} \left(\mathbf{x}_{\mathrm{m}}\,\mathbf{N}^{\mathrm{T}}\right)\lambda_{\beta,\mathrm{p}}\,\mathrm{d}A = \frac{1}{V}\,\mathbf{x}_{\mathrm{m}}\int_{\Gamma_{\beta_{\mathrm{ex}}}} \mathbf{N}^{\mathrm{T}}\lambda_{\beta,\mathrm{p}}\,\mathrm{d}A = \frac{1}{V}\,\mathbf{x}_{\mathrm{m}}\,\mathbf{A}^{\mathrm{T}}\boldsymbol{\lambda}_{\beta,\mathrm{p}}, \tag{3.60a}$$

$$\mathbf{H}_\sigma = \frac{1}{V}\int_{\Gamma_{\sigma_{\mathrm{ex}}}} \left(\mathbf{x}_{\mathrm{m}}\,\mathbf{N}^{\mathrm{T}}\right)\lambda_{\sigma,\mathrm{p}}\,\mathrm{d}A = \frac{1}{V}\,\mathbf{x}_{\mathrm{m}}\int_{\Gamma_{\sigma_{\mathrm{ex}}}} \mathbf{N}^{\mathrm{T}}\,\lambda_{\sigma,\mathrm{p}}\,\mathrm{d}A = \frac{1}{V}\,\mathbf{x}_{\mathrm{m}}\,\mathbf{A}^{\mathrm{T}}\boldsymbol{\lambda}_{\sigma,\mathrm{p}}, \tag{3.60b}$$

where matrix

$$\mathbf{x}_{\mathrm{m}} = \begin{bmatrix} x_1^{(1)} & x_1^{(2)} & \cdots & x_1^{(n_{\mathrm{m}})} \\ x_2^{(1)} & x_2^{(2)} & \cdots & x_2^{(n_{\mathrm{m}})} \end{bmatrix} \tag{3.61}$$

lists the coordinates of all the n_{m} nodes of the microscale mesh, $\boldsymbol{\lambda}_{\beta,\mathrm{p}}$ and $\boldsymbol{\lambda}_{\sigma,\mathrm{p}}$ refer to the components of $\boldsymbol{\lambda}$ that are associated with the periodic boundary conditions (Eqs. (3.79) and (3.80)) imposed on $\Gamma_{\beta_{\mathrm{ex}}}$ and on $\Gamma_{\sigma_{\mathrm{ex}}}$, respectively. With an abuse of notation, the coefficient matrix $\mathbf{A}^{\mathrm{T}}$ in Eq. (3.55) needs to be recast here to accommodate $\boldsymbol{\lambda}_{\beta,\mathrm{p}}$ and $\boldsymbol{\lambda}_{\sigma,\mathrm{p}}$.

The macroscale heat sources due to interfacial heat transfer are computed according to

Eqs. (3.9) and (3.13) as

$$Q_\beta = -\frac{1}{V}\int_{\Gamma_{\beta\sigma}} \lambda_{\beta\sigma}\,\mathrm{d}A = -\frac{1}{V}\sum^{\Gamma_{\beta\sigma}} \mathbf{A}^{\mathrm{T}}\boldsymbol{\lambda}_{\beta\sigma}, \tag{3.62a}$$

$$Q_\sigma = -\frac{1}{V}\int_{\Gamma_{\sigma\beta}} \lambda_{\sigma\beta}\,\mathrm{d}A = -\frac{1}{V}\sum^{\Gamma_{\sigma\beta}} \mathbf{A}^{\mathrm{T}}\boldsymbol{\lambda}_{\beta\sigma}, \tag{3.62b}$$

where $\boldsymbol{\lambda}_{\beta\sigma}$ denotes components of $\boldsymbol{\lambda}$ related to the temperature continuity condition (3.81) imposed on nodes on $\Gamma_{\beta\sigma}$ and $\Gamma_{\sigma\beta}$ ($\lambda_{\sigma\beta}$ not discretized). Also, the coefficient matrix $\mathbf{A}^{\mathrm{T}}$ in Eq. (3.55) is shrunk to accommodate $\boldsymbol{\lambda}_{\beta\sigma}$ but is different in Eqs. (3.62a) and (3.62b) because of different nodes on $\Gamma_{\beta\sigma}$ and $\Gamma_{\sigma\beta}$. The coefficient matrices in Eqs. (3.62a) and (3.62b) however ensures that $Q_\beta + Q_\sigma = 0$. In Eqs. (3.60) and (3.62), all the Lagrange multipliers take the values at the converged state of the microscale iteration.

The tangent matrices are derived as follows. At a converged state, the increment $\Delta\mathbf{w}$ in Eq. (3.58) is zero, and hence the residual vector

$$\hat{\mathbf{f}} = \begin{bmatrix} \mathbf{f} + \mathbf{A}^{\mathrm{T}}\boldsymbol{\lambda} \\ \mathbf{A}\mathbf{u} + \mathbf{C}\mathbf{X} \end{bmatrix} = \mathbf{0}. \tag{3.63}$$

We then apply a small variation $\delta\mathbf{X}$ to the macroscale quantities $\mathbf{X}$ and compute the corresponding change in the microscale solution. Note that Eq. (3.63) should always hold to get the converged microscale solution. Therefore, we have

$$\delta\hat{\mathbf{f}} = \mathbf{0} = \begin{bmatrix} \mathbf{K} & \mathbf{A}^{\mathrm{T}} \\ \mathbf{A} & \mathbf{0} \end{bmatrix} \begin{bmatrix} \delta\mathbf{u} \\ \delta\boldsymbol{\lambda} \end{bmatrix} + \begin{bmatrix} \mathbf{0} \\ \mathbf{C} \end{bmatrix} \delta\mathbf{X}\,. \tag{3.64}$$

Rearranging Eq. (3.64), we obtain

$$\begin{bmatrix} \mathbf{K} & \mathbf{A}^{\mathrm{T}} \\ \mathbf{A} & \mathbf{0} \end{bmatrix} \begin{bmatrix} \delta\mathbf{u} \\ \delta\boldsymbol{\lambda} \end{bmatrix} = -\begin{bmatrix} \mathbf{0} \\ \mathbf{C} \end{bmatrix} \delta\mathbf{X}\,. \tag{3.65}$$

To solve Eq. (3.65), we rewrite it as

$$\hat{\mathbf{K}}\,\delta\mathbf{w} = \hat{\mathbf{C}}\,\delta\mathbf{X} \tag{3.66}$$

and thus the variation $\delta\mathbf{w}$ is expressed as

$$\delta\mathbf{w} = \hat{\mathbf{K}}^{-1}\hat{\mathbf{C}}\,\delta\mathbf{X}\,, \tag{3.67}$$

where $\hat{\mathbf{K}}^{-1}$ must be evaluated at the converged state of the microscale iteration. The solution

$\delta\boldsymbol{\lambda}$ is extracted from $\delta\mathbf{w}$ by means of the gather matrix $\boldsymbol{\delta}$:

$$\delta\boldsymbol{\lambda} = \boldsymbol{\delta}\,\delta\mathbf{w}\,. \tag{3.68}$$

According to Eqs. (3.67) and (3.68), the variations of the homogenized fluxes (3.60) can be formulated as

$$\delta\mathbf{H}_\beta = \frac{1}{V}\,\mathbf{x}_\mathrm{m}\,\mathbf{A}^\mathrm{T}\,\delta\boldsymbol{\lambda}_{\beta,\mathrm{p}} = \frac{1}{V}\,\mathbf{x}_\mathrm{m}\,\mathbf{A}^\mathrm{T}\boldsymbol{\delta}_{\beta,\mathrm{p}}\,\hat{\mathbf{K}}^{-1}\hat{\mathbf{C}}\,\delta\mathbf{X}\,, \tag{3.69a}$$

$$\delta\mathbf{H}_\sigma = \frac{1}{V}\,\mathbf{x}_\mathrm{m}\,\mathbf{A}^\mathrm{T}\,\delta\boldsymbol{\lambda}_{\sigma,\mathrm{p}} = \frac{1}{V}\,\mathbf{x}_\mathrm{m}\,\mathbf{A}^\mathrm{T}\boldsymbol{\delta}_{\sigma,\mathrm{p}}\,\hat{\mathbf{K}}^{-1}\hat{\mathbf{C}}\,\delta\mathbf{X}\,, \tag{3.69b}$$

where $\boldsymbol{\delta}_{\beta,\mathrm{p}}$ and $\boldsymbol{\delta}_{\sigma,\mathrm{p}}$ are the gather matrices used to retrieve $\boldsymbol{\lambda}_{\beta,\mathrm{p}}$ and $\boldsymbol{\lambda}_{\sigma,\mathrm{p}}$, respectively, from $\boldsymbol{\lambda}$. The variations of the macroscale heat sources (3.62) due to interfacial heat transfer are calculated as

$$\delta Q_\beta = -\frac{1}{V}\sum^{\Gamma_{\beta\sigma}}\mathbf{A}^\mathrm{T}\,\delta\boldsymbol{\lambda}_{\beta\sigma} = -\frac{1}{V}\sum^{\Gamma_{\beta\sigma}}\mathbf{A}^\mathrm{T}\boldsymbol{\delta}_{\beta\sigma}\,\hat{\mathbf{K}}^{-1}\hat{\mathbf{C}}\,\delta\mathbf{X}\,, \tag{3.70a}$$

$$\delta Q_\sigma = -\frac{1}{V}\sum^{\Gamma_{\sigma\beta}}\mathbf{A}^\mathrm{T}\,\delta\boldsymbol{\lambda}_{\beta\sigma} = -\frac{1}{V}\sum^{\Gamma_{\sigma\beta}}\mathbf{A}^\mathrm{T}\boldsymbol{\delta}_{\beta\sigma}\,\hat{\mathbf{K}}^{-1}\hat{\mathbf{C}}\,\delta\mathbf{X}\,, \tag{3.70b}$$

where $\boldsymbol{\delta}_{\beta\sigma}$ is the gather matrix used to retrieve $\boldsymbol{\lambda}_{\beta\sigma}$ from $\boldsymbol{\lambda}$. The tangent matrices for the macroscale heat fluxes are calculated as

$$\mathbf{S}_\beta = \frac{\delta\mathbf{H}_\beta}{\delta\mathbf{X}} = \frac{1}{V}\,\mathbf{x}_\mathrm{m}\,\mathbf{A}^\mathrm{T}\boldsymbol{\delta}_{\beta,\mathrm{p}}\,\hat{\mathbf{K}}^{-1}\hat{\mathbf{C}}, \tag{3.71a}$$

$$\mathbf{S}_\sigma = \frac{\delta\mathbf{H}_\sigma}{\delta\mathbf{X}} = \frac{1}{V}\,\mathbf{x}_\mathrm{m}\,\mathbf{A}^\mathrm{T}\boldsymbol{\delta}_{\sigma,\mathrm{p}}\,\hat{\mathbf{K}}^{-1}\hat{\mathbf{C}}, \tag{3.71b}$$

and the tangent matrices for the macroscale heat sources due to interfacial heat transfer are expressed as

$$\mathbf{T}_\beta = \frac{\delta Q_\beta}{\delta\mathbf{X}} = -\frac{1}{V}\sum^{\Gamma_{\beta\sigma}}\mathbf{A}^\mathrm{T}\boldsymbol{\delta}_{\beta\sigma}\,\hat{\mathbf{K}}^{-1}\hat{\mathbf{C}}, \tag{3.72a}$$

$$\mathbf{T}_\sigma = \frac{\delta Q_\sigma}{\delta\mathbf{X}} = -\frac{1}{V}\sum^{\Gamma_{\sigma\beta}}\mathbf{A}^\mathrm{T}\boldsymbol{\delta}_{\beta\sigma}\,\hat{\mathbf{K}}^{-1}\hat{\mathbf{C}}. \tag{3.72b}$$

3.5 Results and discussion

We first present some numerical examples for the purpose of validation in Section 3.5.1 where the FE^2 simulation results are compared with the results of the single-scale simulation (reference solutions). The numerical examples are tailored to show noticeable temperature

Table 3.1. Parameters of the FE^2 multiscale and single-scale simulations for Fig. 3.4.

		quantity	symbol	unit	phase β	phase σ
FE^2	macro	volume fraction	ϵ	-	0.67	0.33
		volumetric heat capacity	c	$J/(m^3\,K)$	3.51×10^6	3.51×10^6
		volume-averaged heat source[a]	R	W/m^3	0.0	2.99×10^7
	micro	conductivity	k	$W/(m\,K)$	1.0	4.0×10^2
Single-scale		volumetric heat capacity	c	$J/(m^3\,K)$	3.51×10^6	3.51×10^6
		volumetric heat source	r	W/m^3	0.0	9.0×10^7
		conductivity	k	$W/(m\,K)$	1.0	4.0×10^2

[a] This quantity is calculated according to Eq. (3.6) or (3.12).

difference between the two phases and thus to demonstrate the capability of the FE^2 framework in solving the two-equation model. The first example (Section 3.5.1) focuses on the interfacial heat transfer between the two phases, which cannot be captured by the one-equation model [27, 31], and ignores the spatial diffusion at the macroscale by having a uniform macroscale temperature field. The macroscale spatial heat fluxes are then considered in the second example (Section 3.5.1) that considers both the linear and nonlinear conduction and in the third example (Section 3.5.1) that features a significant conductivity difference. Finally, the microscale RVE simulation results are discussed in Section 3.5.2 to offer some insights into the interfacial heat transfer coefficient and the microscopic length scale effects.

3.5.1 Comparison with single-scale simulations

Interfacial heat transfer

Consider the insulated two-phase slab problem studied by Ramos et al. [31] using a one-equation model. As shown in Fig. 3.3, the two-phase slab consists of a regular array of 140×70 unit cells, with each unit cell consisting of an inclusion (σ phase) embedded in a matrix (β phase). Both phases are isotropic and have constant but different conductivities whose values are listed in Table 3.1 together with other simulation parameters. The insulated boundary condition $\mathbf{h} = \mathbf{0}$ for $t \in (0, t_{\text{end}}]$ is imposed at the boundary, and the initial condition $u_0 = 0\,°C$ is enforced in the whole domain. The simulation time is $t_{\text{end}} = 30\,s$.

The insulated boundary condition generates a homogeneous temperature field at the macroscale. We can therefore safely use a single square bilinear quadrilateral element with edge length of 0.1 m as the macroscale mesh (Fig. 3.3c). At each integration point of the macroscale element, we take one unit cell as the corresponding RVE. For the single-scale simulation we employ a single unit cell due to the expected homogeneity of the solution fields. From the single-scale simulation, the intrinsic average of the temperatures of the

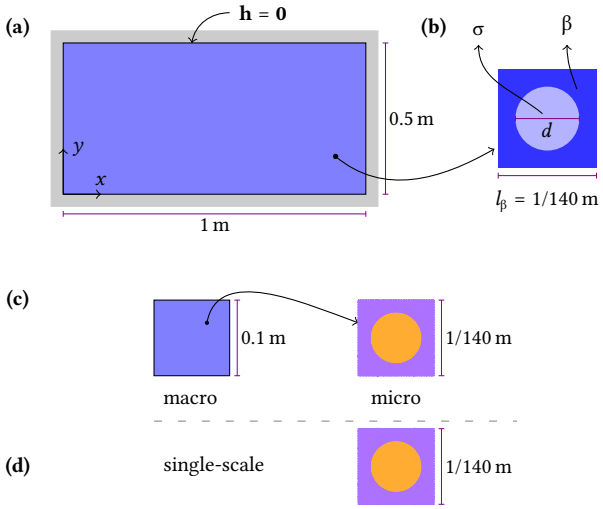

Fig. 3.3. An insulated two-phase slab (a) with width 1 m and height 0.5 m. The slab consists of a regular arrangement of unit cells (140 × 70); each unit cell (b) with edge length $l_\beta = 1/140$ m consists of two phases (β and σ). The diameter of the inclusion (σ phase) is $d = 0.65\ l_\beta$. The initial temperature is 0 °C everywhere and heat is generated in the σ phase; all the parameters are listed in Table 3.1. Panel (c) shows the computational mesh for the FE² method: a square bilinear quadrilateral element is used for the macroscale mesh and 2436 linear triangular elements for the RVE mesh. The single-scale discretization of a unit cell in panel (d) is the same as that of the RVE.

β and σ phases over the unit cell are defined as $\bar{u}_\beta$ and $\bar{u}_\sigma$, according to Eq. (3.77), and serve as references for the two macroscale solutions U_β and U_σ, respectively. Moreover, the average temperature $\bar{u}$ of the whole unit cell, defined as

$$\bar{u} = \epsilon_\beta \bar{u}_\beta + \epsilon_\sigma \bar{u}_\sigma, \tag{3.73}$$

is compared to the solution of the one-equation model in Eq. (3.32), which is independently obtained from the FE² method and not calculated as the weighted average of U_β and U_σ by Eq. (3.36).

The FE² simulation results are compared with results from the single-scale simulation in Fig. 3.4. The macroscale temperature fields U_β and U_σ, defined in Eqs. (3.4) and (3.11), agree with the average temperatures $\bar{u}_\beta$ and $\bar{u}_\sigma$ predicted by the single-scale simulation (Fig. 3.4a), respectively. The macroscale temperature U obtained with the one-equation model agrees with the average temperature $\bar{u}$ of the whole unit cell obtained with the single-scale simulation. As $\bar{u}$ is the weighted average of $\bar{u}_\beta$ and $\bar{u}_\sigma$ (Eq. (3.73)), it is inferred that U matches with the weighted average of U_β and U_σ: Eq. (3.36) holds. This agreement numerically validates the relation between the two models: the one-equation model is a special case of the two-equation model, as shown in Section 3.3.5.

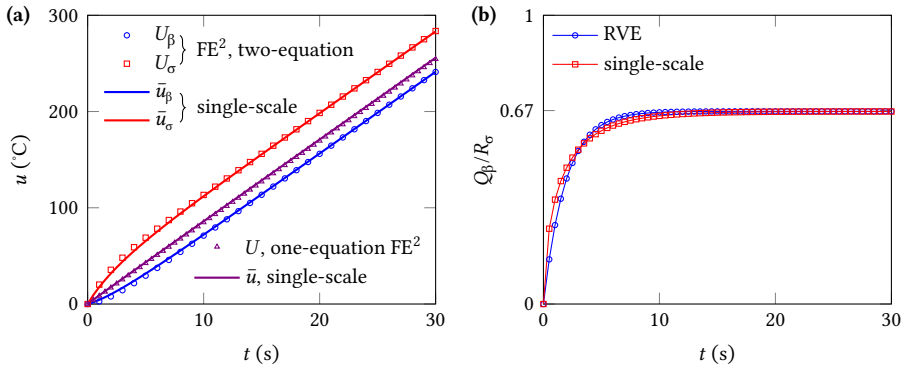

Fig. 3.4. Comparison between the FE^2 simulation results and the results of the single-scale simulations. (a) Temperature increases with time due to the heat generation in the inclusion. The macroscale temperatures U_β and U_σ are obtained from the two-equation model with the FE^2 framework, while U is from the one-equation model. The average temperatures $\overline{u}_\beta$ and $\overline{u}_\sigma$ are intrinsic averages over the β and σ phases of the unit cell, respectively, and $\overline{u}$ refers to the average over the whole unit cell as defined in Eq. (3.73). (b) Volumetric interfacial heat transfer Q_β normalized by the given volume-averaged heat source R_σ (Table 3.1).

Fig. 3.4b shows the temporal evolution of the interfacial heat transfer Q_β (Eq. (3.9)) normalized by the given heat source R_σ (Eq. (3.12)): it increases sharply in the beginning and then quickly stabilizes. In this example, the heat is generated in the σ phase and partially flows into the β phase, increasing the temperatures of both phases simultaneously. The normalized interfacial heat transfer measures the fraction of the heat generation R_σ that goes to the matrix (the β phase). In the plateau stage, the normalized heat transfer converges to the volume fraction of the β phase, suggesting that the distribution of the heat generation between the two phases reaches an equilibrium and is determined by the volume fraction. Again, the agreement between the FE^2 simulation results and results of the single-scale simulation validates the computational framework for the two-equation model.

Actually, the temperature difference between the two phases, as shown above, is also of interest to Ramos et al. [31] and shown in Fig. 12 of their paper. However, since they used the one-equation model, the temperature difference at the macroscale was not presented; instead, they reported the temperatures of a "hot" point in the σ phase and a "cold" point in the β phase of an RVE.

The temperature profile in an RVE (Fig. 3.5a) by our FE^2 simulation also resembles the temperature profile in the unit cell (Fig. 3.5b) obtained with the single-scale simulation. The temperature variation in each phase can be reproduced in our two-equation model thanks to the transfer of the two macroscale temperatures to the microscale RVE (Eq. (3.23)) and the microscale boundary conditions. The one-equation model will however yield a uniform RVE temperature field as shown in Fig. 13a of Ramos et al. [31] unless the microscale transient effect is taken into account (Fig. 13b of Ramos et al. [31]).

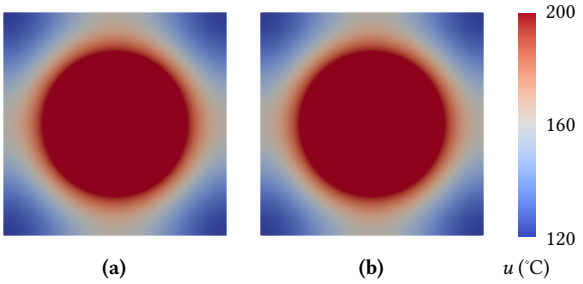

Fig. 3.5. Temperature profile at $t = 20\,\mathrm{s}$ in (a) an RVE from the microscale FE simulation and (b) in the unit cell from the single-scale simulation.

Nonlinear heat conduction

This example considers the same two-phase medium as in Fig. 3.3a and b but with different boundary conditions in order to allow for heat conduction at the macroscale, as shown in Fig. 3.6a. Neumann boundary conditions are enforced at the horizontal edges, while Dirichlet boundary conditions are imposed at the vertical edges:

$$\begin{aligned} &\mathbf{h}|_{y=0} = \mathbf{0}, \qquad \mathbf{h}|_{y=0.5\ \mathrm{m}} = \mathbf{0} \quad \text{and} \\ &u|_{x=0} = 0\,^{\circ}\mathrm{C}, \quad u|_{x=1\ \mathrm{m}} = 300\,^{\circ}\mathrm{C} \quad \text{for } t \in (0, t_{\mathrm{end}}], \end{aligned}$$

where $t_{\mathrm{end}} = 288\,\mathrm{s}$. The initial condition $u_0 = 0\,^{\circ}\mathrm{C}$ is enforced in the whole domain. As these boundary conditions ensure a uniform macroscale temperature field along the y direction, we only consider one row of 40 bilinear quadrilateral elements for the macroscale mesh (Fig. 3.6b). For the RVE we use one unit cell, the same as in Fig. 3.3c. Considering the insulated top and bottom boundaries, we also simulate one layer of unit cells for the single-scale simulation (i.e., 140 side-by-side unit cells as shown in Fig. 3.6c). Each unit cell has the same mesh as the RVE.

To have distinct temperatures difference between the two phases, a heat source in the σ phase is also contained to maintain the local thermal non-equilibrium condition [3, 12]. This scenario is analogous to the real transport problem with reaction sources in the biofilm phase in chemical engineering applications [5, 6] where a local mass non-equilibrium condition arises. As the FE^2 method is advantageous in addressing general constitutive relations, here we not only simulate the linear conduction problem with constant conductivities but also nonlinear conduction problem with temperature-dependent conductivities. The corresponding parameters are listed in Table 3.2.

As shown in Fig. 3.7, the FE^2 simulation results can capture the temperature distribution and evolution in the two phases and agree well with the results of the single-scale simulation

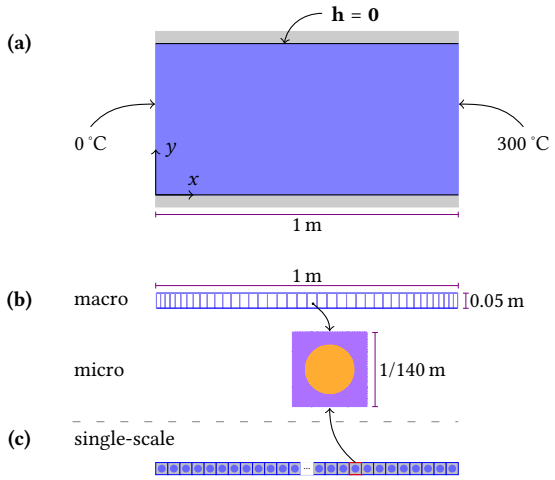

Fig. 3.6. (a) The same two-phase slab as in Fig. 3.3, but with different boundary conditions. In this case the slab is insulated at the upper and lower edges and constant temperatures are applied at the left- and right-hand edges. The initial temperature is 0 °C everywhere. (b) For the FE^2 simulation, the macroscale mesh consists of 40 bilinear quadrilateral elements and the mesh is denser at the two sides; the microscale RVE mesh is the same as the RVE mesh in Fig. 3.3. (c) The single-scale simulation is performed on a mesh consisting of a layer of 140 side-by-side unit cells, each discretized as the RVE.

Table 3.2. Parameters of the FE^2 multiscale and single-scale simulations for Fig. 3.7.

		quantity	symbol	unit	phase β	phase σ
FE^2	macro	volume fraction	ϵ	-	0.67	0.33
		volumetric heat capacity	c	$J/(m^3\,K)$	1.76×10^7	1.76×10^7
		volume-averaged heat source	R	W/m^3	0.0	2.99×10^7
	micro	conductivity[a]	k	$W/(m\,K)$	$400 + k_0 T$	$1 + k_1 T$
Single-scale		volumetric heat capacity	c	$J/(m^3\,K)$	1.76×10^7	1.76×10^7
		volumetric heat source	r	W/m^3	0.0	9.0×10^7
		conductivity[a]	k	$W/(m\,K)$	$400 + k_0 T$	$1 + k_1 T$

[a] Coefficients $k_0 = k_1 = 0$ for the linear conduction case while $k_0 = 4$ and $k_1 = 0.01$ for the nonlinear conduction case; T is the value of temperature measured in degrees Celsius and ranges from 0 to 400.

for both the linear and nonlinear conduction cases. In Fig. 3.7a and c for the linear conduction case, the temperature of the slab continuously increases because of the heat generated in the σ phase but remains constant at the left- and right-hand boundaries as specified. Two typical time instants are selected to show the evolution of the temperature profile. At 72 s, the temperature increase due to the heat generation is uniform in the middle (from 0.1 to 0.9 m) of the slab; close to the two vertical edges of the slab, high temperature gradients develop due to the boundary condition of fixed temperatures. At 144 s, a temperature peak is observed near the right-hand vertical edge because the heat accumulated from the heat source cannot be fluxed out timely. In the FE^2 simulation, the boundary conditions of fixed temperatures at the two vertical edges (Fig. 3.6a) are only applied to the β phase at the macroscale; for the σ phase, the leftmost and rightmost boundaries are also insulated and its temperature U_σ is determined by the interaction with the β phase as well as the internal heat generation. This setting enables the FE^2 method to capture the phenomenon that the temperatures of the σ phase at the two vertical edges are higher than those of the β phase.

The arguments exposed above also apply to the case of nonlinear conduction as shown in Fig. 3.7b and d, with minor differences. According to Table 3.2, the conductivities in the nonlinear case are always higher than those in the linear case, and thus the temperature differences between the two phases are smaller and the temperature gradients near the two vertical edges are lower (Fig. 3.7a vs b and Fig. 3.7c vs d). At each time instant, the weighted averages of U_β and U_σ according to Eq. (3.36) in the middle of the slab however remain unchanged for the linear and nonlinear cases because they are determined by the heat generation and can be manually calculated and checked.

Significant conductivity difference

We further consider another scenario that does not include a heat source but features a significant difference in the conductivity between the two phases, also resulting in a temperature difference. The same problem setting as in Fig. 3.6 is used here but a different set of parameters is taken and listed in Table 3.3. This situation is representative of the heat transfer into a composite material composed of a highly conductive matrix but poorly conductive inclusions. A certain amount of time is necessary before both phases attain the same temperature [15].

Fig. 3.8 shows the simulation results of the FE^2 method and the single-scale approach. The fixed temperature at the right-hand side is higher than the initial null temperature of the whole slab, leading to heat influx at the right-hand side as time passes. Since the matrix (β phase) is much more conductive than the inclusion (σ phase), the matrix's temperature is always higher than the temperature of the inclusion, to the extent that an evident temperature difference is observed. At two time instants, the FE^2 simulation results agree with those by the single-scale simulation, validating the FE^2 multiscale framework for the two-equation

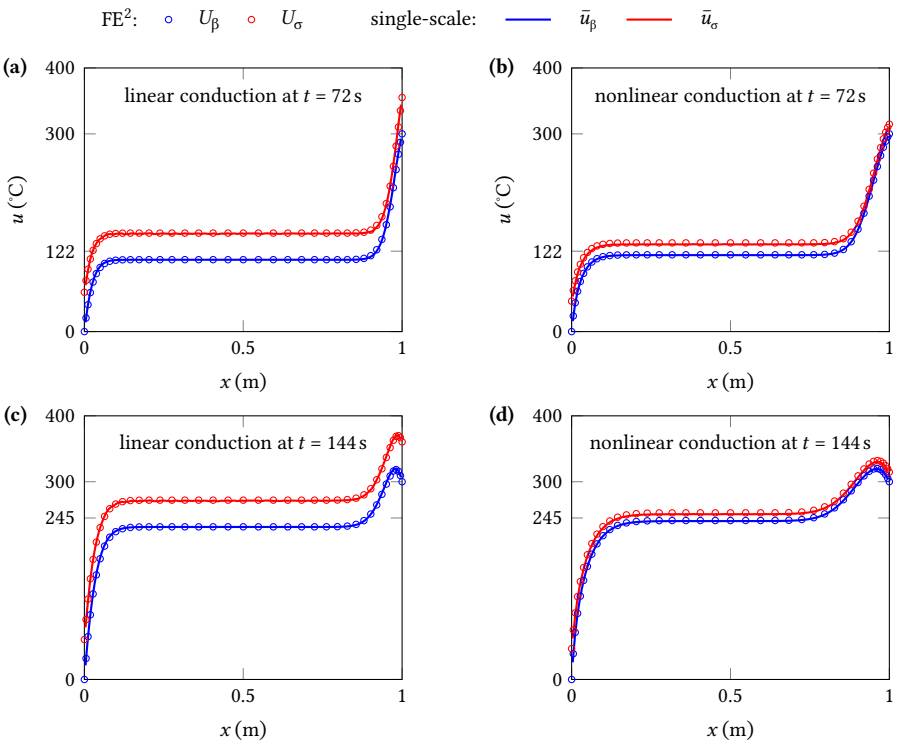

Fig. 3.7. Comparison between the FE^2 and single-scale simulation results. Panels (a) and (c) show the results for the linear conduction case and panels (c) and (d) for the nonlinear conduction case. Quantities U_β and U_σ refer to the macroscale solutions (FE^2 method), while $\bar{u}_\beta$ and $\bar{u}_\sigma$ indicate the intrinsic averages of the temperature in each phase (single-scale approach).

Table 3.3. Parameters of the FE^2 multiscale and single-scale simulations for Fig. 3.8.

		quantity	symbol	unit	phase β	phase σ
FE^2	macro	volume fraction	ϵ	-	0.67	0.33
		volumetric heat capacity	c	J/(m^3 K)	1.76×10^7	1.76×10^7
		volume-averaged heat source	R	W/m^3	0.0	0.0
	micro	conductivity	k	W/(m K)	4.0×10^3	1.0×10^{-1}
Single-scale		volumetric heat capacity	c	J/(m^3 K)	1.76×10^7	1.76×10^7
		volumetric heat source	r	W/m^3	0.0	0.0
		conductivity	k	W/(m K)	4.0×10^3	1.0×10^{-1}

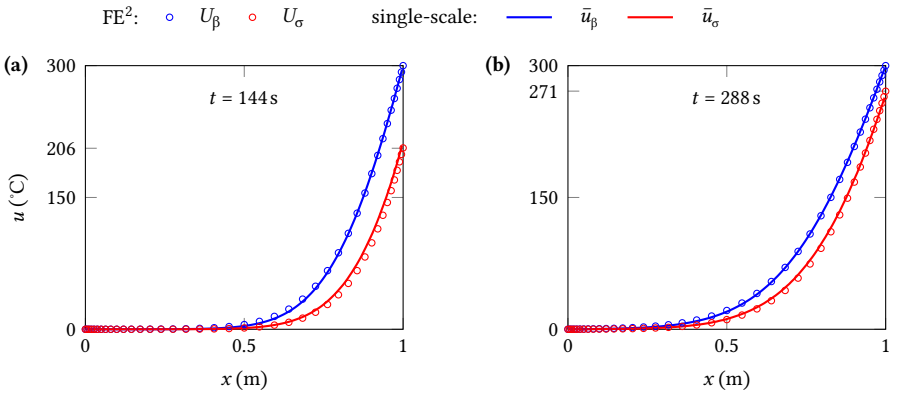

Fig. 3.8. Comparison between the FE^2 and single-scale simulation results for the conduction problem characterized by a significant conductivity difference in the two phases. Quantities U_β and U_σ refer to the macroscale solutions (FE^2 method), while $\bar{u}_\beta$ and $\bar{u}_\sigma$ indicate the intrinsic averages of the temperature in each phase (single-scale approach).

model.

3.5.2 Insights from microscale RVE simulations

In the previous simulations of linear conduction problems, we observe that in the tangent vector $\mathbf{T}_\beta$ (Eq. (3.72)), the third component that shows dependence of the interfacial heat flow on U_β is always the additive inverse of the sixth component that shows dependence on U_σ: $\mathbf{T}_\beta^{(3)} + \mathbf{T}_\beta^{(6)} = 0$. This relation is also observed, as expected, in $\mathbf{T}_\sigma$. The other components are relatively negligible, implying almost no temperature gradient dependence of the interfacial heat flow. Moreover, the components of $\mathbf{T}_\beta$ themselves are independent of the macroscale temperatures U_β and U_σ. These observations suggest that the volumetric interfacial heat flow Q_β as defined in Eq. (3.9) linearly depends on the temperature difference between the two phases according to the relationship

$$Q_\beta = T_\mathrm{h} \left(U_\sigma - U_\beta \right), \tag{3.74}$$

where T_h is usually referred to as the interfacial heat transfer coefficient [1, 3, 4]. The linear dependence in Eq. (3.74) can also be deduced from the results reported in Fig. 3.4: the ratio between Q_β and $U_\beta - U_\sigma$ yields, at each time step, the same coefficient T_h values. Although the linear relation (3.74) has been widely used in the homogenized transport equations in the two-equation model [1, 4, 9], the estimation of the heat transfer coefficient value is however still challenging [8] either in experimental measurements [4] or by analytical approaches [1]. Our numerical results suggest that the heat transfer coefficient is indeed constant for a linear two-phase system. The microscale RVE simulation thus numerically validates the

widely-used linear relation and, more importantly, offers a convenient way to calculate the heat transfer coefficient.

The relation $\mathbf{T}_\beta^{(3)} + \mathbf{T}_\beta^{(6)} = 0$ observed in the linear examples however breaks down in the nonlinear conduction case and the linear relation (3.74) does not hold. The heat transfer coefficient defined in the linear case actually depends on the specific conductivities of both phases. In nonlinear conduction problems, the temperature dependent conductivity naturally leads to temperature dependent coefficients $\mathbf{T}_\beta^{(3)}$ and $\mathbf{T}_\beta^{(6)}$. Compared to the numerical approach by Quintard and Whitaker [1], the proposed FE^2 framework has the intrinsic advantage of addressing nonlinear conduction problems because the interfacial heat transfer as well as its dependence on macroscale field variables are numerically calculated from the microscale problem, avoiding the postulation of relation (3.74) and the wide range of values reported for the heat transfer coefficient [8].

In conventional FE^2 frameworks for the one-equation model, the effective conductivity of the whole RVE is generally not affected by the microscopic length scale, given that material properties of each phase are fixed. An analogous situation arises in computational solid mechanics: the homogenized stiffness (deformation gradient dependence of the homogenized stress) does not depend on the unit cell size. This microscopic length scale independence is also true for the tangent matrices ($\mathbf{S}_\beta$ and $\mathbf{S}_\sigma$) characterizing the temperature gradient dependence of the homogenized flux, provided that volume fraction and conductivity of each phase are fixed. However, this conclusion does not apply to the coefficient T_h of the interfacial heat transfer. Figure 3.9a shows that the coefficient T_h depends on the edge length of the unit cell l_uc that characterizes the microscopic length scale. As l_uc increases, the coefficient T_h decreases in a non-linear fashion which can be described with good approximation by the quadratic expression

$$\frac{T_\mathrm{h} l_\beta^2}{k_\beta} = \frac{a}{\left(l_\mathrm{uc}/l_\beta\right)^2} \tag{3.75}$$

between T_h and l_uc. The quadratic relation was also reported in Table 1 of Quintard and Whitaker [1]. Our simulation results can be fit by Eq. (3.75) with the same coefficient ($a = 25.8$) reported by Quintard and Whitaker [1] if the same parameters (volume fraction and conductivity of each phase) are used in our simulations. These results further indicate that our numerical framework can properly account for linear conduction effects in a two-phase medium.

Fig. 3.9b shows the effect of the microscopic length scale on the evolution of the interfacial heat transfer in the first example of Section 3.5.1. The smaller the unit cell, the faster the interfacial heat transfer increases with time in the transient stage and the earlier it begins to level off. The microscopic length scale however does not affect the magnitude of the normalized interfacial heat transfer in the plateau stage, which is determined by the volume

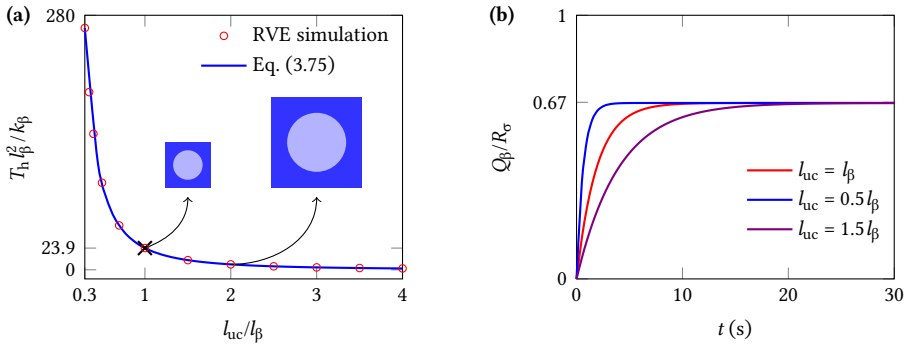

Fig. 3.9. Effect of unit cell size: (a) interfacial heat transfer coefficient T_h decreases quadratically with the unit cell edge length l_{uc}; (b) increase of the interfacial heat transfer with time at three different unit cell sizes. The values of l_β, k_β, and R_σ can be found in the first example of Section 3.5.1.

fraction. Since a smaller unit cell corresponds to a greater value of the coefficient T_h (Eq. (3.75)), the temperature difference will be smaller according to Eq. (3.74), in view of the same interfacial heat transfer in the plateau stage. Eventually, with increasingly smaller unit cells, the temperature difference will be as small as to the extent that the local equilibrium assumption holds [19]. The microscale FE simulation can thus provide quantitative guidelines for the determination of the microscopic length scale at which the one-equation model can be used with confidence (i.e., by accepting a controllable error) in place of the two-equation model.

The unit cell size is not to be confused with the RVE size. The unit cell size characterizes the microscopic length scale and thus is determined by the material, while the RVE is associated with the FE^2 method and its size is determined so that the RVE is as large as to be representative but also as small as to satisfy the rule of scale separation. The difference between a larger unit cell and a larger RVE can be seen in Figs. 3.9a and 3.10. Unlike unit cells, larger RVEs however do not affect the results for the two-phase medium used in this study: as shown in Fig. 3.10, the interfacial heat transfer coefficient T_h remains unchanged with the RVE size l_{rve}. Our numerical results also indicate that the tangent matrices $\mathbf{S}_\beta$ and $\mathbf{S}_\sigma$ of the homogenized flux (effective conductivities) do not change with the RVE size. Therefore, a single unit cell can be safely used as the RVE in our studies.

3.6 Concluding remarks

For transient heat conduction in a two-phase medium, this study presents a FE^2 two-scale framework that can properly address the development of different temperature fields in each phase thanks to the use of a two-equation model. The approach has been demonstrated in

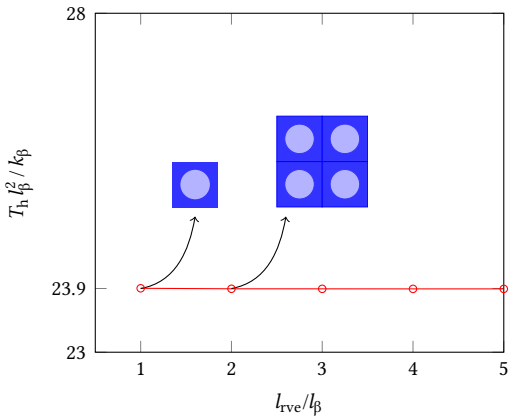

Fig. 3.10. Effect of RVE size: the interfacial heat transfer coefficient T_h in Eq. (3.74) remains constant for different RVE sizes l_{rve}.

simple academic problems with the intention of showing its potential in addressing general problems.

The macroscale equations are pragmatically derived from the single-scale governing equations by means of the volume-averaging method. The approach does not explicitly require the definition of constitutive relations or the employment of other conditions (such as the interfacial heat transfer condition (3.74)) at the macroscale. The macroscale heat fluxes and interfacial heat transfer, as well as their dependence on macroscale field variables, are numerically calculated from the microscale problem defined on an RVE. The microscale problem enables the use of general constitutive relations (e.g., temperature dependent conductivity) leading to the solution of general nonlinear transport problems with temperature-dependent heat transfer coefficients.

The two-equation model treats the two phases separately at both scales and, at variance with numerical approaches making use of the one-equation model, explicitly considers the interfacial heat transfer, thus being suited to address general local thermal non-equilibrium conditions. The heat transfer coefficient, expressing the macroscale temperature dependence of the interfacial heat transfer in the linear case, is found to depend on the microscopic length scale, which is a unique and new feature of the proposed FE^2 method.

3.A Volume average operator

With reference to a quantity x_α (a scalar or vector) in the α phase, we define the volume average operator with respect to the whole RVE as

$$\langle x_\alpha \rangle = \frac{1}{V} \int_{V_\alpha} x_\alpha \, \mathrm{d}V \tag{3.76}$$

and the intrinsic volume average [9] over the α phase as

$$\bar{x}_\alpha = \frac{1}{V_\alpha} \int_{V_\alpha} x_\alpha \, \mathrm{d}V, \tag{3.77}$$

where V denotes the total volume of the two-phase medium, and V_α is the volume of the α phase. The variable α represents either β or σ. If the volume fraction of the α phase is defined as

$$\epsilon_\alpha = \frac{V_\alpha}{V},$$

the following relation between the two volume averages holds:

$$\langle x_\alpha \rangle = \epsilon_\alpha \bar{x}_\alpha. \tag{3.78}$$

3.B Microscale problem boundary conditions

1. Periodic boundary conditions

   As shown in Fig. 3.1b, we group the external boundaries into the master boundary (mb) and slave boundary (sb). The enforcement of the periodic boundary conditions requires a one-to-one correspondence between master and slave boundaries of each phase in terms of mesh nodes. The constraint in Eq. (3.21) is then applied to each pair of nodes, one node on the master boundary and the other on the slave boundary, excluding the four corner nodes. The total number of node pairs is denoted by N_{pb}. For each pair of nodes, we assign a Lagrange multiplier λ_l to the constraint between them, with the Lagrange constraint equation expressed as

   $$u_\alpha^l\Big|_{\mathrm{mb}} - u_\alpha^l\Big|_{\mathrm{sb}} - \boldsymbol{\nabla} U_\alpha \cdot \left(\mathbf{x}_{\mathrm{mb}}^l - \mathbf{x}_{\mathrm{sb}}^l\right) = 0, \tag{3.79}$$

   where l ranges from 1 to N_{pb}, and α refers to either β or σ depending on the phase to which the node pair l belongs.

For the four corner nodes, the three Lagrange constraint equations are

$$\begin{aligned} u_\alpha^{(2)} - u_\alpha^{(1)} - \boldsymbol{\nabla} U_\alpha \cdot \left(\mathbf{x}^{(2)} - \mathbf{x}^{(1)}\right) = 0, \\ u_\alpha^{(3)} - u_\alpha^{(1)} - \boldsymbol{\nabla} U_\alpha \cdot \left(\mathbf{x}^{(3)} - \mathbf{x}^{(1)}\right) = 0, \\ u_\alpha^{(4)} - u_\alpha^{(1)} - \boldsymbol{\nabla} U_\alpha \cdot \left(\mathbf{x}^{(4)} - \mathbf{x}^{(1)}\right) = 0, \end{aligned} \tag{3.80}$$

where α takes the phase (either β or σ) containing the corner nodes.

2. Interfacial boundary conditions

   If there are N_{if} pairs of interface nodes, there exist N_{if} Lagrange constraint equations

$$u_\beta^l - u_\sigma^l = 0, \tag{3.81}$$

   where l ranges from 1 to N_{if}, u_β^l denotes the nodal temperature at the interface $\Gamma_{\beta\sigma}$, and u_σ^l is the temperature of the corresponding node on $\Gamma_{\sigma\beta}$.

3. Conservation of the stored heat between the macro- and micro-scales

   This condition is expressed by means of two Lagrange constraint equations from Eq. (3.23):

$$\begin{aligned} \int_{V_\beta} \mathbf{N}\, \mathrm{d}V\, \mathbf{u}_\beta - V_\beta\, U_\beta = 0, \\ \int_{V_\sigma} \mathbf{N}\, \mathrm{d}V\, \mathbf{u}_\sigma - V_\sigma\, U_\sigma = 0. \end{aligned} \tag{3.82}$$

In total, the number of Lagrange multipliers is

$$N_\lambda = N_{\text{pb}} + N_{\text{if}} + 5, \tag{3.83}$$

i.e., the sum of Lagrange multipliers from Eqs. (3.79) to (3.82).

References

[1] M. Quintard and S. Whitaker, *One- and two-equation models for transient diffusion processes in two-phase systems,* Advances in Heat Transfer **23**, 37 (1993).

[2] M. Quintard, M. Kaviany, and S. Whitaker, *Two-medium treatment of heat transfer in porous media: Numerical results for effective properties,* Advances in Water Resources **20**, 77 (1997).

[3] F. Kuwahara, M. Shirota, and A. Nakayama, *A numerical study of interfacial convective heat transfer coefficient in two-energy equation model for convection in porous media,* International Journal of Heat and Mass Transfer **44**, 1153 (2001).

[4] D. A. Nield and A. Bejan, *Convection in Porous Media* (Springer New York, 2013).

[5] F. Golfier, B. D. Wood, L. Orgogozo, M. Quintard, and M. Buès, *Biofilms in porous media: Development of macroscopic transport equations via volume averaging with closure for local mass equilibrium conditions,* Advances in Water Resources **32**, 463 (2009).

[6] L. Orgogozo, F. Golfier, M. Buès, and M. Quintard, *Upscaling of transport processes in porous media with biofilms in non-equilibrium conditions,* Advances in Water Resources **33**, 585 (2010).

[7] F. E. Teruel and L. Díaz, *Calculation of the interfacial heat transfer coefficient in porous media employing numerical simulations,* International Journal of Heat and Mass Transfer **60**, 406 (2013).

[8] A. Gandomkar and K. Gray, *Local thermal non-equilibrium in porous media with heat conduction,* International Journal of Heat and Mass Transfer **124**, 1212 (2018).

[9] S. Whitaker, *The Method of Volume Averaging* (Springer Netherlands, 1999).

[10] W. Shyy, S. S. Thakur, H. Ouyang, J. Liu, and E. Blosch, *Computational Techniques for Complex Transport Phenomena* (Cambridge University Press, 1997).

[11] B. D. Wood, *Technical note: Revisiting the geometric theorems for volume averaging,* Advances in Water Resources **62**, 340 (2013).

[12] M. Kaviany, *Principles of Heat Transfer in Porous Media* (Springer New York, 1995).

[13] Y. Mahmoudi and N. Karimi, *Numerical investigation of heat transfer enhancement in a pipe partially filled with a porous material under local thermal non-equilibrium condition,* International Journal of Heat and Mass Transfer **68**, 161 (2014).

[14] M. Quintard and S. Whitaker, *Local thermal equilibrium for transient heat conduction: Theory and comparison with numerical experiments,* International Journal of Heat and Mass Transfer **38**, 2779 (1995).

[15] D. A. S. Rees and I. Pop, *Local thermal non-equilibrium in porous medium convection,* in *Transport Phenomena in Porous Media III* (Elsevier, 2005) pp. 147–173.

[16] A. Gupta, J. H. Seo, X. Zhang, W. Du, A. M. Sastry, and W. Shyy, *Effective transport properties of $LiMn_2O_4$ electrode via particle-scale modeling,* Journal of The Electrochemical Society **158**, A487 (2011).

[17] A. Salvadori, E. Bosco, and D. Grazioli, *A computational homogenization approach for Li-ion battery cells: Part 1 – formulation,* Journal of the Mechanics and Physics of Solids **65**, 114 (2014).

[18] B. D. Wood and F. J. Valdés-Parada, *Volume averaging: Local and nonlocal closures using a Green's function approach,* Advances in Water Resources **51**, 139 (2013).

[19] H. Davarzani, M. Marcoux, and M. Quintard, *Theoretical predictions of the effective thermodiffusion coefficients in porous media,* International Journal of Heat and Mass Transfer **53**, 1514 (2010).

[20] R. J. M. Smit, W. A. M. Brekelmans, and H. E. H. Meijer, *Prediction of the mechanical behavior of nonlinear heterogeneous systems by multi-level finite element modeling,* Computer Methods in Applied Mechanics and Engineering **155**, 181 (1998).

[21] F. Feyel and J.-L. Chaboche, *FE^2 multiscale approach for modelling the elastoviscoplastic behaviour of long fibre SiC/Ti composite materials,* Computer Methods in Applied Mechanics and Engineering **183**, 309 (2000).

[22] V. Kouznetsova, W. A. M. Brekelmans, and F. P. T. Baaijens, *An approach to micro-macro modeling of heterogeneous materials,* Computational Mechanics **27**, 37 (2001).

[23] C. Miehe, *Strain-driven homogenization of inelastic microstructures and composites based on an incremental variational formulation,* International Journal for Numerical Methods in Engineering **55**, 1285 (2002).

[24] J. Schröder, *A numerical two-scale homogenization scheme: The FE^2 method,* in *Plasticity and Beyond* (Springer Vienna, 2014) pp. 1–64.

[25] B. S. Mercer, K. K. Mandadapu, and P. Papadopoulos, *Novel formulations of microscopic boundary-value problems in continuous multiscale finite element methods,* Computer Methods in Applied Mechanics and Engineering **286**, 268 (2015).

[26] T. Qiu, Q. Wang, and C. Yang, *Upscaling multicomponent transport in porous media with a linear reversible heterogeneous reaction,* Chemical Engineering Science **171**, 100 (2017).

[27] I. Özdemir, W. A. M. Brekelmans, and M. G. D. Geers, *Computational homogenization for heat conduction in heterogeneous solids,* International Journal for Numerical Methods in Engineering **73**, 185 (2007).

[28] I. Özdemir, W. Brekelmans, and M. Geers, *FE^2 computational homogenization for the thermo-mechanical analysis of heterogeneous solids,* Computer Methods in Applied Mechanics and Engineering **198**, 602 (2008).

[29] A. Sengupta, P. Papadopoulos, and R. L. Taylor, *A multiscale finite element method for modeling fully coupled thermomechanical problems in solids,* International Journal for Numerical Methods in Engineering **91**, 1386 (2012).

[30] F. Larsson, K. Runesson, and F. Su, *Variationally consistent computational homogenization of transient heat flow,* International Journal for Numerical Methods in Engineering **81**, 1659 (2010).

[31] G. R. Ramos, T. dos Santos, and R. Rossi, *An extension of the hill-mandel principle for transient heat conduction in heterogeneous media with heat generation incorporating finite RVE thermal inertia effects,* International Journal for Numerical Methods in Engineering **111**, 553 (2017).

[32] M. Geers, V. Kouznetsova, and W. Brekelmans, *Multi-scale computational homogenization: Trends and challenges,* Journal of Computational and Applied Mathematics **234**, 2175 (2010).

[33] R. Hill, *Elastic properties of reinforced solids: Some theoretical principles,* Journal of the Mechanics and Physics of Solids **11**, 357 (1963).

[34] J. Schröder, *Derivation of the localization and homogenization conditions for electro-mechanically coupled problems,* Computational Materials Science **46**, 595 (2009).

[35] D. Perić, E. A. de Souza Neto, R. A. Feijóo, M. Partovi, and A. J. C. Molina, *On micro-to-macro transitions for multi-scale analysis of non-linear heterogeneous materials: Unified variational basis and finite element implementation,* International Journal for Numerical Methods in Engineering **87**, 149 (2010).

[36] E. de Souza Neto, P. Blanco, P. Sánchez, and R. Feijóo, *An RVE-based multiscale theory of solids with micro-scale inertia and body force effects,* Mechanics of Materials **80**, 136 (2015).

[37] K.-J. Bathe, *Finite Element Procedures* (Prentice-Hall, New Jersey, 1996).

[38] S. Fernández-Méndez and A. Huerta, *Imposing essential boundary conditions in mesh-free methods,* Computer Methods in Applied Mechanics and Engineering **193**, 1257 (2004).

4

FE^2 multiscale modeling of transport processes in porous battery separators

Abstract

Existing battery modeling works have limitations in addressing concentration-dependent transport properties and characterizing anisotropic microstructures. We propose a simple yet adequate FE^2 multiscale framework that addresses these limitations. The microscale simulation can comprehensively characterize an anisotropic microstructure using a tensor description for the effective transport properties. From the microscale solution, the homogenized fluxes and their dependence on the downscaled macroscale variables are upscaled and thus replace the macroscale constitutive relations which are otherwise assumed in the literature. The FE^2 framework is validated by comparison to the single-scale approach.

keywords: multiscale battery modeling, FE^2, computational homogenization, ionic transport, concentration-dependent transport property, effective diffusivity tensor

4.1 Introduction

Many electrochemical models for predicting battery performance are based upon assumptions that are functional to their efficient numerical solution. A common assumption is that transport properties are constant when calculating the effective transport coefficients. Moreover, the effective transport properties are usually represented by a scalar or, at best, by a tensor with null off-diagonal entries. The implication of this choice is that the role of the microstructure is not fully reflected by the effective transport properties. This paper discusses these aspects by means of a FE^2 multiscale framework endowed with nonlinear physics-based models at the microscale (pore-scale) and well-defined information exchange between the micro- and macro-scale (cell level).

The popular DFN model [1], also referred to as the pseudo two-dimensional (P2D) model, describes porous battery components as homogenized macroscopic continua using averaged mass and charge transport equations. Microstructure effect are however taken into account in an indirect manner through the use of effective transport properties defined by means of a Bruggeman expression as summarized in 4.C. Such a simplified microstructure representation, although computationally efficient, can lead to prediction discrepancies in battery responses [2]. The lack of microstructure morphology consideration also hinders battery performance improvements through microstructure manipulation.

To consider the microstructure, a straightforward method is to conduct single-scale simulations (or called direct numerical simulations) [3, 4] that fully resolve the microstructure and thus yield accurate predictions. However, the discretization of the microstructure would require a significant computational effort, especially when the pore/particle size can be two to three orders of magnitude smaller than the typical size of a battery cell [5]. The direct microstructure-resolved models are therefore deemed unsuitable in terms of being computationally economic.

A compromise between computational cost and microstructure examination can be reached by the multiscale models [2, 6] that extend the DFN model in addressing the microstructure. The multiscale models shared similar mathematic structure in the macroscale governing equations to the DFN model (4.C) but simulated the complicated microstructure for more accurate description of the effective transport properties and volume-averaged reaction current densities. The macroscale governing equations are derived from their microscale counterparts by the volume averaging method [7], and the averaging process results in the so-called “closure terms” that need special treatment to obtain for example the effective transport properties.

Some problems however arise with the multiscale models. First, the derivation of the homogenized equations relies on simplification assumptions that cannot be rigorously proven [7–9]. Specifically, the volume-averaged fluxes are empirically modeled based on

effective transport properties [2, 9], and this is because their expressions cannot be directly obtained through the first theorem of the volume averaging method [9], even for constant bulk transport properties (i.e., linear diffusion). Second, the microscale simulations for the closure terms used constant bulk transport properties and thus the calculated effective transport properties only reflect the microstructure geometry effect. The omission of the concentration dependence leads to the question of whether we can safely use the same concentration dependence function for the effective transport properties at the macroscale (Section 4.5.1). Finally, the microscale simulations are restricted to isotropic microstructures and thus have limitations in characterizing anisotropic microstructures (Section 4.5.1). Anisotropic microstructures generally lead to transport properties in the tensor format and the off-diagonal terms are not necessarily null [10]. An non-zero off-diagonal terms will cause the macroscale responses in the direction perpendicular to the field variable gradient. Most of the microstructure studies in the literature however simply ignore the anisotropy problem. More details and discussion about the nonlinear transport properties and anisotropic microstructures can be found in Section 4.5.1.

Instead of using assumptions for the macroscale physics and solving closure terms, we adopt a FE^2-based computational homogenization scheme and present a two-scale framework with simple information exchange between the macro- and micro-scale problems. The FE^2 method has been developed and successfully employed in applications ranging from mechanical equilibrium problems [11–13] to transport problems [14] and multi-physics problems [15–18]. The theoretical framework of a computational homogenization approach for battery applications has been recently developed by Salvadori et al. [5, 19]. The model accounted for the multi-physics nature of processes taking place in battery cells, including diffusion, migration, intercalation, and mechanics.

In this paper, we focus on developing a simple FE^2 framework for ionic transport through porous battery cell separators. In the separator only two constituents coexist: a liquid electrolyte filling the pores of an inert and electrochemically inactive membrane (e.g., polyolefin [20]). The absence of active materials results in significant modeling simplifications, as no lithium exchange occurs between the constituents. This allows us to capture the most fundamental phenomena and check the applicability of the FE^2 method in the battery setting.

4.2 Single-scale description

We model ionic transport processes in the electrolyte of battery separators (Fig. 4.1a) by means of conservation laws and the concentrated solution theory [1]. Although readily available in the literature [1, 21], the governing equations are presented next since they serve as the starting point for the derivation of the volume-averaged macroscale equations

in Section 4.3.1; furthermore, their finite element method (FEM) solution is employed as reference solution for the FE^2 simulation results in Section 4.5.2.

The ionic transport in the electrolyte is governed by the mass conservation of lithium ions and the electric charge balance that are expressed, respectively, as

$$\frac{\partial c_e}{\partial t} + \boldsymbol{\nabla} \cdot \mathbf{q}_e = 0 \quad \text{and} \tag{4.1a}$$

$$\boldsymbol{\nabla} \cdot \mathbf{i}_e = 0 \quad \text{in} \quad V_\beta \times [0, t_{\text{end}}], \tag{4.1b}$$

with the lithium ion flux

$$\mathbf{q}_e = -D_e \boldsymbol{\nabla} c_e + \frac{t_e}{F} \mathbf{i}_e, \tag{4.2a}$$

the current density

$$\mathbf{i}_e = -\kappa_e \boldsymbol{\nabla} \phi_e + \kappa_D \boldsymbol{\nabla} \ln c_e, \tag{4.2b}$$

and the coefficient

$$\kappa_D = \frac{2RT\kappa_e}{F}\left(1 + \frac{\partial \ln f_e}{\partial \ln c_e}\right)(1 - t_e). \tag{4.2c}$$

The coupled set of differential equations (4.1) is solved in terms of the lithium ion concentration c_e and the electric potential ϕ_e. In the above equations, the subscript "e" refers to the electrolyte (β phase), D_e and κ_e denote the bulk diffusivity and ionic conductivity, respectively, t_e is the transference number, and f_e is the mean activity coefficient. Finally, F, R, and T represent the Faraday constant, the gas constant, and the absolute temperature, respectively.

4.3 Multiscale framework

The multiscale method employed in this study is summarized in this section where the governing equations at the two scales and the corresponding information-passing procedures are reported. In the remainder of the paper, quantities at the microscale and macroscale are identified by subscripts "m" and "M", respectively.

4.3.1 Macroscale model

The macroscale governing equations are derived by volume-averaging the single-scale formulations presented in the previous section over a representative volume element (RVE). With reference to the RVE in Fig. 4.1b, the application of the average operator (4.A) to Eq. (4.1)

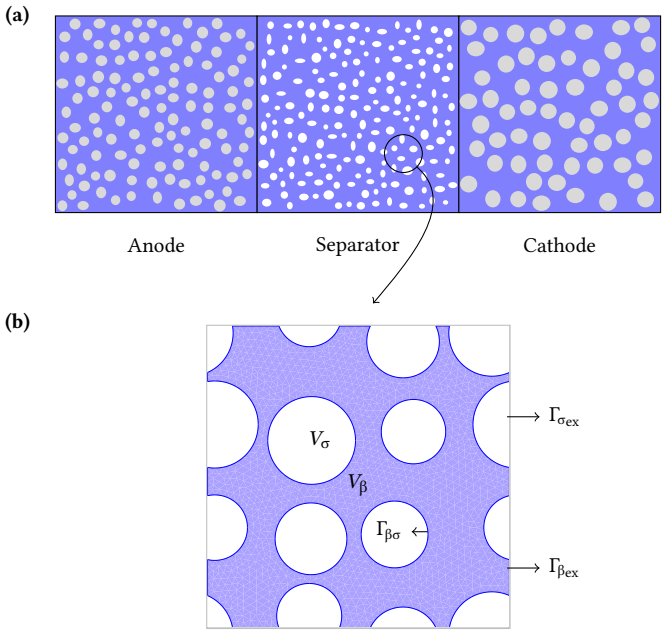

Fig. 4.1. Two-dimensional schematics of the problem domains. (a) Schematic of a battery cell with porous anode, separator, and cathode. The porous electrode and separator domains are filled with the electrolyte occupying domain V_β. (b) Microscopic representative volume element (RVE) of battery separator, consisting of blue-shaded electrolyte domain V_β and gray-shaded ion-transport blocking phase domains V_σ. The blocking phases represent the separator membrane. The RVE boundary Γ_{ex} is divided into two parts, each associated with a phase, such that $\Gamma_{ex} = \Gamma_{\beta ex} \cup \Gamma_{\sigma ex}$ with $\Gamma_{\beta ex} \cap \Gamma_{\sigma ex} = \varnothing$.

yields

$$\epsilon_\beta \frac{\partial \langle c_e \rangle_\beta}{\partial t} + \langle \nabla \cdot \mathbf{q}_e \rangle = 0 \quad \text{and} \tag{4.3a}$$

$$\langle \nabla \cdot \mathbf{i}_e \rangle = 0 \quad \text{in} \quad V_\beta \times [0, t_{\text{end}}], \tag{4.3b}$$

where ϵ_β is the electrolyte volume fraction (i.e., RVE porosity), and $\langle c_e \rangle_\beta$ represents the intrinsic volume average of the concentration, with the boundary of domain V_β defined as $\Gamma_{\beta ex} \cup \Gamma_{\beta\sigma}$ with $\Gamma_{\beta ex} \cap \Gamma_{\beta\sigma} = \varnothing$. By making use of the divergence theorem, the divergence terms in Eq. (4.3) are expanded as

$$\langle \nabla \cdot \mathbf{q}_e \rangle = \frac{1}{V} \int_{\Gamma_{\beta ex}} \mathbf{q}_e \cdot \mathbf{n}_{\beta ex} \, dA + \frac{1}{V} \int_{\Gamma_{\beta\sigma}} \mathbf{q}_e \cdot \mathbf{n}_{\beta\sigma} \, dA, \tag{4.4a}$$

$$\langle \nabla \cdot \mathbf{i}_e \rangle = \frac{1}{V} \int_{\Gamma_{\beta ex}} \mathbf{i}_e \cdot \mathbf{n}_{\beta ex} \, dA + \frac{1}{V} \int_{\Gamma_{\beta\sigma}} \mathbf{i}_e \cdot \mathbf{n}_{\beta\sigma} \, dA, \tag{4.4b}$$

where $\mathbf{n}_{\beta ex}$ is the outward-pointing unit vector normal to the β phase boundary $\Gamma_{\beta ex}$, and $\mathbf{n}_{\beta\sigma}$ is the unit vector normal to $\Gamma_{\beta\sigma}$, pointing to σ phase from β. Note that the volume average in the left-hand side is over the β phase as the ionic species and its flux only exist in the electrolyte.

At the macroscale, the separator and electrodes are viewed as homogeneous media and the microscale RVE is considered as a macroscale point [22]. The volume average of the outfluxes through the RVE boundary Γ_{ex} can therefore be thought of as obtained from the divergence of macroscale fluxes as

$$\nabla \cdot \mathbf{q}_M = \frac{1}{V} \int_{\Gamma_{ex}} \mathbf{q}_e \cdot \mathbf{n}_{ex} \, dA, \tag{4.5a}$$

$$\nabla \cdot \mathbf{i}_M = \frac{1}{V} \int_{\Gamma_{ex}} \mathbf{i}_e \cdot \mathbf{n}_{ex} \, dA. \tag{4.5b}$$

Since there is no flux in the σ phase and through its boundary $\Gamma_{\sigma ex}$, we only need to consider the flux through the boundary occupied by β phase and thus only $\Gamma_{\beta ex}$ survive in the right-hand side of Eq. (4.5). We can therefore express the first terms in the right-hand sides of Eqs. (4.4a) and (4.4b) as

$$\frac{1}{V} \int_{\Gamma_{\beta ex}} \mathbf{q}_e \cdot \mathbf{n}_{\beta ex} \, dA = \nabla \cdot \mathbf{q}_M, \tag{4.6a}$$

$$\frac{1}{V} \int_{\Gamma_{\beta ex}} \mathbf{i}_e \cdot \mathbf{n}_{\beta ex} \, dA = \nabla \cdot \mathbf{i}_M. \tag{4.6b}$$

The second terms in the right-hand sides of Eqs. (4.4a) and (4.4b) represent the flux

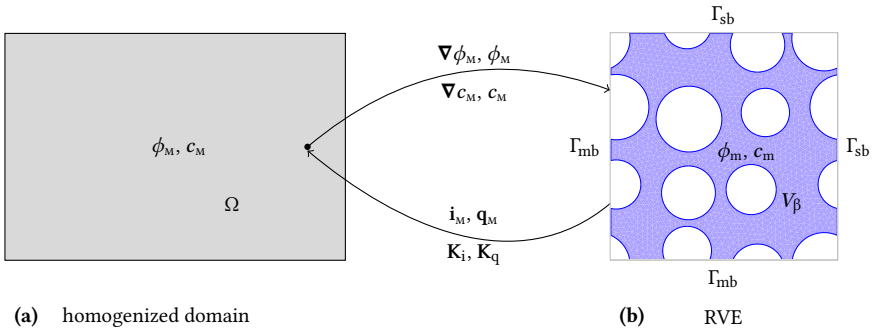

Fig. 4.2. Homogenized domain at the macroscale, RVE at the microscale, and information exchange between macro- and micro-scales. The macroscale potential (ϕ_M) and its gradient ($\nabla\phi_M$), and the concentration (c_M) and its gradient (∇c_M) at a point of the macroscale domain Ω (integration point in the context of FEM) are transferred to the microscale to define the boundary conditions, while the averaged fluxes ($\mathbf{i}_M$, $\mathbf{q}_M$) and their dependence ($\mathbf{K}_i$, $\mathbf{K}_q$) on the downscaled quantities are transferred back after the microscale quantities (ϕ_m and c_m) are solved. Panel (b) shows also the boundaries used for the enforcement of periodic boundary conditions in the FE analysis of the RVE: left and bottom edges Γ_{mb} are denoted as the master boundaries, while the right and upper edges Γ_{sb} are considered as the slave boundaries.

between the two phases. Here we restrict our scope to the ionic transport through the battery separator where there is no mutual interfacial flux between the electrolyte (β phase) and the porous membrane (σ phase). Consequently, by further considering Eqs. (4.4) and (4.6), we reformulate Eq. (4.3) as

$$\epsilon_\beta \frac{\partial c_M}{\partial t} + \nabla \cdot \mathbf{q}_M = 0 \quad \text{and} \tag{4.7a}$$

$$\nabla \cdot \mathbf{i}_M = 0 \quad \text{in} \quad \Omega \times [0, t_{end}], \tag{4.7b}$$

where $c_M = \langle c_e \rangle_\beta$ represents the intrinsic concentration in the electrolyte. Equation (4.7) expresses the macroscale governing equations over the homogenized domain Ω (Fig. 4.2a). It is remarked that c_M and ϕ_M (not explicitly present in Eq. (4.7b)) are the two field variables to solve for, and that the macroscale constitutive relations for $\mathbf{q}_M$ and $\mathbf{i}_M$ are not known yet and will be numerically obtained through the information exchange between the two scales. As schematically depicted in Fig. 4.2, the macroscale solution c_M and ϕ_M and their gradients at an integration point are downscaled to define the microscale problem; the macroscale fluxes and their tangents are then computed from the microscale solution and upscaled.

4.3.2 Downscaling

The boundary conditions enforced at the microscale level are obtained by downscaling macroscale quantities at each integration point of the macroscale mesh: concentration c_M,

potential ϕ_{M}, and their gradients $\boldsymbol{\nabla} c_{\text{M}}$ and $\boldsymbol{\nabla}\phi_{\text{M}}$, respectively. For conciseness, these quantities are stacked in the column vector

$$\mathbf{X} = \left[(\boldsymbol{\nabla} c_{\text{M}})^{\text{T}} \quad c_{\text{M}} \quad (\boldsymbol{\nabla}\phi_{\text{M}})^{\text{T}} \quad \phi_{\text{M}} \right]^{\text{T}}. \tag{4.8}$$

4.3.3 Microscale model

The microscale problem is defined on a RVE (Fig. 4.2b) associated to a macroscale integration point. The governing equations at the microscale are in principle the same as those used in the single-scale description (Eq. (4.1)), except for the assumption regarding the steady-state approximation due to the small RVE size (leading to the neglected time variation of the concentration field) and the use of subscript "m" instead of subscript "e" for the microscale quantities.

The microscale governing equations are expressed as

$$\boldsymbol{\nabla} \cdot \mathbf{q}_{\text{m}} = \boldsymbol{\nabla} \cdot (-D_{\text{e}}\, \boldsymbol{\nabla} c_{\text{m}}) = 0 \quad \text{and} \tag{4.9a}$$

$$\boldsymbol{\nabla} \cdot \mathbf{i}_{\text{m}} = \boldsymbol{\nabla} \cdot (-\kappa_{\text{e}}\, \boldsymbol{\nabla}\phi_{\text{m}} + \kappa_{\text{D}}\, \boldsymbol{\nabla} \ln c_{\text{m}}) = 0 \quad \text{in} \quad V_{\beta}. \tag{4.9b}$$

Equation (4.9a) is obtained by substituting Eq. (4.2a) into the steady state equivalent of Eq. (4.1a), taking into account that the current density is divergence free (Eq. (4.1b)) and the transference number t_{e} is taken as a constant.

Next, we derive the microscale boundary conditions from the macroscale quantities $\mathbf{X}$ in Eq. (4.8). Without loss of generality, the microscale fields can be decomposed into linear contributions consistent with macroscale quantities (c_{M}, ϕ_{M}, and their gradients) and the fluctuation fields $\tilde{c}_{\text{m}}$ and $\tilde{\phi}_{\text{m}}$ as

$$c_{\text{m}} = c_{\text{M}} + \boldsymbol{\nabla} c_{\text{M}} \cdot (\mathbf{x} - \mathbf{x}_{\text{r}}) + \tilde{c}_{\text{m}}, \tag{4.10a}$$

$$\phi_{\text{m}} = \phi_{\text{M}} + \boldsymbol{\nabla}\phi_{\text{M}} \cdot (\mathbf{x} - \mathbf{x}_{\text{r}}) + \tilde{\phi}_{\text{m}}, \tag{4.10b}$$

where $\mathbf{x}$ represents the spatial coordinate at the microscale and $\mathbf{x}_{\text{r}}$ denotes the coordinates of a reference point in the RVE domain.

To design the boundary conditions of the microscale problem, we assume that the volume average of the gradients of microscale variables over the whole RVE is equal to the corresponding macroscale gradients in analogy with the kinematical averaging relation used

in solid mechanics to establish the macro-to-micro coupling:

$$\frac{1}{V}\int_V \boldsymbol{\nabla} c_{\mathrm{m}}\,\mathrm{d}V = \boldsymbol{\nabla} c_{\mathrm{M}}, \tag{4.11a}$$

$$\frac{1}{V}\int_V \boldsymbol{\nabla} \phi_{\mathrm{m}}\,\mathrm{d}V = \boldsymbol{\nabla} \phi_{\mathrm{M}}, \tag{4.11b}$$

where $V = V_\beta \cup V_\sigma$ with $V_\beta \cap V_\sigma = \varnothing$. Note that by analogy with the problem of a RVE with holes under mechanical loading [23], the domain of the σ phase needs to be included because the RVE is considered as a macroscale point as a whole. Substituting Eq. (4.10a) into the left-hand side of Eq. (4.11a) yields

$$\frac{1}{V}\int_V \boldsymbol{\nabla} c_{\mathrm{m}}\,\mathrm{d}V = \boldsymbol{\nabla} c_{\mathrm{M}} + \frac{1}{V}\int_V \boldsymbol{\nabla} \tilde{c}_{\mathrm{m}}\,\mathrm{d}V\,. \tag{4.12}$$

According to the divergence theorem, the second term in the right-hand side of Eq. (4.12) can be reformulated as

$$\frac{1}{V}\int_V \boldsymbol{\nabla} \tilde{c}_{\mathrm{m}}\,\mathrm{d}V = \frac{1}{V}\int_{\Gamma_{\mathrm{ex}}} \tilde{c}_{\mathrm{m}}\,\mathbf{n}_{\mathrm{ex}}\,\mathrm{d}A\,, \tag{4.13}$$

where Γ_{ex} is the RVE boundary (Fig. 4.1b). Comparing Eq. (4.12) with Eq. (4.11a) and considering Eq. (4.13) lead to

$$\int_{\Gamma_{\mathrm{ex}}} \tilde{c}_{\mathrm{m}}\,\mathbf{n}_{\mathrm{ex}}\,\mathrm{d}\Gamma = 0 \quad \text{and} \tag{4.14a}$$

$$\int_{\Gamma_{\mathrm{ex}}} \tilde{\phi}_{\mathrm{m}}\,\mathbf{n}_{\mathrm{ex}}\,\mathrm{d}\Gamma = 0, \tag{4.14b}$$

where the relation for ϕ_{m} has been obtained by analogy.

To satisfy Eq. (4.14), we employ periodic boundary conditions [12]:

$$\left[\tilde{c}_{\mathrm{m}}\right]_{\Gamma_{\mathrm{mb}}} = \left[\tilde{c}_{\mathrm{m}}\right]_{\Gamma_{\mathrm{sb}}}, \quad \left[\tilde{\phi}_{\mathrm{m}}\right]_{\Gamma_{\mathrm{mb}}} = \left[\tilde{\phi}_{\mathrm{m}}\right]_{\Gamma_{\mathrm{sb}}}, \tag{4.15}$$

where Γ_{mb} and Γ_{sb} refer to the master and slave boundaries, respectively, as shown in Fig. 4.2b. By substituting Eq. (4.15) into Eq. (4.10), we have

$$c_{\mathrm{m}}(\mathbf{x}_{\mathrm{mb}}) - c_{\mathrm{m}}(\mathbf{x}_{\mathrm{sb}}) - \boldsymbol{\nabla} c_{\mathrm{M}} \cdot (\mathbf{x}_{\mathrm{mb}} - \mathbf{x}_{\mathrm{sb}}) = 0, \tag{4.16a}$$

$$\phi_{\mathrm{m}}(\mathbf{x}_{\mathrm{mb}}) - \phi_{\mathrm{m}}(\mathbf{x}_{\mathrm{sb}}) - \boldsymbol{\nabla} \phi_{\mathrm{M}} \cdot (\mathbf{x}_{\mathrm{mb}} - \mathbf{x}_{\mathrm{sb}}) = 0, \tag{4.16b}$$

where $\mathbf{x}_{\mathrm{mb}}$ and $\mathbf{x}_{\mathrm{sb}}$ represent an arbitrary point on the master boundary and its counterpart on the slave boundary, respectively. In the FE simulations, only β phase is accounted for in

the computational domain; hence, the periodic boundary conditions are implemented merely on the boundary $\Gamma_{\beta_{ex}}$ of β phase.

To uniquely solve the microscale problem, we impose another condition, that is, the intrinsic volume averages of microscale variables (c and ϕ) are equal to the macroscale quantities:

$$\langle c_{\mathrm{m}} \rangle_{\beta} = c_{\mathrm{M}}, \quad \langle \phi_{\mathrm{m}} \rangle_{\beta} = \phi_{\mathrm{M}}. \tag{4.17}$$

These relations express conservation of the lithium ion mass and electric potential between macro- and micro-scales.

4.3.4 Upscaling

In this section we describe how the homogenized quantities, based on the microscale solution and needed in the macroscale computation (Fig. 4.2), are upscaled. In the continuum mechanics context it is customary to derive the micro-to-macro transition by enforcing either the energy [24] (Hill-Mandel condition) or entropy [25] consistency across scales. An extended version of the Hill-Mandel condition tailored for battery cell modeling was proposed by Salvadori et al. [5, 19], who equated "the microscopic volume average of the virtual power on the RVE and the point wise one at the macroscale" [19]. An alternative strategy is used here, we enforce

$$\frac{1}{V} \int_{V} \boldsymbol{\nabla} c_{\mathrm{m}} \cdot \mathbf{q}_{\mathrm{m}} \, \mathrm{d}V = \boldsymbol{\nabla} c_{\mathrm{M}} \cdot \mathbf{q}_{\mathrm{M}}, \tag{4.18a}$$

$$\frac{1}{V} \int_{V} \boldsymbol{\nabla} \phi_{\mathrm{m}} \cdot \mathbf{i}_{\mathrm{m}} \, \mathrm{d}V = \boldsymbol{\nabla} \phi_{\mathrm{M}} \cdot \mathbf{i}_{\mathrm{M}}. \tag{4.18b}$$

This approach presents similarities with the works of Keip, Steinmann, and Schröder [15–17] and Lee and Sundararaghavan [18]. The former focuses on the electromechanical coupling in piezoelectric and electro-active materials at multiple scales, and the authors independently considered the mechanical and electrical contributions in the scale transitions. The latter makes use of restriction (4.18a) to identify the micro-to-macro scale transitions for the mass flux in the context of diffusion-reaction-induced degradation of composites. Numerical evidence indicates that the micro-to-macro scale transitions obtained from Eq. (4.18) (given in Eq. (4.21)) are sound for the class of problems considered in this study: in Section 4.5.2 we show that the results of our FE^2 framework are in agreement with those obtained with a single-scale analysis framework.

Macroscale fluxes are obtained by following the procedure described below. By making

use of Eq. (4.9) and the divergence theorem, the left-hand side of Eq. (4.18a) is expressed as

$$\frac{1}{V}\int_V \boldsymbol{\nabla} c_\mathrm{m} \cdot \mathbf{q}_\mathrm{m}\,\mathrm{d}V = \frac{1}{V}\int_V \boldsymbol{\nabla}\cdot(c_\mathrm{m}\,\mathbf{q}_\mathrm{m})\,\mathrm{d}V = \frac{1}{V}\int_{\Gamma_\mathrm{ex}} c_\mathrm{m}\,\mathbf{q}_\mathrm{m}\cdot\mathbf{n}_\mathrm{ex}\,\mathrm{d}A\,. \tag{4.19}$$

From the periodic boundary conditions (4.15) we evaluate $\mathbf{q}_\mathrm{m}\cdot\mathbf{n}_\mathrm{ex}$ at the master boundary to be the opposite of that at the corresponding slave boundary. This is called the anti-periodic normal flux boundary conditions [26] and can also be seen from the Lagrange multiplier used in the microscale FE implementation of periodic boundary conditions (4.B). Substituting Eq. (4.10a) into Eq. (4.19) and considering the periodic boundary conditions and anti-periodic normal flux boundary conditions, we obtain

$$\frac{1}{V}\int_{\Gamma_\mathrm{ex}} c_\mathrm{m}\,\mathbf{q}_\mathrm{m}\cdot\mathbf{n}_\mathrm{ex}\,\mathrm{d}A = \boldsymbol{\nabla} c_\mathrm{M}\cdot\frac{1}{V}\int_{\Gamma_\mathrm{ex}} \mathbf{x}\,\mathbf{q}_\mathrm{m}\cdot\mathbf{n}_\mathrm{ex}\,\mathrm{d}A\,. \tag{4.20}$$

Finally, comparing Eqs. (4.18a) and (4.20) yields the macroscale lithium ion mass flux

$$\mathbf{q}_\mathrm{M} = \frac{1}{V}\int_{\Gamma_\mathrm{ex}} \mathbf{x}\,\mathbf{q}_\mathrm{m}\cdot\mathbf{n}_\mathrm{ex}\,\mathrm{d}A\,. \tag{4.21a}$$

An analogous procedure leads to the definition of the macroscale current density

$$\mathbf{i}_\mathrm{M} = \frac{1}{V}\int_{\Gamma_\mathrm{ex}} \mathbf{x}\,\mathbf{i}_\mathrm{m}\cdot\mathbf{n}_\mathrm{ex}\,\mathrm{d}A\,. \tag{4.21b}$$

Finally, the macroscale consistent tangent matrices are defined by

$$\mathbf{K}_\mathrm{q} = \frac{\delta\mathbf{q}_\mathrm{M}}{\delta\mathbf{X}} \quad \text{and} \quad \mathbf{K}_\mathrm{i} = \frac{\delta\mathbf{i}_\mathrm{M}}{\delta\mathbf{X}}. \tag{4.22}$$

4.4 Implementation of multiscale framework

In this section we formulate the numerical framework to solve the macroscale and microscale problems using the finite element method. All vectors are assumed to be column vectors.

4.4.1 The macroscale problem

Following standard finite element procedures, we first express the variational form of the macroscale governing equations (4.7) as

$$\int_\Omega \delta c_{\text{M}}\, \epsilon_\beta \frac{\partial c_{\text{M}}}{\partial t}\, \mathrm{d}V - \int_\Omega \boldsymbol{\nabla}\, \delta c_{\text{M}} \cdot \mathbf{q}_{\text{M}}\, \mathrm{d}V + \int_{\partial\Omega} \delta c_{\text{M}}\, \bar{q}_{\text{M}}\, \mathrm{d}\Gamma = 0, \tag{4.23a}$$

$$- \int_\Omega \boldsymbol{\nabla}\, \delta\phi_{\text{M}} \cdot \mathbf{i}_{\text{M}}\, \mathrm{d}V + \int_{\partial\Omega} \delta\phi_{\text{M}}\, \bar{i}_{\text{M}}\, \mathrm{d}\Gamma = 0, \tag{4.23b}$$

where δc_{M} and $\delta\phi_{\text{M}}$ are admissible variations of the two field variables, and the terms $\bar{q}_{\text{M}}$ and $\bar{i}_{\text{M}}$ are prescribed lithium ion mass flux and current density at the macroscale domain boundary $\partial\Omega$.

A standard finite element approximation is adopted for the spatial discretization of the problem. In Eq. (4.23), the macroscale fluxes $\mathbf{q}_{\text{M}}$ and $\mathbf{i}_{\text{M}}$ are obtained from the microscale computations and they depend on the downscaled macroscale quantities $\mathbf{X}$ that include both c_{M} and ϕ_{M}. Given the coupled nature of the problem, the two macroscale equations are solved simultaneously. Each node in the spatial discretization is therefore equipped with two degrees of freedom: one representing the concentration c_{M} and the other the potential ϕ_{M}.

The continuous lithium ion mass concentration field $c_{\text{M}}(\mathbf{x})$ and electric potential field $\phi_{\text{M}}(\mathbf{x})$ are discretized into nodal values collected in the vectors $\mathbf{c}_{\text{M}}$ and $\boldsymbol{\phi}_{\text{M}}$, respectively. The two field variables at an arbitrary point $\mathbf{x}$ are approximated by means of the interpolations

$$c_{\text{M}}(\mathbf{x}) = \mathbf{N}(\mathbf{x})\, \mathbf{c}_{\text{M}} \quad \text{and} \quad \phi_{\text{M}}(\mathbf{x}) = \mathbf{N}(\mathbf{x})\, \boldsymbol{\phi}_{\text{M}}, \tag{4.24}$$

where

$$\mathbf{N} = \begin{bmatrix} N_1(\mathbf{x}) & N_2(\mathbf{x}) & \cdots & N_{n_{\text{m}}}(\mathbf{x}) \end{bmatrix} \tag{4.25}$$

collects the shape functions of all the n_{m} nodes of the discretized macroscale domain. The variations of the field variables are then expressed as

$$\delta c_{\text{M}}(\mathbf{x}) = \mathbf{N}(\mathbf{x})\, \delta\mathbf{c}_{\text{M}} \quad \text{and} \quad \delta\phi_{\text{M}}(\mathbf{x}) = \mathbf{N}(\mathbf{x})\, \delta\boldsymbol{\phi}_{\text{M}}. \tag{4.26}$$

Substituting Eqs. (4.24) and (4.26) into Eq. (4.23), we rewrite the weak statement in matrix notation as

$$\mathbf{F}_{\text{c}} = \int_\Omega \epsilon_\beta \mathbf{N}^{\text{T}} \mathbf{N} \frac{\Delta \mathbf{c}_{\text{M}}}{\Delta t}\, \mathrm{d}V - \int_\Omega \mathbf{B}^{\text{T}} \mathbf{q}_{\text{M}}\, \mathrm{d}V + \int_{\partial\Omega} \bar{q}_{\text{M}} \mathbf{N}^{\text{T}}\, \mathrm{d}\Gamma = \mathbf{0}, \tag{4.27a}$$

$$\mathbf{F}_{\phi} = - \int_\Omega \mathbf{B}^{\text{T}} \mathbf{i}_{\text{M}}\, \mathrm{d}V + \int_{\partial\Omega} \bar{i}_{\text{M}} \mathbf{N}^{\text{T}}\, \mathrm{d}\Gamma = \mathbf{0}, \tag{4.27b}$$

where

$$\mathbf{B} = \nabla \mathbf{N} = \begin{bmatrix} \dfrac{\partial N_1}{\partial x} & \dfrac{\partial N_2}{\partial x} & \cdots & \dfrac{\partial N_{n_\mathrm{m}}}{\partial x} \\ \dfrac{\partial N_1}{\partial y} & \dfrac{\partial N_2}{\partial y} & \cdots & \dfrac{\partial N_{n_\mathrm{m}}}{\partial y} \end{bmatrix} \tag{4.28}$$

denotes the gradient matrix of shape functions. The backward Euler method is used for the approximation of the time derivative term: the concentration increment $\Delta \mathbf{c}_{\text{M}}$ in Eq. (4.27) is defined as the difference between the most updated (current time increment, previous iteration) and the last converged (previous time increment) solutions obtained with an incremental-iterative procedure, and Δt quantifies the time increment size. The macroscale fluxes $\mathbf{q}_{\text{M}}$ and $\mathbf{i}_{\text{M}}$ in Eq. (4.27) are referred to the current time increment and previous iteration. They are directly upscaled from the microscale problem solution at each integration point as elaborated in Section 4.4.3.

The two sets of discrete equations (4.27a) and (4.27b) and the two field variables are collected in

$$\mathbf{F} = \begin{bmatrix} \mathbf{F}_\mathrm{c} \\ \mathbf{F}_\phi \end{bmatrix} \quad \text{and} \quad \mathbf{U} = \begin{bmatrix} \mathbf{c}_{\text{M}} \\ \boldsymbol{\phi}_{\text{M}} \end{bmatrix},$$

respectively. The system of discrete equations

$$\mathbf{F}(\mathbf{U}_n) = \mathbf{0}$$

at time $t = t_n$ (time step n) is solved by the Newton-Raphson iterative scheme. At iteration step k, the system of linearized equations reads

$$\mathbf{K}\left(\mathbf{U}_n^{k+1} - \mathbf{U}_n^k\right) + \mathbf{F}\left(\mathbf{U}_n^k\right) = \mathbf{0}, \tag{4.29}$$

with the global tangent stiffness matrix

$$\mathbf{K} = \left[\frac{\partial \mathbf{F}}{\partial \mathbf{U}_n}\right]_k = \begin{bmatrix} \mathbf{K}_{\mathrm{cc}} & \mathbf{K}_{\mathrm{c}\phi} \\ \mathbf{K}_{\phi\mathrm{c}} & \mathbf{K}_{\phi\phi} \end{bmatrix}_k . \tag{4.30}$$

The four components of the global tangent stiffness matrix $\mathbf{K}$ are defined by

$$\mathbf{K}_{cc} = \frac{\partial \mathbf{F}_c}{\partial \mathbf{c}_M} = \int_\Omega \frac{\epsilon_\beta}{\Delta t} \mathbf{N}^T \mathbf{N} \, dV - \int_\Omega \mathbf{B}^T \frac{\partial \mathbf{q}_M}{\partial \mathbf{c}_M} \, dV \,, \tag{4.31a}$$

$$\mathbf{K}_{c\phi} = \frac{\partial \mathbf{F}_c}{\partial \boldsymbol{\phi}_M} = - \int_\Omega \mathbf{B}^T \frac{\partial \mathbf{q}_M}{\partial \boldsymbol{\phi}_M} \, dV \,, \tag{4.31b}$$

$$\mathbf{K}_{\phi c} = \frac{\partial \mathbf{F}_\phi}{\partial \mathbf{c}_M} = - \int_\Omega \mathbf{B}^T \frac{\partial \mathbf{i}_M}{\partial \mathbf{c}_M}, \tag{4.31c}$$

$$\mathbf{K}_{\phi\phi} = \frac{\partial \mathbf{F}_\phi}{\partial \boldsymbol{\phi}_M} = - \int_\Omega \mathbf{B}^T \frac{\partial \mathbf{i}_M}{\partial \boldsymbol{\phi}_M} \, dV \,. \tag{4.31d}$$

Recasting the vector $\mathbf{X}$ defined in Eq. (4.8) in its discrete form as

$$\mathbf{X} = \begin{bmatrix} \mathbf{B}\mathbf{c}_M \\ \mathbf{N}\mathbf{c}_M \\ \mathbf{B}\boldsymbol{\phi}_M \\ \mathbf{N}\boldsymbol{\phi}_M \end{bmatrix} \tag{4.32}$$

and defining

$$\mathbf{S}_c = \frac{\partial \mathbf{X}}{\partial \mathbf{c}_M} = \begin{bmatrix} \mathbf{B} \\ \mathbf{N} \\ \mathbf{0} \\ \mathbf{0} \end{bmatrix} \quad \text{and} \quad \mathbf{S}_\phi = \frac{\partial \mathbf{X}}{\partial \boldsymbol{\phi}_M} = \begin{bmatrix} \mathbf{0} \\ \mathbf{0} \\ \mathbf{B} \\ \mathbf{N} \end{bmatrix} \tag{4.33}$$

yield the quantities

$$\begin{aligned} \frac{\partial \mathbf{q}_M}{\partial \mathbf{c}_M} &= \mathbf{K}_q \mathbf{S}_c, \quad \frac{\partial \mathbf{q}_M}{\partial \boldsymbol{\phi}_M} = \mathbf{K}_q \mathbf{S}_\phi, \\ \frac{\partial \mathbf{i}_M}{\partial \mathbf{c}_M} &= \mathbf{K}_i \mathbf{S}_c, \quad \frac{\partial \mathbf{i}_M}{\partial \boldsymbol{\phi}_M} = \mathbf{K}_i \mathbf{S}_\phi. \end{aligned} \tag{4.34}$$

4.4.2 The microscale problem

The variational form of the microscale governing equations (4.9) is expressed as

$$\int_{V_\beta} \boldsymbol{\nabla} \delta c_m \cdot (D_e \, \boldsymbol{\nabla} c_m) \, dV + \int_{\Gamma_{\beta ex}} \delta c_m \left(\mathbf{q}_m \cdot \mathbf{n}_{\beta ex} \right) d\Gamma + \int_{\Gamma_{\beta\sigma}} \delta c_m \left(\mathbf{q}_m \cdot \mathbf{n}_{\beta\sigma} \right) d\Gamma = 0, \tag{4.35a}$$

$$\int_{V_\beta} \boldsymbol{\nabla} \delta \phi_m \cdot \left(\kappa_e \, \boldsymbol{\nabla} \phi_m - \kappa_D \, \frac{1}{c_m} \boldsymbol{\nabla} c_m \right) dV + \int_{\Gamma_{\beta ex}} \delta \phi_m \left(\mathbf{i}_m \cdot \mathbf{n}_{\beta ex} \right) d\Gamma + \int_{\Gamma_{\beta\sigma}} \delta \phi_m \left(\mathbf{i}_m \cdot \mathbf{n}_{\beta\sigma} \right) d\Gamma = 0, \tag{4.35b}$$

in terms of the two scalar problem fields c_m and ϕ_m. Since there is no flux through the interface between β and σ phases, the boundary terms on the interior boundary $\Gamma_{\beta\sigma}$ are zero and can be removed. The remaining boundary terms on the exterior boundary $\Gamma_{\beta\mathrm{ex}}$ do not represent any prescribed Neumann boundary conditions but reflect unknown fluxes caused by the periodic boundary condition constraints (4.16). The periodic boundary condition constraints are enforced using the Lagrange multiplier method and correspondingly the flux on the boundary $\Gamma_{\beta\mathrm{ex}}$ is denoted as λ. Thus, the variational form is simplified to

$$\int_{V_\beta} \boldsymbol{\nabla}\, \delta c_\mathrm{m} \cdot (D_\mathrm{e}\, \boldsymbol{\nabla} c_\mathrm{m})\, \mathrm{d}V + \int_{\Gamma_{\beta\mathrm{ex}}} \delta c_\mathrm{m}\, \lambda_\mathrm{c}\, \mathrm{d}\Gamma = 0, \tag{4.36a}$$

$$\int_{V_\beta} \boldsymbol{\nabla}\, \delta \phi_\mathrm{m} \cdot \left(\kappa_\mathrm{e}\, \boldsymbol{\nabla} \phi_\mathrm{m} - \kappa_\mathrm{D}\, \frac{1}{c_\mathrm{m}} \boldsymbol{\nabla} c_\mathrm{m}\right) \mathrm{d}V + \int_{\Gamma_{\beta\mathrm{ex}}} \delta \phi_\mathrm{m}\, \lambda_\phi\, \mathrm{d}\Gamma = 0. \tag{4.36b}$$

The variational form is completed by the definition of appropriate statements expressing the enforcement of periodic boundary conditions:

$$\int_{\Gamma_{\beta\mathrm{ex}}} \delta\lambda\, A\, \mathrm{d}\Gamma = 0, \tag{4.37}$$

where A represents the left-hand expressions of Eq. (4.16).

The discretized system of governing equations at the microscale is obtained by replacing the discrete expression of the problem fields and their gradients in Eq. (4.36):

$$\int_{V_\beta} \mathbf{B}^\mathrm{T} D_\mathrm{e} \mathbf{B} \mathbf{c}_\mathrm{m}\, \mathrm{d}V + \int_{\Gamma_{\beta\mathrm{ex}}} \mathbf{N}^\mathrm{T} \lambda_\mathrm{c}\, \mathrm{d}\Gamma = \mathbf{0}, \tag{4.38a}$$

$$\int_{V_\beta} \mathbf{B}^\mathrm{T} \left(\kappa_\mathrm{e} \mathbf{B} \boldsymbol{\phi}_\mathrm{m} - \kappa_\mathrm{D} \frac{1}{\mathbf{N}\mathbf{c}_\mathrm{m}} \mathbf{B} \mathbf{c}_\mathrm{m}\right) \mathrm{d}V + \int_{\Gamma_{\beta\mathrm{ex}}} \mathbf{N}^\mathrm{T} \lambda_\phi\, \mathrm{d}\Gamma = \mathbf{0}, \tag{4.38b}$$

where the diffusivity D_e and the conductivity κ_e (and hence κ_D) are, in general, concentration-dependent quantities.

The discrete version of the periodic boundary condition constraints is obtained from Eq. (4.37) by means of the point collocation method [27] and expressed in 4.B via Eqs. (4.59) and (4.60). The constraint (4.17) is also discretized and expressed in Eq. (4.61). All the constraint equations are then collected and expressed in matrix form as

$$\begin{bmatrix} \mathbf{A}_\mathrm{c} & \mathbf{0} \\ \mathbf{0} & \mathbf{A}_\phi \end{bmatrix} \begin{bmatrix} \mathbf{c}_\mathrm{m} \\ \boldsymbol{\phi}_\mathrm{m} \end{bmatrix} + \begin{bmatrix} \mathbf{C}_\mathrm{c} \\ \mathbf{C}_\phi \end{bmatrix} \mathbf{X} = \mathbf{0}, \tag{4.39}$$

where $\mathbf{A}_\mathrm{c}$, $\mathbf{A}_\phi$, $\mathbf{C}_\mathrm{c}$, and $\mathbf{C}_\phi$ are constant coefficient matrices whose expressions are omitted for brevity. The Lagrange multipliers responsible for the enforcement of these constraints

are also discretized and stacked together with the vectors of nodal unknowns in the vector

$$\mathbf{u} = \begin{bmatrix} \mathbf{c}_\mathrm{m} & \boldsymbol{\phi}_\mathrm{m} & \boldsymbol{\lambda}_\mathrm{c} & \boldsymbol{\lambda}_\phi \end{bmatrix}^\mathrm{T}.$$

The system of nonlinear equations (4.38) augmented by constraint equations (4.39) is solved by means of the Newton-Raphson iteration scheme. The increment $\Delta\mathbf{u}^{k+1}$ is computed at iteration k from

$$\begin{bmatrix} \mathbf{K}_\mathrm{cc} & \mathbf{K}_{\mathrm{c}\phi} & \mathbf{A}_\mathrm{c}^\mathrm{T} & \mathbf{0} \\ \mathbf{K}_{\phi\mathrm{c}} & \mathbf{K}_{\phi\phi} & \mathbf{0} & \mathbf{A}_\phi^\mathrm{T} \\ \mathbf{A}_\mathrm{c} & \mathbf{0} & \mathbf{0} & \mathbf{0} \\ \mathbf{0} & \mathbf{A}_\phi & \mathbf{0} & \mathbf{0} \end{bmatrix} \begin{bmatrix} \Delta\mathbf{c}_\mathrm{m} \\ \Delta\boldsymbol{\phi}_\mathrm{m} \\ \Delta\boldsymbol{\lambda}_\mathrm{c} \\ \Delta\boldsymbol{\lambda}_\phi \end{bmatrix} + \begin{bmatrix} \mathbf{f}_\mathrm{c} + \mathbf{A}_\mathrm{c}^\mathrm{T}\boldsymbol{\lambda}_\mathrm{c} \\ \mathbf{f}_\phi + \mathbf{A}_\phi^\mathrm{T}\boldsymbol{\lambda}_\phi \\ \mathbf{A}_\mathrm{c}\mathbf{c}_\mathrm{m} + \mathbf{C}_\mathrm{c}\mathbf{X} \\ \mathbf{A}_\phi\boldsymbol{\phi}_\mathrm{m} + \mathbf{C}_\phi\mathbf{X} \end{bmatrix} = \mathbf{0}, \tag{4.40}$$

where we have omitted the iteration index for clarity, $\mathbf{f}_\mathrm{c}$ and $\mathbf{f}_\phi$ denote the first terms in the left-hand sides of (4.38a) and (4.38b), respectively, and the tangent matrices are defined as

$$\mathbf{K}_\mathrm{cc} = \frac{\partial \mathbf{f}_\mathrm{c}}{\partial \mathbf{c}_\mathrm{m}}, \quad \mathbf{K}_{\mathrm{c}\phi} = \frac{\partial \mathbf{f}_\mathrm{c}}{\partial \boldsymbol{\phi}_\mathrm{m}} = \mathbf{0}, \quad \mathbf{K}_{\phi\phi} = \frac{\partial \mathbf{f}_\phi}{\partial \boldsymbol{\phi}_\mathrm{m}}, \quad \mathbf{K}_{\phi\mathrm{c}} = \frac{\partial \mathbf{f}_\phi}{\partial \mathbf{c}_\mathrm{m}}. \tag{4.41}$$

4.4.3 Upscaling of macroscale quantities

This section details the numerical evaluation of homogenized fluxes ($\mathbf{q}_\mathrm{M}$ and $\mathbf{i}_\mathrm{M}$) and tangent matrices ($\mathbf{K}_\mathrm{q}$ and $\mathbf{K}_\mathrm{i}$) based on the microscale solution. In analogy with problems in mechanics, where Lagrange multipliers multiplied by the constraint coefficients represent the equivalent constraint forces, the Lagrange multipliers $\boldsymbol{\lambda}_\mathrm{c}$ and $\boldsymbol{\lambda}_\phi$, associated with the periodic boundary conditions in Eqs. (4.59) and (4.60), are related to the integrals of the lithium ion mass flux and current density, respectively, over the area of influence of each node at the external boundary. Accordingly, the homogenized fluxes are computed with reference to Eq. (4.21) as

$$\mathbf{q}_\mathrm{M} = \frac{1}{V}\int_{\Gamma_{\beta_\mathrm{ex}}} \mathbf{x}_\mathrm{m}\,\mathbf{N}^\mathrm{T}\,\lambda_\mathrm{c}\,\mathrm{d}A = \frac{1}{V}\,\mathbf{x}_\mathrm{m}\int_{\Gamma_{\beta_\mathrm{ex}}} \mathbf{N}^\mathrm{T}\lambda_\mathrm{c}\,\mathrm{d}A = \frac{1}{V}\,\mathbf{x}_\mathrm{m}\mathbf{A}_\mathrm{c}^\mathrm{T}\boldsymbol{\lambda}_\mathrm{c}, \tag{4.42a}$$

$$\mathbf{i}_\mathrm{M} = \frac{1}{V}\int_{\Gamma_{\beta_\mathrm{ex}}} \mathbf{x}_\mathrm{m}\,\mathbf{N}^\mathrm{T}\,\lambda_\phi\,\mathrm{d}A = \frac{1}{V}\,\mathbf{x}_\mathrm{m}\int_{\Gamma_{\beta_\mathrm{ex}}} \mathbf{N}^\mathrm{T}\,\lambda_\phi\,\mathrm{d}A = \frac{1}{V}\,\mathbf{x}_\mathrm{m}\mathbf{A}_\phi^\mathrm{T}\boldsymbol{\lambda}_\phi, \tag{4.42b}$$

where

$$\mathbf{x}_\mathrm{m} = \begin{bmatrix} x^{(1)} & x^{(2)} & \dots & x^{(n_\mathrm{m})} \\ y^{(1)} & y^{(2)} & \dots & y^{(n_\mathrm{m})} \end{bmatrix} \tag{4.43}$$

lists the coordinates of all the n_m nodes.

The tangent matrices are obtained as follows. At the converged state, the increment in

Eq. (4.40) is zero, and hence

$$\mathbf{f} = \begin{bmatrix} \mathbf{f}_c + \mathbf{A}_c^T \boldsymbol{\lambda}_c \\ \mathbf{f}_\phi + \mathbf{A}_\phi^T \boldsymbol{\lambda}_\phi \\ \mathbf{A}_c \mathbf{c}_m + \mathbf{C}_c \mathbf{X} \\ \mathbf{A}_\phi \boldsymbol{\phi}_m + \mathbf{C}_\phi \mathbf{X} \end{bmatrix} = \mathbf{0}. \tag{4.44}$$

We apply a small variation $\delta\mathbf{X}$ to the macroscale quantities $\mathbf{X}$ and compute the corresponding change in the microscale solution from

$$\begin{bmatrix} \mathbf{K}_{cc} & \mathbf{0} & \mathbf{A}_c^T & \mathbf{0} \\ \mathbf{K}_{\phi c} & \mathbf{K}_{\phi\phi} & \mathbf{0} & \mathbf{A}_\phi^T \\ \mathbf{A}_c & \mathbf{0} & \mathbf{0} & \mathbf{0} \\ \mathbf{0} & \mathbf{A}_\phi & \mathbf{0} & \mathbf{0} \end{bmatrix} \begin{bmatrix} \delta\mathbf{c}_m \\ \delta\boldsymbol{\phi}_m \\ \delta\boldsymbol{\lambda}_c \\ \delta\boldsymbol{\lambda}_\phi \end{bmatrix} = - \begin{bmatrix} \mathbf{0} \\ \mathbf{0} \\ \mathbf{C}_c \\ \mathbf{C}_\phi \end{bmatrix} \delta\mathbf{X}, \tag{4.45}$$

assuming that Eq. (4.44) always holds at a converged state. By rewriting Eq. (4.45) as

$$\hat{\mathbf{K}}\, \delta\mathbf{u} = \hat{\mathbf{C}}\, \delta\mathbf{X}, \tag{4.46}$$

the variations $\delta\boldsymbol{\lambda}_c$ and $\delta\boldsymbol{\lambda}_\phi$ are extracted from the converged microscale solution $\delta\mathbf{u}$ by means of gather matrices $\boldsymbol{\delta}_c$ and $\boldsymbol{\delta}_\phi$:

$$\delta\boldsymbol{\lambda}_c = \boldsymbol{\delta}_c\, \delta\mathbf{u}, \tag{4.47a}$$

$$\delta\boldsymbol{\lambda}_\phi = \boldsymbol{\delta}_\phi\, \delta\mathbf{u}. \tag{4.47b}$$

The variations of the homogenized fluxes in Eq. (4.42) are therefore expressed as

$$\delta\mathbf{q}_M = \frac{1}{V} \mathbf{x}_m \mathbf{A}_c^T\, \delta\boldsymbol{\lambda}_c = \frac{1}{V} \mathbf{x}_m \mathbf{A}_c^T \boldsymbol{\delta}_c \hat{\mathbf{K}}^{-1} \hat{\mathbf{C}}\, \delta\mathbf{X}, \tag{4.48a}$$

$$\delta\mathbf{i}_M = \frac{1}{V} \mathbf{x}_m \mathbf{A}_\phi^T\, \delta\boldsymbol{\lambda}_\phi = \frac{1}{V} \mathbf{x}_m \mathbf{A}_\phi^T \boldsymbol{\delta}_\phi \hat{\mathbf{K}}^{-1} \hat{\mathbf{C}}\, \delta\mathbf{X}, \tag{4.48b}$$

leading to the calculation of the tangent matrices

$$\mathbf{K}_q = \frac{\delta\mathbf{q}_M}{\delta\mathbf{X}} = \frac{1}{V} \mathbf{x}_m \mathbf{A}_c^T \boldsymbol{\delta}_c \hat{\mathbf{K}}^{-1} \hat{\mathbf{C}}, \tag{4.49a}$$

$$\mathbf{K}_i = \frac{\delta\mathbf{i}_M}{\delta\mathbf{X}} = \frac{1}{V} \mathbf{x}_m \mathbf{A}_\phi^T \boldsymbol{\delta}_\phi \hat{\mathbf{K}}^{-1} \hat{\mathbf{C}}. \tag{4.49b}$$

In a two-dimensional setting these matrices read as

$$\mathbf{K}_{\mathrm{q}} = \begin{bmatrix} D_{11} & D_{12} & D_{13} & D_{14} & D_{15} & D_{16} \\ D_{21} & D_{22} & D_{23} & D_{24} & D_{25} & D_{26} \end{bmatrix} \tag{4.50a}$$

and

$$\mathbf{K}_{\mathrm{i}} = \begin{bmatrix} \kappa_{11} & \kappa_{12} & \kappa_{13} & \kappa_{14} & \kappa_{15} & \kappa_{16} \\ \kappa_{21} & \kappa_{22} & \kappa_{23} & \kappa_{24} & \kappa_{25} & \kappa_{26} \end{bmatrix}. \tag{4.50b}$$

The consistent tangent matrices $\mathbf{K}_{\mathrm{q}}$ and $\mathbf{K}_{\mathrm{i}}$ express the dependence of macroscale fluxes on the macroscale field variables and their gradients. In particular, component D_{11} represents the diffusivity in the x direction while D_{22} the diffusivity in the y direction; component κ_{14} represents the ionic conductivity in the x direction and κ_{25} the conductivity in the y direction. As discussed in the next section, the other components allow to characterize properties of anisotropic microstructures. For example, component D_{12}, suggesting the dependence of the component in the first direction of $\mathbf{q}_{\mathrm{M}}$ on the component in the second direction of $\boldsymbol{\nabla} c_{\mathrm{M}}$, indicates the off-diagonal term in the effective diffusivity tensor for an anisotropic microstructure and is referred to as the rotatory diffusivity [10].

4.5 Results and discussion

As discussed in Section 4.3.1, the FE^2 framework does not require an explicit definition of effective transport properties since they are numerically obtained from the analysis at the RVE level. This aspect is discussed in the first application (Section 4.5.1) where the microscale component of the FE^2 framework is assessed. Microscale (RVE) results are compared with those obtained with the DFN model [1] for the extraction of the effective transport properties. The multiscale simulation for separators made of nanoporous materials [22] are discussed in Section 4.5.2. The FE^2 simulation results are compared with results of the single-scale simulation for the purpose of validation, and with predictions of the DFN model for illustration of the anisotropic microstructure effect. Exploiting the findings of the first application, a simplified alternative strategy to the concurrent computation for microstructure with non-evolving geometry is illustrated in Section 4.5.3. Finally, Section 4.5.4 demonstrates an application of the FE^2 framework with a time-evolving microstructure. Table 4.1 lists the notation used for the field variables in the DFN model and the FE^2 framework.

Table 4.1. Field variables and their physical meanings. At the macroscale, quantities defined in the DFN model and their counterparts in the FE^2 method are equivalent, and they are comparable to the volume averages by the single-scale approach.

Approach	symbol	physical meaning	scale
DFN	ϕ_n	homogenized electric potential	macroscale
	c_n	homogenized concentration	
FE^2	ϕ_M	electric potential at the macroscale	
	c_M	concentration at the macroscale	
	ϕ_m	electric potential at the microscale	microscale
	c_m	concentration at the microscale	
Single-scale	ϕ_e	electric potential at the pore-scale	
	c_e	concentration at the pore-scale	

4.5.1 Effective transport properties

The effective transport properties (diffusivity and ionic conductivity) are obtained from the consistent tangent matrices $\mathbf{K}_q$ (4.50a) and $\mathbf{K}_i$ (4.50b) stemming from the microscale problem. In the DFN model, the effective transport properties (4.65) are defined as the bulk properties multiplied by a factor that only takes into account the porosity. Two major concerns emerge with this approach. First, the relationship linking bulk and macroscale properties through porosity is postulated [22]. In the case of concentration-dependent bulk properties ($D_e(c_e)$ and $\kappa_e(c_e)$) [28], Eq. (4.65) implies the dependence of the effective properties (D_{eff} and κ_{eff}) on the homogenized concentration c_n (since they are used in Eq. (4.62)) instead of c_e at the pore-scale. This discrepancy stems from the phenomenological postulation of the governing equations (4.62) in the DFN model [1] and the macroscale constitutive equations (4.65) [2, 6]. The question then arises as to how well relation (4.65) estimates the actual dependence of the effective properties on the homogenized concentration c_n. Second, porosity alone does not account for microstructure morphology and its effect on the macroscopic response. Microstructures with identical porosity may yield different effective transport coefficients and thus different transport properties depending on actual geometry and transport direction (see for example Fig. 4.4 and Lagadec et al. [20]). It is therefore necessary to simulate the microstructure not only to provide accurate predictions, but also to further the understanding of how a porous microstructure affects the effective transport properties [29, 30].

Several works have addressed the second concern by means of numerical simulations on microscopic volume elements that are either numerically generated or reconstructed from

real battery microstructures. Cooper et al. [31] suggested to describe local heterogeneities in the microstructure using a vectorial tortuosity. The multiscale model in Du et al. [6] focused on the effect of the microstructure geometry on the exponent α and reported its value based on a large number of numerically-generated microstructure samples. Furthermore, image-based simulations of battery electrode [31, 32] and separator [20, 33, 34] microstructures reported different effective transport coefficients in both through-plane and in-plane directions (i.e., the direction of transport between electrodes and those directions orthogonal to it [20], respectively). In the numerical frameworks used for instance in Refs. [6, 31, 35] for determining the effective transport coefficient δ, the authors applied boundary conditions to a pair of opposite boundaries and insulated the other boundaries. These boundary conditions resulted in the transport property in one specific direction, obtaining for example D_{11} or D_{22} at a time, implicitly assuming the absence of coupling terms. While this treatment can be considered adequate for a geometrically isotropic microstructure whose effective transport coefficient can be characterized by a scalar parameter, its application to a geometrically anisotropic microstructure is inadequate.

In general, a tensorial description should be used to describe the effective diffusivity [10, 36–38] in the case of an anisotropic microstructure (and in such cases, off-diagonal terms are not necessarily zero [10]). The calculation of the effective transport coefficient δ only along orthogonal directions [20, 31–34, 36, 39] implicitly assumes that the main direction of transport between the electrodes is a principal direction and the off-diagonal terms are therefore null or, at best, negligible. This incorrect assumption and the tensorial nature of the transport properties are discussed in Section 4.5.1 while a study on the contribution of the off-diagonal terms on the overall separator response is presented in Section 4.5.2.

The previously mentioned two concerns regarding the concentration dependence and anisotropic microstructure effect can be addressed by our microscale simulations. To comprehensively characterize an anisotropic microstructure, the boundary conditions are modified as in Section 4.3.3 to enable the simultaneous calculation of transport properties in the principal directions (e.g., both D_{11} and D_{22} in a two-dimensional space) as well as the off-diagonal terms. The actual evaluation of these quantities is performed by means of the evaluation of the consistent tangent matrices in Section 4.4.3 based on the microscale solution. The proposed treatment allows the computation of transport properties in all the orthogonal directions as well as the off-diagonal terms in a coherent framework and within one microscale simulation. These quantities represent the nonlinear dependence of macroscale fluxes on the macroscale field variables. The nonlinear constitutive relation is therefore upscaled from the micro- to macro-scale, removing all the inconsistencies related to the use of simplified effective transport properties (4.65).

Unless otherwise stated, the microscale boundary conditions for the determination of

Table 4.2. Modeling parameters. Note that concentration c_e is expressed in mol/L.

Parameter	symbol	value	unit	ref.
diffusivity	D_e	$5.34 \times 10^{-10}\, e^{-0.65 c_e}$	m^2/s	[2]
ionic conductivity	κ_e	$0.0911 + 1.9101 c_e - 1.052 c_e^2 + 0.1554 c_e^3$	S/m	[2]
transference number	t_e	0.4		[40]
thermodynamic factor	$1 + \frac{\partial \ln f_e}{\partial \ln c_e}$	1		[1]
Faraday constant	F	96 485	C/mol	
gas constant	R	8.31	J/(K mol)	
absolute temperature	T	298.15	K	

the effective transport properties are defined by the downscaled macroscale quantities

$$\mathbf{X} = \begin{bmatrix} 11.2 \times 10^6\,\mathrm{mol/m^4} & 0\,\mathrm{mol/m^4} & 1000\,\mathrm{mol/m^3} & 600\,\mathrm{mV/m} & 0\,\mathrm{mV/m} & 1\,\mathrm{mV} \end{bmatrix}^{\mathrm{T}}. \tag{4.51}$$

Further, all the results involving a RVE have been obtained considering RVEs with 16 particles, corresponding to a RVE size that ensures converged transport properties (refer to the study in 4.E for the case of elliptical particles).

Concentration-dependent transport properties

This section attempts to answer the previously raised question of how accurate Eq. (4.65) represents the actual dependence of the effective diffusivity D_{eff} and ionic conductivity κ_{eff} on the homogenized concentration c_n. We consider a liquid electrolyte consisting of $LiPF_6$ dissolved in EC:DMC (a mixture of ethylene carbonate and dimethyl carbonate). Bulk transport properties, listed in Table 4.2, are chosen according to Refs. [1, 2, 40]. In the microscale FE computation, we calculate the effective transport properties at varying macroscale concentration values c_M. The chosen RVE includes 16 randomly-distributed circular particles (blocking phase) with the effective transport coefficient $\delta = 0.31$ in the x and y directions, corresponding to the value shown in Fig. 4.9. It is remarked that $\delta = 0.31$ is calculated using constant diffusivity and ionic conductivity at a porosity value of 0.5 and is thus only determined by the microstructure geometry.

Figure 4.3 shows the effective transport properties as function of the macroscale concentration (i.e., c_n in the DFN model and c_M in the proposed FE^2 approach). The effective transport properties D_{eff} and κ_{eff} denoted by dashed lines are calculated via Eq. (4.65) with $\alpha = 1.5$ (hence $\epsilon_\beta^\alpha = 0.35$) with bulk transport properties described as a function of concentration in Table 4.2. This implies that the concentration dependence does not change from the microscale to the macroscale and only a scaling factor is considered to reflect the microstructure geometry effect. The solid lines represent the effective transport properties (4.68) that

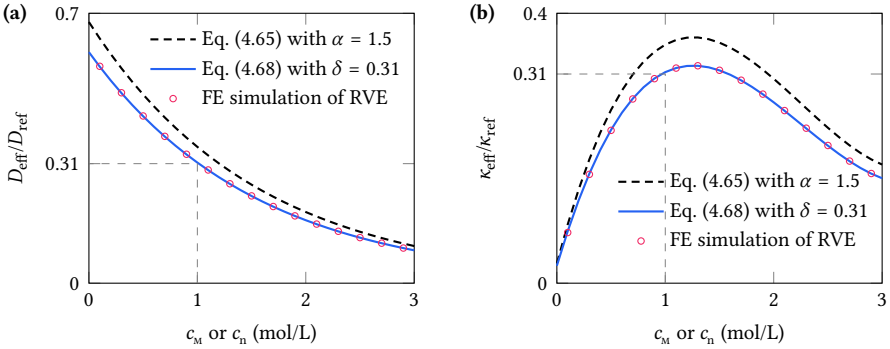

Fig. 4.3. Effective diffusivity D_{eff} (a) and ionic conductivity κ_{eff} (b) normalized by the bulk values at $c_{\text{e}} = 1.0\,\text{mol/L}$ (i.e., D_{ref} and κ_{ref}, respectively) versus the macroscale concentration c (c_{n} in the DFN model or c_{M} in the FE^2). The dashed lines are calculated via Eq. (4.65) with $\alpha = 1.5$, the solid lines represent the bulk properties multiplied by 0.31 (Fig. 4.9), while circles are calculated D_{11} and κ_{14} in Eq. (4.50) at each macroscale input c_{M}. The RVE porosity here is $\epsilon = 0.5$. The bulk properties can be found in Table 4.2.

are equal to bulk properties multiplied by the effective transport coefficient $\delta = 0.31$ (Fig. 4.9). The simulated effective transport properties denoted by circles are the component D_{11} in Eq. (4.50a) and κ_{14} in Eq. (4.50b) at discrete macroscale concentrations c_{M}. Note that these effective properties are normalized by the bulk properties at concentration $c_{\text{e}} = 1.0\,\text{mol/L}$, denoted as D_{ref} and κ_{ref}.

The microscale FE simulation results agree well with the concentration-dependent bulk properties multiplied by the effective transport coefficient $\delta = 0.31$. This agreement addresses the first concern and validates the incorporation of microstructure effect by directly scaling the concentration-dependent bulk properties by a microstructure-related factor. However, the difference between simulated results and those obtained using Eq. (4.65) with Bruggeman exponent $\alpha = 1.5$ is evident: predictions by Eq. (4.65) overestimate the effective properties. For the effective diffusivity, the difference is larger at smaller concentrations, while for the effective ionic conductivity, the difference is largest around 1.2 mol/L, where the maximum ionic conductivity is achieved. The overestimated effective properties may lead to an overestimation of the battery performance.

Anisotropic effective transport properties

This section highlights the capability of the FE^2 method in characterizing anisotropic microstructures in terms of the effective diffusivity or ionic conductivity tensor. As shown by Eq. (4.50), the tangent matrices of macroscale fluxes with respect to the macroscale field variables are general: both mass flux $\mathbf{q}_{\text{M}}$ and current density $\mathbf{i}_{\text{M}}$ include the dependence on concentration, potential, and their gradients. In particular, the macroscale diffusivity

tensor [10]

$$\mathbf{D}_{\text{eff}} = \begin{bmatrix} D_{11} & D_{12} \\ D_{21} & D_{22} \end{bmatrix} \tag{4.52}$$

extracted from $\mathbf{K}_{\text{q}}$ includes not only the transport properties in the x and y directions but also the off-diagonal components (D_{12} and D_{21}). The simultaneous presence of all the components in the effective diffusivity tensor enables the microscale FE framework to efficiently and comprehensively study the effects of an anisotropic microstructure. Anisotropy likewise applies to the effective ionic conductivity tensor $\boldsymbol{\kappa}_{\text{eff}}$, which will not be discussed for brevity.

The degree of isotropy of the effective transport properties (at the macroscale) is determined by the RVE microstructure (at the microscale). Specifically, the transport properties depend on the morphology of the ion-transport blocking phase (e.g., separator membranes [29]). For insights into the microstructure effect, we consider RVEs filled with randomly distributed elliptical particles surrounded by the electrolyte. In these RVEs, the position of an ellipse is random but the orientation is fixed at θ; the orientation θ is then changed from 0° to 90° to calculate the corresponding effective diffusivity tensor. Here we consider two different shapes represented by two aspect ratio values a/b of the semi-major to the semi-minor axes (Fig. 4.4). As the porosity can largely affect the transport properties (Fig. 4.9), it is held constant at 0.5 in this orientation/shape effect study. For each orientation we generate 100 RVE configurations for both aspect ratios taking isotropic and constant (i.e., not concentration-dependent) microscale bulk properties D_{e} and κ_{e}. We also name the tensor containing the effective transport coefficients δ_{ij}

$$\boldsymbol{\delta} = \frac{\mathbf{D}_{\text{eff}}}{D_{\text{e}}} = \begin{bmatrix} \delta_{11} & \delta_{12} \\ \delta_{21} & \delta_{22} \end{bmatrix}, \tag{4.53}$$

the 'tensor of the effective transport coefficients'.

As shown in Fig. 4.4a for $a/b = 1.5$, the effective transport coefficient δ_{11} in the x direction is maximized at $\theta = 0°$, that is, when the major axis of the ellipse is aligned along the x direction. As the major axis is progressively aligned with the y direction (θ increases), δ_{11} keeps decreasing and reaches the minimum at $\theta = 90°$. Due to the symmetry of the two directions, the effective transport coefficient δ_{22} in the y direction is a mirror of δ_{11} with respect to 45°, at which they coincide. We observe that in each simulation the values of the off-diagonal components δ_{12} and δ_{21} coincide, consistent with theoretical predictions for (uncoupled) diffusion phenomena in anisotropic media [10]. The off-diagonal components reach the peak value at $\theta = 45°$, thus showing a symmetry with respect to $\theta = 45°$; they reflect the effect of concentration gradient in the y direction on the mass flux in the x direction and vice versa, due to the anisotropic microstructure.

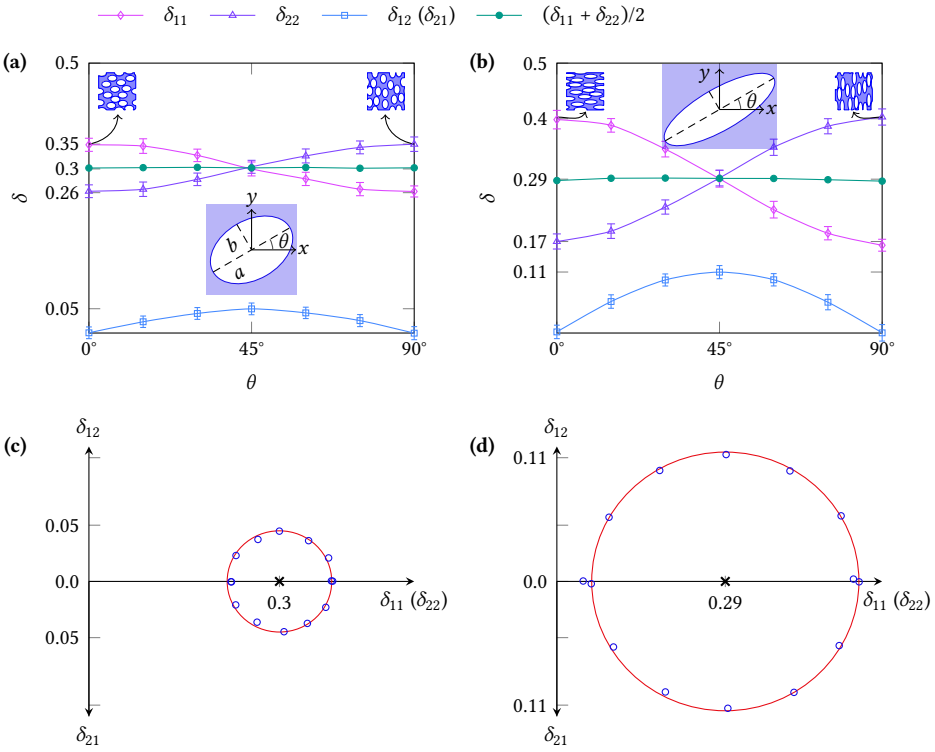

Fig. 4.4. Effective transport coefficients δ_{ij} in Eq. (4.53) versus the orientation θ of the ellipses at aspect ratio a/b = 1.5 (a) and 3.0 (b). The subscripts 1 and 2 are associated with the x and y directions, respectively. The diagonal components δ_{11} and δ_{22} are the transport coefficients in the x and y directions, respectively, while the off-diagonal components δ_{12} and δ_{21} reflect the influence of concentration gradient in the y direction on the mass flux in the x direction and vice versa. In the simulation the bulk properties (D_e and κ_e) are isotropic and constant. The porosity is held constant at 0.5, that is, the total area of ellipses is fixed. Panels (c) and (d) show the Mohr's circles related to the results in panels (a) and (b), respectively.

The variation of the three components δ_{11}, δ_{22}, and δ_{12} with θ follows the transformation equations derived from coordinate rotation [10]. The transformation equations are similar to the well-known stress transformation equations, and thus we make use of the Mohr's circle [41], typically used in solid mechanics, to interpret our numerical results. A similar approach has been recently taken in Yang and Qin [42]. The Mohr's circle is plotted for $\boldsymbol{\delta}$ and the data points (the average values in panel (a)) at different θ values are aligned along the circle. Here the center point is located on the horizontal axis at the mean value of δ_{11} and δ_{22}, which is basically constant irrespective of the θ value; the diameter of Mohr's circle is calculated as the difference of δ_{11} and δ_{22} when $\theta = 0^\circ$ or 90°. The constant mean value suggests that the transport property enhancement in one direction occurs at the expense of the property in the perpendicular direction.

The arguments just exposed also apply to the results at a higher aspect ratio ($a/b = 3.0$ in Fig. 4.4b), although with a difference. The variation of the effective transport coefficients is wider than that at $a/b = 1.5$, suggesting a stronger anisotropic effect; accordingly, the radius of the Mohr's circle is larger. The mean value of δ_{11} and δ_{22} (0.29) is also constant and quite close to that at $a/b = 1.5$ (0.30) and to the average (0.31) of δ calculated from RVEs with randomly-distributed circular particles ($a/b = 1.0$) at the same porosity (Fig. 4.9). The maximum difference (0.02) is of the same order of magnitude as the standard deviation of the reported δ values.

In Fig. 4.4, we fix the coordinate system but rotate the elliptical particles for the sake of computational convenience. This strategy is equivalent to fixing the microstructure but rotating the coordinate system. Actually, for an arbitrary fixed microstructure, by rotating the coordinate system, the effective diffusivity tensor measured can also be represented by Mohr's circle as described above. From Fig. 4.4b to a, it can be seen that the lower the aspect ratio a/b (less anisotropic), the smaller the radius of Mohr's circle. The circle will shrink to a single point when $a = b$ (isotropic microstructure). Therefore, the radius of the constructed Mohr's circle can serve to characterize the degree of microstructural anisotropy. Two conclusions follow. First, the anisotropy degree can be evaluated as the difference between the maximum and minimum principal transport properties along the principal directions (i.e., with null off-diagonal components) [42]. However, the difference between the maximum and minimum transport properties along arbitrary orthogonal directions, proposed by Cooper et al. [31] as a measure of the anisotropy, is actually not representative of the anisotropy degree. Second, since the transport direction between electrodes is in general not the principal, the off-diagonal components of the effective diffusivity tensor cannot be disregarded a priori. We show in Sections 4.5.2 and 4.5.3 that the off-diagonal components can have a significant impact on the macroscale separator response.

Thanks to the the simplified representation of the separator microstructure adopted (with ellipses-shaped inclusion to represent the blocking phase), we compare our simulation

results with those reported by Ebner et al. [32], who studied the effect of particle shape and orientation on the tortuosity of (three-dimensional) battery electrode microstructure. We first introduce the concept of tortuosity τ that quantifies the resistance to diffusion caused by the convolution of the pore network [31]. The tortuosity τ is calculated from porosity ϵ (held at 0.5) and the simulated effective transport coefficient δ through the relation $\tau = \epsilon/\delta$. Ebner et al. [32] reported the tortuosity around 1.46 for NMC electrodes consisting of spherical active particles. In LCO electrodes, the active particles are elongated along an in-plane direction and the tortuosity in the through-plane direction increases to 1.77. As the particles are further shaped into platelets in the graphite electrodes, the tortuosity in the through-plane direction grows up to 3.76. By converting δ into τ, we obtain a tortuosity equal to 1.61 for a RVE filled with random circular particles (Fig. 4.9). As the aspect ratio increases from 1.5 to 3, the tortuosity in Fig. 4.4 along the direction corresponding to the through-plane direction increases from 1.9 to 2.9. Note that in a real battery microstructure a particle's major axis is basically aligned with the current collector plane and is thus perpendicular to the through-plane direction [32]. The through-plane direction can be identified with the x direction at $\theta = 90^\circ$ in Fig. 4.4. The agreement in the trend of tortuosity change validates the simple representation of real microstructures by two-dimensional RVEs with ellipses and the anisotropic effect quantified by the proposed numerical approach. Our numerical simulation results confirm the qualitative design guidelines proposed in Ebner et al. [32] and can provide quantitative guidelines to manipulate the microstructure for better performance.

Since the results in Fig. 4.4 are obtained with bulk transport properties that are isotropic (described by a scalar) and constant (concentration independent), the off-diagonal terms in the effective diffusivity tensor stems from the microstructure anisotropy, which largely depends on the interplay between particle shape and orientation. The effect of the off-diagonal terms on macroscopic responses is further illustrated in Section 4.5.2.

4.5.2 Comparison with single-scale simulation results and DFN model prediction

The previous discussion on effective transport properties pertains to microscale simulations and is in general valid for any porous microstructure, including that of electrodes and separators. In this section we employ the multiscale approach to characterize ionic transport in the separator with an anisotropic microstructure. As a validation of the FE^2 framework, the multiscale simulation results are compared with those obtained from a single-scale simulation. This example highlights the relevance of the off-diagonal terms to the proper evaluation of the macroscopic response, and the ability of the FE^2 method to properly account for all terms of the effective transport property tensor. The predictions of the DFN model, which uses scalar effective transport properties, are also discussed.

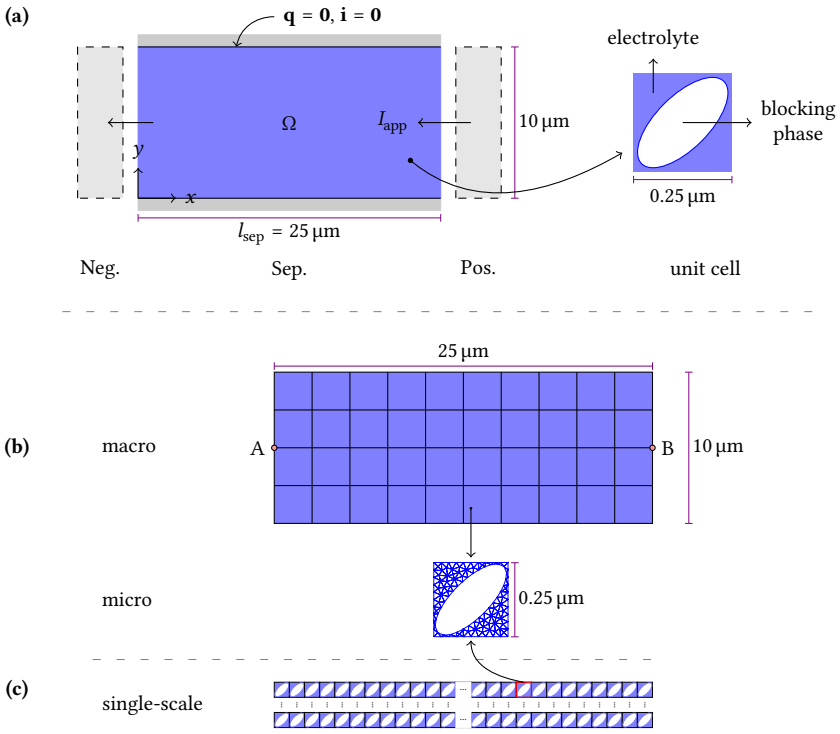

Fig. 4.5. Panel (a) illustrates the problem setting. The RVE porosity is 0.5, and the electrolyte properties are listed in Table 4.2. Panel (b) shows the computational mesh for the FE^2 method: 10×4 four-node quadrilateral elements are used for the macroscale mesh and 204 three-node triangular elements for the RVE mesh. The single-scale discretization in panel (c) consists of 100×40 unit cells, with each unit cell discretized as the RVE.

We simulate a porous separator consisting of a regular array of unit cells. Each unit cell contains an elliptical ion-transport blocking phase surrounded by the electrolyte as shown in Fig. 4.5a. Figure 4.5b shows the discretization of the multiscale problem domains at both scales. At an integration point of the macroscale mesh, we attach the microscale RVE, which is equal to a unit cell. For the single-scale simulation, we consider 100×40 unit cells as shown in Fig. 4.5c. Numerical studies (not reported here) confirm that the results obtained with each approach can be considered converged. Here we consider the concentration-dependent transport properties listed in Table 4.2.

In accordance with the galvanostatic charge process, a constant current density I_{app} and a constant lithium ion mass flux are enforced. In addition, the electric potential at the leftmost boundary $x = 0$ is set to zero as the reference value. Boundary and initial conditions are

expressed as

$$\mathbf{i}_{\text{M}} \cdot \mathbf{n}|_{x=l_{\text{sep}}} = -I_{\text{app}}, \quad \phi_{\text{M}}|_{x=0} = 0, \tag{4.54a}$$

$$\mathbf{q}_{\text{M}} \cdot \mathbf{n}|_{x=l_{\text{sep}}} = -\frac{I_{\text{app}}}{F}, \quad \mathbf{q}_{\text{M}} \cdot \mathbf{n}|_{x=0} = \frac{I_{\text{app}}}{F} \quad \text{for } t \in [0, t_{\text{end}}], \tag{4.54b}$$

and

$$c_{\text{M}} = c_0 \quad \text{at } t = 0 \text{ in } \Omega, \tag{4.54c}$$

respectively. We apply a current density $I_{\text{app}} = 300\,\text{A/m}^2$, equivalent to a 10 C charge rate for commercial graphite-NMC battery cells [20, 43]. The initial concentration c_0 in the whole separator domain Ω is specified at $1000\,\text{mol/m}^3$. The simulation ends at $t_{\text{end}} = 4\,\text{s}$ when steady-state responses are observed. The above boundary and initial conditions for the multiscale problem also hold for the single-scale problem.

The results are reported in Fig. 4.6. Panels (a) and (c) show the steady-state ionic concentration and electric potential distribution, respectively, along three horizontal lines (bottom: $y = 0\,\mu\text{m}$, middle: $y = 5\,\mu\text{m}$, and top:$y = 10\,\mu\text{m}$), while panels (b) and (d) show the concentration and potential profiles, respectively, along three vertical lines (leftmost: $x = 0\,\mu\text{m}$, middle: $y = 12.5\,\mu\text{m}$, and rightmost: $y = 25\,\mu\text{m}$). The circles represent the macroscale solution c_{M} and ϕ_{M} from the FE^2 method; the solid lines denote the single-scale simulation results, i.e., the intrinsic volume averages $\langle c \rangle_\beta$ and $\langle \phi \rangle_\beta$ of each unit cell (4.A). Initially, the concentration is uniform in the x and y directions; as the current flows, concentration gradient starts to develop, resulting in lower concentration at the leftmost edge and higher concentration at the rightmost boundary. Despite the insulated top and bottom boundaries, field variable gradients develop in the y direction to counterbalance the contribution by the off-diagonal terms (e.g., D_{12} and D_{21}) reported in Fig. 4.4.

Besides the steady-state profiles, we show the concentration evolution at the middle point of the left-hand boundary (A) and that of the right-hand boundary (B) in panel (e). Panel (f) reports the temporal evolution of the potential drop from point B to A and provides an indication of the ohmic loss attributable to the separator. The figure shows that the multiscale simulation results adequately match the single-scale simulation results, validating the multiscale framework (and the scale transitions described in Sections 4.3.3 and 4.3.4). In this example, we specifically choose the inclination $\theta = 45^\circ$ for the particles in order to maximize the off-diagonal values (in analogy with the results reported in Fig. 4.4), causing evident concentration and potential gradients in the y direction. The variation in the y direction is captured by the FE^2 method and the single-scale approach, but is not seen in the results pertaining to the DFN model, as denoted by the dashed lines in any of the panels. The difference is due to the scalar effective transport property parameter adopted in the DFN

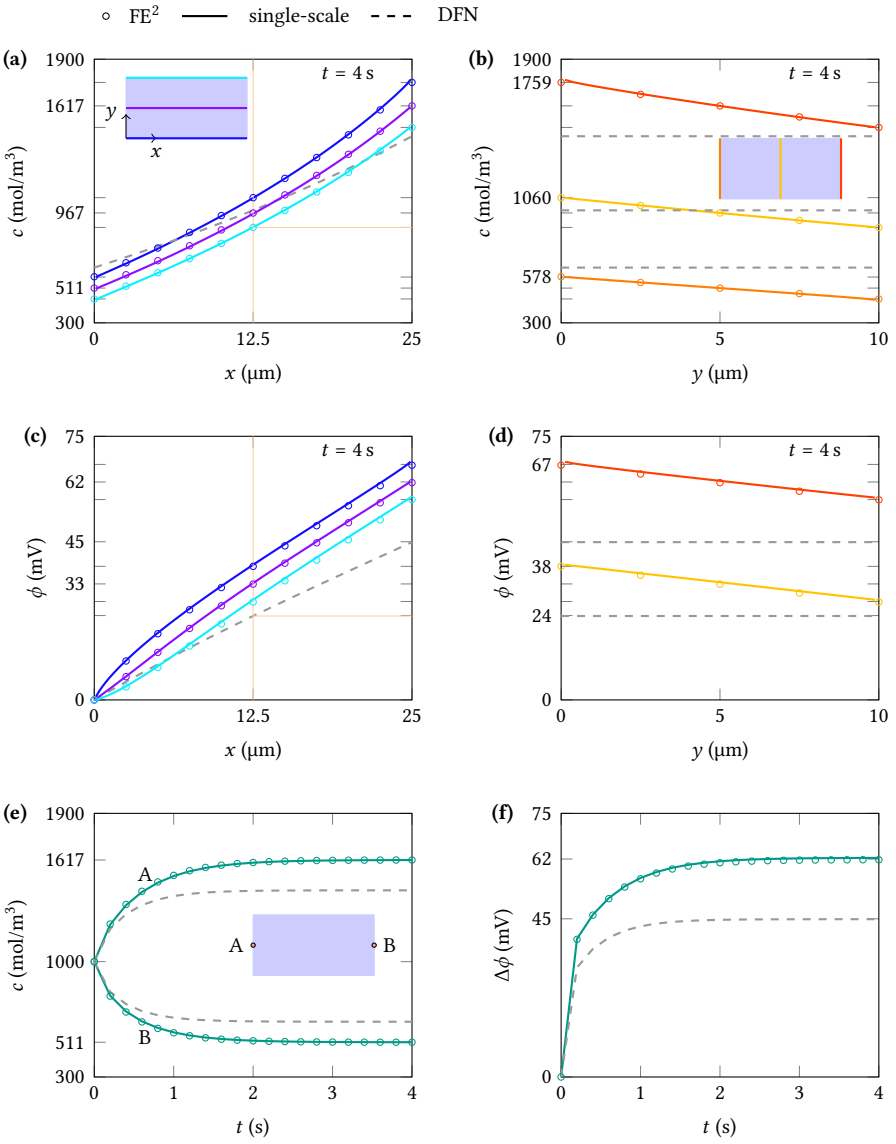

Fig. 4.6. Comparison between FE^2 calculation and single-scale simulations. Panels (a) and (c) show concentration c and potential ϕ, respectively, along the x direction at $y = 0$, 5, and 10 µm in the steady state ($t = 4$ s); correspondingly, panels (b) and (d) show concentration c and potential ϕ along the y direction at $x = 0$, 12.5, and 25 µm. Here c and ϕ refer to c_{M} and ϕ_{M} for the FE^2 method, c_{n} and ϕ_{n} for the DFN model (Table 4.1), and the intrinsic volume averages $\langle c \rangle_{\beta}$ and $\langle \phi \rangle_{\beta}$ for the single-scale simulations. Panel (e) shows the temporal evolution of the concentration at point A and B, which are located at the center of the leftmost ($x = 0$ µm) and rightmost ($x = 25$ µm) boundaries of the separator, respectively. Panel (f) shows the temporal evolution of the potential drop $\Delta\phi$ from point B to A across the separator, i.e., the potential at point B, in view of a null potential fixed at the leftmost boundary.

model. This scalar parameter is equivalent to a transport property tensor with equal diagonal terms $D_{11} = D_{22}$ and null off-diagonal terms $D_{12} = D_{21} = 0$, i.e., the identity tensor multiplied by D_{11}. Furthermore, the value of D_{11} is determined through Eq. (4.65) with $\alpha = 1.5$, which was shown to overestimate the effective transport properties (Fig. 4.3). This overestimation further amplifies the difference with the results of the multiscale and single-scale simulations in Fig. 4.6, which is up to 33% in terms of the potential drop across the separator (panels (c), (d), and (f)). The roles of the off-diagonal terms are further investigated in the following section.

4.5.3 A simplified alternative strategy to the FE^2 method

According to the discussion in Section 4.5.1 related to Fig. 4.3, the effective transport properties obtained from the concentration-dependent bulk transport properties multiplied by the effective transport coefficient δ are as accurate as the results obtained with the microscale FE simulation. For anisotropic microstructures, geometry anisotropy alone will cause anisotropic effective transport properties described in the tensor format (Fig. 4.4), even in the case of isotropic bulk transport properties. The observation in Fig. 4.3, related to an isotropic microstructure, begs the question: Considering an anisotropic microstructure, would it be possible to use the effective transport property tensors ($\mathbf{D}_{\text{eff}}$ and $\boldsymbol{\kappa}_{\text{eff}}$), obtained as the product of bulk transport properties (D_{eff} and κ_{eff}) and the tensor of the effective transport coefficients $\boldsymbol{\delta}$, in macroscale simulations, i.e., using the DFN model (4.62) in place of concurrent FE^2 simulations? This simplified alternative strategy has been used in computational solid mechanics (see, e.g., [44]) to reduce simulation costs and is in general applicable when material properties are independent of the field variables, leading to a clear identification of the effects of the microstructure geometry. In this section, we will verify if this simplified alternative strategy is applicable to anisotropic microstructures and concentration-dependent bulk transport properties. The problem setting is that of Section 4.5.2.

Figure 4.7 shows the comparison between the results by the simplified alternative strategy and those by the concurrent FE^2 method. The results by these two approaches agree well with each other, suggesting that an independent microscale computation of RVE can be conducted a priori and then used for the macroscale simulation. The agreement also suggests that the effective transport properties ($\mathbf{D}_{\text{eff}} = D_{\text{e}}(c_{\text{M}})\,\boldsymbol{\delta}$ and $\boldsymbol{\kappa}_{\text{eff}} = \kappa_{\text{e}}(c_{\text{M}})\,\boldsymbol{\delta}$) are in agreement with the effective transport properties directly obtained from the microscale FE simulations, analogous to the results reported in Fig. 4.3. Therefore, for a quick evaluation of the battery performance, we can simply assume an non-evolving microstructure and adopt the proposed simplified alternative strategy. For non-evolving microstructures, the concurrent FE^2 has no advantage over the simplified strategy, even if in the case of anisotropic microstructures. The key to the macroscale prediction is the proper characterization of the microscale RVE.

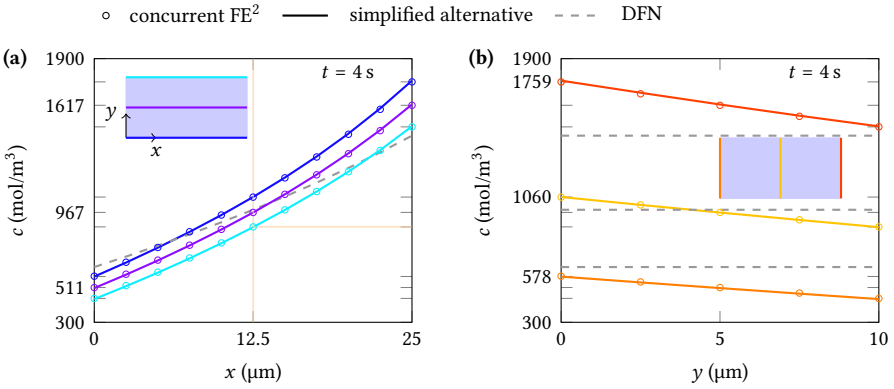

Fig. 4.7. Comparison of the results obtained with the simplified alternative strategy and the concurrent FE^2 method. The problem setting is reported in Fig. 4.5a. The results of the concurrent FE^2 and DFN model are those shown in Fig. 4.6a and b. The simplified alternative strategy results are obtained by solving Eq. (4.62) with the effective transport properties equal to the bulk properties multiplied by the tensor of the effective transport coefficients, which is calculated from the microscale FE simulation of the RVE in Fig. 4.5a.

We remark that this simplified alternative strategy differs from the multiscale models in the literature [2, 6] in terms of the tensorial description of the effective transport coefficients. The microscale simulations of these models do not consider the off-diagonal terms and only evaluate the diagonal terms (i.e., the transport properties in two/three orthogonal directions [31, 33]). Such a procedure is acceptable for anisotropic microstructures only if the considered directions coincide with the principal directions of the transport processes. The comparison between the FE^2 simulation results and the DFN model predictions in Fig. 4.7 shows that if the off-diagonal terms are ignored, an erroneous evaluation of the cell response follows despite the dominant mono-dimensional nature of the battery cell processes.

4.5.4 An example with time-evolving microstructure

The example in the previous sections 4.5.2 and 4.5.3 assumes that the microstructure does not evolve during a (dis)charge cycle. However, a (dis)charge process is always accompanied with expansion/contraction of the electrodes, leading to dynamic microstructure changes of the separator. In addition to the electrochemistry-induced deformation, external mechanical loading may also cause extra deformations [20, 45].

When the separator membrane deforms, the microstructure deformation results in concurrent porosity ϵ and tortuosity τ changes [20]. The concurrent changes of porosity and tortuosity cause reduced effective transport coefficients $\delta = \epsilon/\tau$ of the separator membrane [20], influencing the battery cell performance. Lagadec et al. [20] showed that when the separator membrane is subject to a significant deformation level (up to 40%), the effective

transport coefficient reduces by 96% in the through-plane direction of the separator layer, thus making the separator the limiting component of the cell operation at a modest C-rate of 0.75 C.

A multiscale simulation approach with concurrent macro- and micro-scale simulations could be employed to capture the effect of the evolving microstructure. As the porosity effect has been already discussed, for simplicity we only consider the microstructure morphology evolution (aspect ratio change) and hold the porosity constant at 0.5. The problem setting is that of Section 4.5.2, except for the microstructure (the RVE contains 16 ellipses with changing aspect ratios a/b (Fig. 4.8a and b)). During the whole simulation process, we use five RVEs containing elliptical particles with aspect ratio a/b ranging from 3 to 1.4 with an increment step equal to 0.4 and five corresponding RVEs with reversed aspect ratios, as well as a RVE containing circular ($a/b = 1$) particles (Fig. 4.8, red boxes). For each aspect ratio value, we generate 50 RVE samples and calculate the average transport properties; we then select a RVE with transport properties that are close to the average values.

We consider two deformation histories with coincident initial and final microstructure configurations, but different time-evolving patterns. Figure 4.8a shows pattern I: each RVE configuration is active for two consecutive time steps, except for that with $a/b = 1$ which is active for only one time step. Pattern II is shown in Fig. 4.8b: the aspect ratio a/b evolves from 3 to 1/3 in the first 11 time steps and then stays at $a/b = 1/3$ in the last 10 time steps. The total simulation time (4 s) is taken shorter than that of a charging cycle under 10 C for the sake of computational cost.

The microstructure evolution in Figs. 4.8a and b is obtained by keeping the semi-major axes of the ellipses always aligned with the x direction when $a/b > 1$ or the y direction when $a/b < 1$. According to Fig. 4.4, these two directions are the principal directions and hence the off-diagonal components (δ_{12} and δ_{21}) are null. Due to the insulated top and bottom boundaries and the absence of the off-diagonal components, concentration and potential will be uniform in the y direction, with the maximum and minimal values at the right-hand and left-hand edges, respectively. The temporal evolution of the maximum/minimum concentration and potential drop across the separator are of interest and plotted in Figs. 4.8c and d. The DFN model results (same as in Fig. 4.6e) are presented here as a reference: the maximum/minimum concentration and potential drop show a transient stage followed by a steady-state configuration. This behavior is due to the fixed porosity and hence the non-evolving transport properties with time. However, for pattern I, the maximum concentration keeps increasing, the minimum concentration keeps decreasing, and the potential drop keeps increasing. These trends are attributed to the evolving shape of the blocking phase and the consequent decreasing diffusivity in the x direction, in spite of the constant porosity. In the case of pattern II, the change of the concentration and potential drop is more drastic in the beginning and then tends to stabilize, in accordance with the quick microstructure evolution

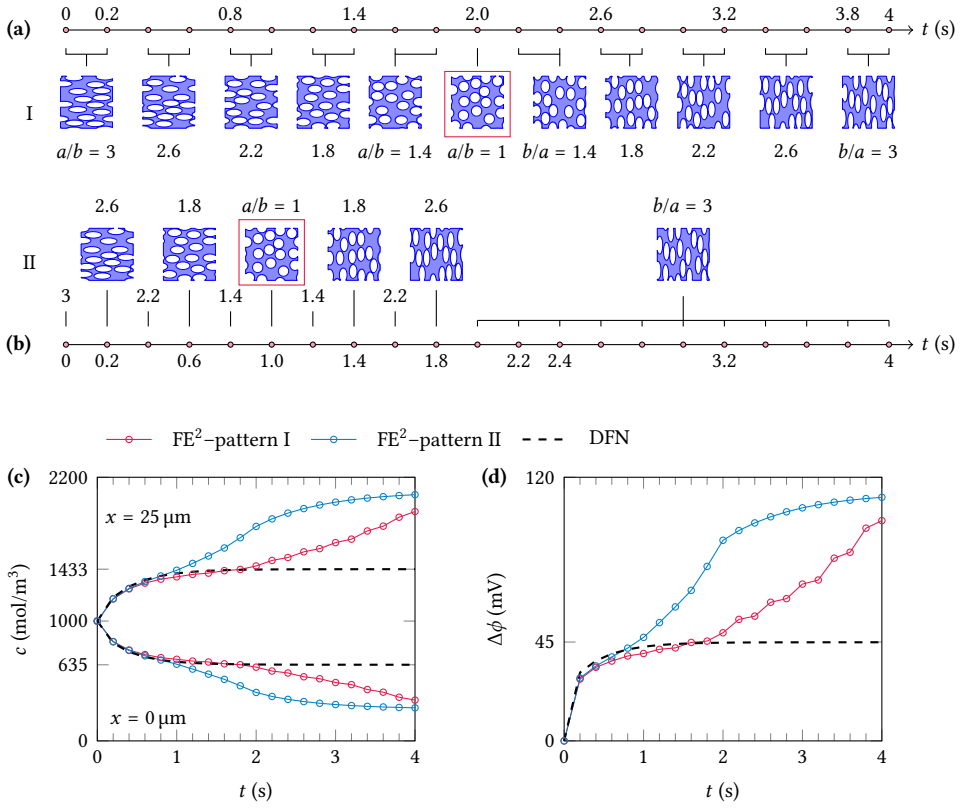

Fig. 4.8. FE^2 simulation of a separator with time-evolving microstructure. The 4 s simulation time is discretized into 21 time steps. The microstructure evolves with time following two different patterns (I in panel (a) and II in (b)) at constant porosity equal to 0.5. Panel (c) shows the temporal evolution of the maximum and minimum concentrations computed by the FE^2 method under pattern I and II and by the DFN model that only considers porosity. Panel (d) shows the potential drop across the separator. Here c and ϕ refer to c_{M} and ϕ_{M} in the FE^2 method and c_{n} and ϕ_{n} in the DFN model.

in the first 11 time steps, followed by a stabilized microstructure. A noticeable difference between the two deformation patterns lies in the energy loss due to the potential drop in Fig. 4.8b. The energy dissipated during the simulated process is proportional to the integral of the potential drop ($\Delta\phi$) with respect to time: pattern II dissipates 58.6% more energy than pattern I.

The morphology change alone leads to different macroscopic responses depending on the deformation histories (pattern I and II). If a porosity change is superimposed onto the morphology change, we envisage an even stronger modification of the macroscopic responses, indicating the need to monitor the microstructure evolution and the consequent transport property changes at adequately close time instants. The on-the-fly transport property simulations based on imaged microstructures was also encouraged by Legadec et al. [20] for improved understanding of local effects in energy storage applications. However, they also recognized that the deformation of the separator is elastic (no residual deformation upon loading removal) under low applied loadings, rendering it a challenge to image the separator microstructure at different stages of the deformation process.

4.6 Conclusions

The major difference between the proposed FE^2 framework and existing multiscale models [2, 6] lies in the microscale problem setting and simulation. The downscaled macroscale quantities enable the microscale FE simulation to return the effective transport property as a function of the macroscale field variables, especially when the bulk transport properties are concentration dependent. Figure 4.3 shows that the simulated effective transport properties are in perfect agreement with the bulk properties multiplied by a microstructure-related coefficient (i.e., the effective transport coefficient in Eq. (4.66)). This agreement suggests that the dependence of the effective transport properties on the homogenized concentration can take the same form as the concentration dependence of the bulk properties at the pore-scale and thus validates the common practice (Eq. (4.68)) employed in many models [1, 2, 6].

Anisotropy of microstructures causes anisotropic effective transport properties even when the bulk transport properties are isotropic (Fig. 4.4). The effective transport properties can be described by a scalar parameter only for an isotropic microstructure, while for an anisotropic microstructure, a tensor representation with generally non-zero off-diagonal terms is necessary [10]. The tensor description is extremely necessary and useful when the principal directions of the electrode microstructure can not be determined in advance. Unlike existing microstructure characterization studies [6, 31, 32, 35], our microscale simulation naturally characterizes any microstructure in a tensor format and calculates all terms of the effective transport property tensor. Because of such comprehensive microstructure

characterization, the microstructure effect can be quantified by the FE^2 framework and thus be exploited for better macroscale performance. Even if transport processes are predominantly unidirectional at the battery cell level (along the through-plane direction), transport processes are actually multi-directional in the microstructure of porous battery components. The FE^2 framework thus provides a valuable design tool for both porous battery separators and electrodes.

As the microscale computation is embedded in the macroscale simulation, the FE^2 framework is especially relevant in situations where the microstructure morphology evolves in time and space (Section 4.5.4). For non-evolving microstructures, the insights from the concentration-dependence and anisotropy studies demonstrate that a microscale simulation can be conducted a priori and the simplified alternative strategy (Section 4.5.3) used for cost reduction in place of the FE^2 method.

4.A Volume average operators

The volume average and intrinsic volume average operators are defined with reference to the electrolyte phase β. This phase occupies volume V_β in the RVE volume V. The volume average of quantity x in the electrolyte phase is defined as

$$\langle x \rangle = \frac{1}{V} \int_{V_\beta} x \, \mathrm{d}V, \tag{4.55}$$

and its intrinsic volume average as

$$\langle x \rangle_\beta = \frac{1}{V_\beta} \int_{V_\beta} x \, \mathrm{d}V. \tag{4.56}$$

The volume fraction of the electrolyte phase β is defined as

$$\epsilon_\beta = \frac{V_\beta}{V}. \tag{4.57}$$

By comparing (4.55) and (4.56) it follows that

$$\langle x \rangle = \epsilon_\beta \langle x \rangle_\beta . \tag{4.58}$$

4.B Discrete constraint equations for the microscale problem

The relations below are valid for a two-dimensional microscale problem.

1. Periodic boundary conditions
   As shown in Fig. 4.2b, the boundary of the RVE is partitioned into master boundary (mb) and slave boundary (sb). Periodic boundary conditions require a one-to-one correspondence between the nodes on the master boundary and those on the slave boundary of the electrolyte phase. The constraints in Eq. (4.16) are therefore applied to each pair of nodes: one node on the master boundary and the other on the slave boundary, excluding the four corner nodes for which an extra condition is defined next.

   The total number of node pairs is denoted by N_{pb}. For a node pair l, we assign two Lagrange multipliers to the constraints—λ_{c}^{l} for c_{m} and λ_{ϕ}^{l} for ϕ_{m}—and the constraint

equations are then expressed as

$$c_{\mathrm{m}}^{l}\Big|_{\mathrm{mb}} - c_{\mathrm{m}}^{l}\Big|_{\mathrm{sb}} - \nabla c_{\mathrm{M}} \cdot \left(\mathbf{x}_{\mathrm{mb}}^{l} - \mathbf{x}_{\mathrm{sb}}^{l}\right) = 0, \tag{4.59a}$$

$$\phi_{\mathrm{m}}^{l}\Big|_{\mathrm{mb}} - \phi_{\mathrm{m}}^{l}\Big|_{\mathrm{sb}} - \nabla \phi_{\mathrm{M}} \cdot \left(\mathbf{x}_{\mathrm{mb}}^{l} - \mathbf{x}_{\mathrm{sb}}^{l}\right) = 0. \tag{4.59b}$$

For the four corner nodes, we have 2×3 Lagrange constraint equations:

$$u_{\mathrm{m}}^{(2)} - u_{\mathrm{m}}^{(1)} - \nabla u_{\mathrm{M}} \cdot \left(\mathbf{x}^{(2)} - \mathbf{x}^{(1)}\right) = 0, \tag{4.60a}$$

$$u_{\mathrm{m}}^{(3)} - u_{\mathrm{m}}^{(1)} - \nabla u_{\mathrm{M}} \cdot \left(\mathbf{x}^{(3)} - \mathbf{x}^{(1)}\right) = 0, \tag{4.60b}$$

$$u_{\mathrm{m}}^{(4)} - u_{\mathrm{m}}^{(1)} - \nabla u_{\mathrm{M}} \cdot \left(\mathbf{x}^{(4)} - \mathbf{x}^{(1)}\right) = 0, \tag{4.60c}$$

where u takes either c or ϕ, and superscripts $1-4$ represent the four corner nodes.

2. Conservation of concentration and potential between the macro- and micro-scales
We have two more Lagrange constraint equations corresponding to Eq. (4.17):

$$\frac{1}{V_\beta}\int_{V_\beta} \mathbf{N}\,\mathrm{d}V\ \mathbf{c}_{\mathrm{m}} - c_{\mathrm{M}} = 0, \tag{4.61a}$$

$$\frac{1}{V_\beta}\int_{V_\beta} \mathbf{N}\,\mathrm{d}V\ \boldsymbol{\phi}_{\mathrm{m}} - \phi_{\mathrm{M}} = 0. \tag{4.61b}$$

4.C Doyle-Fuller-Newman model

We outline the widely-used DFN model [1]. Here only the equations related to ionic transport in the electrolyte are presented; for the complete DFN model, readers are referred to Refs. [46, 47]. The governing equations are formulated as

$$\epsilon_\beta \frac{\partial c_{\mathrm{n}}}{\partial t} + \nabla \cdot (-D_{\mathrm{eff}} \nabla c_{\mathrm{n}}) = 0, \tag{4.62a}$$

$$\nabla \cdot (-\kappa_{\mathrm{eff}} \nabla \phi_{\mathrm{n}} + \kappa_{\mathrm{D,eff}} \nabla \ln c_{\mathrm{n}}) = 0, \tag{4.62b}$$

where ϵ_β is the porosity (volume fraction of the electrolyte phase β), and c_{n} and ϕ_{n} represent the homogenized concentration and electric potential in the homogenized domain for the electrolyte, respectively (subscript "n" refers to Newman). The effective diffusivity D_{eff} and ionic conductivity κ_{eff} for porous media are taken as their bulk counterparts D_{e} and κ_{e} corrected by porosity ϵ_β and tortuosity τ [22, 31, 48]:

$$D_{\mathrm{eff}} = D_{\mathrm{e}} \frac{\epsilon_\beta}{\tau}, \quad \kappa_{\mathrm{eff}} = \kappa_{\mathrm{e}} \frac{\epsilon_\beta}{\tau}. \tag{4.63}$$

A relation similar to Eq. (4.2c) holds between the effective parameters $\kappa_{D,\mathrm{eff}}$ and κ_{eff}. We remark that in Eq. (4.62), the effective transport properties (D_{eff} and κ_{eff}) are scalar parameters especially for isotropic microstructures and will be replaced by the general tensor format when used for anisotropic microstructures (Fig. 4.7).

In Eq. (4.63), the tortuosity is described by the relation

$$\tau = \epsilon_\beta^{1-\alpha}, \tag{4.64}$$

which is commonly referred to as the Bruggeman relation in the literature [30]. Bruggeman [49] derived expressions for spherical or cylindrical transport obstructing phases for which the parameter α takes the value 1.5 or 2, respectively. The value 1.5 is traditionally used in the DFN model although its validity is obviously restricted to the case of non-overlapping spherical particles [50, 51]. Inserting Eq. (4.64) into Eq. (4.63) gives

$$D_{\mathrm{eff}} = D_{\mathrm{e}}\epsilon_\beta^{\alpha}, \quad \kappa_{\mathrm{eff}} = \kappa_{\mathrm{e}}\epsilon_\beta^{\alpha}. \tag{4.65}$$

In Eq. (4.65) the bulk properties can be constant or concentration dependent.

The effective transport coefficient is defined as

$$\delta = \frac{D_{\mathrm{eff}}}{D_{\mathrm{e}}} = \frac{\kappa_{\mathrm{eff}}}{\kappa_{\mathrm{e}}}. \tag{4.66}$$

Note that the notion of an effective transport coefficient is in principle valid when D_{e} and κ_{e} are constant. Substituting Eq. (4.66) into Eq. (4.63), we can relate tortuosity and effective transport coefficient as follows:

$$\tau = \frac{\epsilon_\beta}{\delta}. \tag{4.67}$$

In numerical simulations, we can directly calculate the effective transport coefficient and then indirectly obtain the tortuosity from Eq. (4.67). In the literature [2, 6], the effective transport coefficient δ, numerically estimated under constant bulk properties, is used to approximate the effective transport properties in the case of concentration-dependent bulk properties:

$$D_{\mathrm{eff}}(c_{\mathrm{n}}) = D_{\mathrm{e}}(c_{\mathrm{e}})\,\delta, \quad \kappa_{\mathrm{eff}}(c_{\mathrm{n}}) = \kappa_{\mathrm{e}}(c_{\mathrm{e}})\,\delta. \tag{4.68}$$

To ease the comparison with our numerical results, effective transport coefficient and porosity are related by means of Eqs. (4.65) and (4.66):

$$\delta = \epsilon_\beta^{\alpha}. \tag{4.69}$$

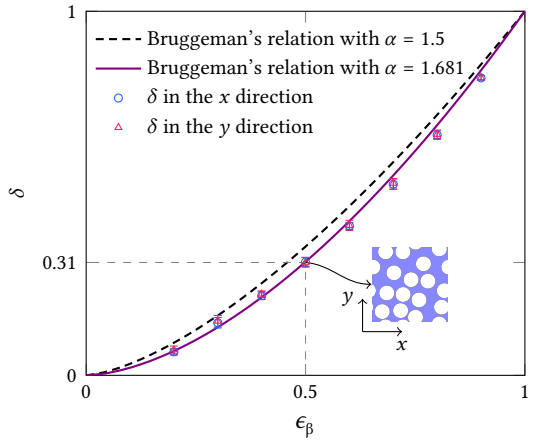

Fig. 4.9. Effective transport coefficient $\delta = D_{\text{eff}}/D_{\text{e}}$ versus porosity ϵ_β (i.e., electrolyte volume fraction) for an isotropic microstructure with circular particles. The coefficients δ in the x and y directions are calculated by D_{11}/D_{e} and D_{22}/D_{e}, respectively, and Bruggeman relation refers to Eq. (4.69). The exponent $\alpha = 1.5$ is customarily used in the DFN model [1]. The figure also indicates the value of the effective transport coefficient at porosity 0.5.

4.D Validation of the microscale approach

For the purpose of validation, Fig. 4.9 compares the effective transport coefficient $\delta = D_{\text{eff}}/D_{\text{e}}$ obtained with the proposed method to the values obtained from Bruggeman relation (4.69) as a function of porosity. In the RVE microscale simulations, the bulk transport properties D_{e} and κ_{e} take constant values, and the RVE contains randomly-distributed circular particles (blocking phase).

In the RVE samples, the number of particles is fixed at 16, which is large enough to obtain converged transport properties, and their radii are held fixed at 0.5 µm; accordingly, the RVE size changes with the porosity. The effective transport coefficient δ in the x direction is calculated as D_{11}/D_{e} (or $\kappa_{14}/\kappa_{\text{e}}$), and that in the y direction as D_{22}/D_{e} (or $\kappa_{25}/\kappa_{\text{e}}$), with the coefficients D_{ii} (or κ_{ij}) defined in Eq. (4.50). For each porosity value, we generate a number of RVE samples (10 samples for porosity values $0.2 - 0.4$, 50 samples for 0.5 and 0.6, and 100 samples for $0.7 - 0.9$) and report the average and deviation of the simulated δ values. The average δ values in the x and y directions are very close to each other due to the isotropy of the RVE microstructure; the difference caused by the microstructural randomness is negligible, as indicated by the small standard deviation error bars at each data point.

The numerical results are described very well by the Bruggeman relation (4.69) with $\alpha = 1.681$, which is coincidentally equal to the value reported by Du et al. [6] obtained from the curve fitting of data obtained from 2462 realizations of randomly packed ellipsoidal particles in a three-dimensional volume. For completeness, we also report Bruggeman

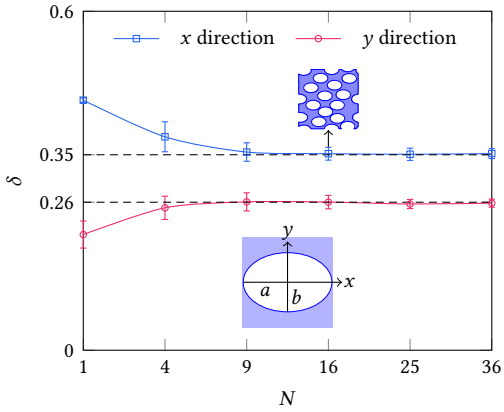

Fig. 4.10. RVE size convergence study: effective transport coefficients $\delta = D_{\text{eff}}/D_{\text{e}}$ in the x and y directions vary with the number N of particles inside the RVE. The coefficient δ in the x and y directions are calculated by D_{11}/D_{e} and D_{22}/D_{e}, respectively. All the particles are aligned with the x direction with the semi-major axis $a = 0.15\,\mu\text{m}$ and semi-minor axis $b = 0.1\,\mu\text{m}$. The number of RVE samples is 50 for $N = 1 - 16$ and 30 for $N = 25$ and 36.

relation with $\alpha = 1.5$, a value used in the DFN model [1] that is strictly valid for spherical particles only [50]. The comparison with the numerical results indicates that the Bruggeman relation with $\alpha = 1.5$ overpredicts the effective diffusivity.

4.E RVE size convergence study

In the FE^2 method, a crucial step pertaining to the microscale FE simulation is the selection of an appropriate RVE size. Here we calculate the effective transport properties employing RVEs of different sizes to verify their expected convergence to unique numerical values. The porosity is fixed at 0.5, and the size of the elliptical particles is specified by the semi-major axis $a = 0.15\,\mu\text{m}$ and the semi-minor axis $b = 0.1\,\mu\text{m}$. The particles are randomly distributed but the major axes are aligned along the x direction. We increase the size of the RVE and with that the number of particles in the RVE from 1 to 36. Figure 4.10 shows convergence of the effective transport coefficients $\delta = D_{\text{eff}}/D_{\text{e}}$ to 0.35 and 0.26 in the x and y directions, respectively, starting from RVEs with $N = 9$ particles. The values of the effective transport coefficients are different due to the anisotropic microstructure and correspond to those at $\theta = 0°$ in Fig. 4.4a. The randomly distributed elliptical particles are generated by the random sequential adsorption algorithm [1]. The 16 particle RVE, with size $1.2\,\mu\text{m}$, is large enough to ensure converged transport properties.

[1]Python script available on Github: https://github.com/mzzhuo/randEllipses.

References

[1] M. Doyle, T. F. Fuller, and J. Newman, *Modeling of galvanostatic charge and discharge of the Lithium/polymer/insertion cell,* Journal of The Electrochemical Society **140**, 1526 (1993).

[2] A. Gupta, J. H. Seo, X. Zhang, W. Du, A. M. Sastry, and W. Shyy, *Effective transport properties of $LiMn_2O_4$ electrode via particle-scale modeling,* Journal of The Electrochemical Society **158**, A487 (2011).

[3] R. E. Garciá and Y.-M. Chiang, *Spatially resolved modeling of microstructurally complex battery architectures,* Journal of The Electrochemical Society **154**, A856 (2007).

[4] G. M. Goldin, A. M. Colclasure, A. H. Wiedemann, and R. J. Kee, *Three-dimensional particle-resolved models of Li-ion batteries to assist the evaluation of empirical parameters in one-dimensional models,* Electrochimica Acta **64**, 118 (2012).

[5] A. Salvadori, D. Grazioli, and M. G. D. Geers, *Governing equations for a two-scale analysis of Li-ion battery cells,* International Journal of Solids and Structures **59**, 90 (2015).

[6] W. Du, N. Xue, W. Shyy, and J. R. R. A. Martins, *A surrogate-based multi-scale model for mass transport and electrochemical kinetics in Lithium-ion battery electrodes,* Journal of The Electrochemical Society **161**, E3086 (2014).

[7] S. Whitaker, *The Method of Volume Averaging* (Springer Netherlands, 1999).

[8] M. Quintard, M. Kaviany, and S. Whitaker, *Two-medium treatment of heat transfer in porous media: Numerical results for effective properties,* Advances in Water Resources **20**, 77 (1997).

[9] G. L. Plett, *Battery Management Systems, Volume I: Battery Modeling*, Vol. 1 (Artech House Publishers, 2015).

[10] A. Bejan, *Advanced Engineering Thermodynamics* (John Wiley & Sons, Inc., 2016).

[11] F. Feyel and J.-L. Chaboche, *FE^2 multiscale approach for modelling the elastoviscoplastic behaviour of long fibre SiC/Ti composite materials,* Computer Methods in Applied Mechanics and Engineering **183**, 309 (2000).

[12] C. Miehe, *Strain-driven homogenization of inelastic microstructures and composites based on an incremental variational formulation,* International Journal for Numerical Methods in Engineering **55**, 1285 (2002).

[13] B. S. Mercer, K. K. Mandadapu, and P. Papadopoulos, *Novel formulations of microscopic boundary-value problems in continuous multiscale finite element methods,* Computer Methods in Applied Mechanics and Engineering **286**, 268 (2015).

[14] A. Sengupta, P. Papadopoulos, and R. L. Taylor, *A multiscale finite element method for modeling fully coupled thermomechanical problems in solids,* International Journal for Numerical Methods in Engineering **91**, 1386 (2012).

[15] J. Schröder, *Derivation of the localization and homogenization conditions for electro-mechanically coupled problems,* Computational Materials Science **46**, 595 (2009).

[16] J. Schröder and M.-A. Keip, *Two-scale homogenization of electromechanically coupled boundary value problems,* Computational Mechanics **50**, 229 (2012).

[17] M.-A. Keip, P. Steinmann, and J. Schröder, *Two-scale computational homogenization of electro-elasticity at finite strains,* Computer Methods in Applied Mechanics and Engineering **278**, 62 (2014).

[18] S. Lee and V. Sundararaghavan, *Multi-scale modeling of moving interface problems with flux and field jumps: Application to oxidative degradation of ceramic matrix composites,* International Journal for Numerical Methods in Engineering **85**, 784 (2010).

[19] A. Salvadori, E. Bosco, and D. Grazioli, *A computational homogenization approach for Li-ion battery cells: Part 1 – formulation,* Journal of the Mechanics and Physics of Solids **65**, 114 (2014).

[20] M. F. Lagadec, R. Zahn, and V. Wood, *Designing polyolefin separators to minimize the impact of local compressive stresses on lithium-ion battery performance,* Journal of The Electrochemical Society **165**, A1829 (2018).

[21] K. E. Thomas, J. Newman, and R. M. Darling, *Mathematical modeling of lithium batteries,* in *Advances in Lithium-Ion Batteries* (Springer US, 2002) pp. 345–392.

[22] X. Zhang and D. M. Tartakovsky, *Effective ion diffusion in charged nanoporous materials,* Journal of The Electrochemical Society **164**, E53 (2017).

[23] D. Perić, E. A. de Souza Neto, R. A. Feijóo, M. Partovi, and A. J. C. Molina, *On micro-to-macro transitions for multi-scale analysis of non-linear heterogeneous materials: Unified variational basis and finite element implementation,* International Journal for Numerical Methods in Engineering **87**, 149 (2010).

[24] R. Hill, *Elastic properties of reinforced solids: Some theoretical principles,* Journal of the Mechanics and Physics of Solids **11**, 357 (1963).

[25] I. Özdemir, W. Brekelmans, and M. Geers, *FE^2 computational homogenization for the thermo-mechanical analysis of heterogeneous solids,* Computer Methods in Applied Mechanics and Engineering **198**, 602 (2008).

[26] I. Özdemir, W. A. M. Brekelmans, and M. G. D. Geers, *Computational homogenization for heat conduction in heterogeneous solids,* International Journal for Numerical Methods in Engineering **73**, 185 (2007).

[27] S. Fernández-Méndez and A. Huerta, *Imposing essential boundary conditions in mesh-free methods,* Computer Methods in Applied Mechanics and Engineering **193**, 1257 (2004).

[28] L. O. Valøen and J. N. Reimers, *Transport properties of $LiPF_6$-based Li-ion battery electrolytes,* Journal of The Electrochemical Society **152**, A882.

[29] M. F. Lagadec, R. Zahn, and V. Wood, *Characterization and performance evaluation of lithium-ion battery separators,* Nature Energy **4**, 16 (2018).

[30] B. Tjaden, D. J. L. Brett, and P. R. Shearing, *Tortuosity in electrochemical devices: A review of calculation approaches,* International Materials Reviews **63**, 47 (2016).

[31] S. J. Cooper, D. Eastwood, J. Gelb, G. Damblanc, D. J. L. Brett, R. S. Bradley, P. J. Withers, P. D. Lee, A. J. Marquis, N. P. Brandon, and P. R. Shearing, *Image based modelling of microstructural heterogeneity in $LiFePO_4$ electrodes for Li-ion batteries,* Journal of Power Sources **247**, 1033 (2014).

[32] M. Ebner, D.-W. Chung, R. E. García, and V. Wood, *Tortuosity anisotropy in lithium-ion battery electrodes,* Advanced Energy Materials **4**, 1301278 (2014).

[33] M. F. Lagadec, M. Ebner, R. Zahn, and V. Wood, *Communication—technique for visualization and quantification of lithium-ion battery separator microstructure,* Journal of The Electrochemical Society **163**, A992 (2016).

[34] M. F. Lagadec, R. Zahn, S. Müller, and V. Wood, *Topological and network analysis of lithium-ion battery components: The importance of pore space connectivity for cell operation,* Energy & Environmental Science **11**, 3194 (2018).

[35] S. J. Cooper, A. Bertei, P. R. Shearing, J. A. Kilner, and N. P. Brandon, *TauFactor: An open-source application for calculating tortuosity factors from tomographic data,* SoftwareX **5**, 203 (2016).

[36] U. Pasaogullari, P. P. Mukherjee, C.-Y. Wang, and K. S. Chen, *Anisotropic heat and water transport in a PEFC cathode gas diffusion layer,* Journal of The Electrochemical Society **154**, B823 (2007).

[37] J. Tan, A. M. Tartakovsky, K. Ferris, and E. M. Ryan, *Investigating the effects of anisotropic mass transport on dendrite growth in high energy density Lithium batteries,* Journal of The Electrochemical Society **163**, A318 (2015).

[38] V. P. Nemani, S. J. Harris, and K. C. Smith, *Design of bi-tortuous, anisotropic graphite anodes for fast ion-transport in Li-ion batteries,* Journal of The Electrochemical Society **162**, A1415 (2015).

[39] J. Yablecki, A. Nabovati, and A. Bazylak, *Modeling the effective thermal conductivity of an anisotropic gas diffusion layer in a polymer electrolyte membrane fuel cell,* Journal of The Electrochemical Society **159**, B647 (2012).

[40] X. Zhang, *Multiscale Modeling of Li-ion Cells: Mechanics, Heat Generation and Electrochemical Kinetics*, Ph.D. thesis, University of Michigan (2009).

[41] W. F. Hosford, *Mechanical Behavior of Materials* (Cambridge University Press, 2005).

[42] C. fu Yang and L. jiang Qin, *Graphical representation and explanation of the conductivity tensor of anisotropic media,* Surveys in Geophysics **41**, 249 (2020).

[43] X. Han, M. Ouyang, L. Lu, and J. Li, *Simplification of physics-based electrochemical model for lithium ion battery on electric vehicle. Part I: Diffusion simplification and single particle model,* Journal of Power Sources **278**, 802 (2015).

[44] F. E. Halabi, D. González, A. Chico, and M. Doblaré, *FE^2 multiscale in linear elasticity based on parametrized microscale models using proper generalized decomposition,* Computer Methods in Applied Mechanics and Engineering **257**, 183 (2013).

[45] J. Cannarella, X. Liu, C. Z. Leng, P. D. Sinko, G. Y. Gor, and C. B. Arnold, *Mechanical properties of a battery separator under compression and tension,* Journal of The Electrochemical Society **161**, F3117 (2014).

[46] V. R. Subramanian, V. D. Diwakar, and D. Tapriyal, *Efficient macro-micro scale coupled modeling of batteries,* Journal of The Electrochemical Society **152**, A2002 (2005).

[47] L. Cai and R. E. White, *Mathematical modeling of a lithium ion battery with thermal effects in COMSOL inc. multiphysics (MP) software,* Journal of Power Sources **196**, 5985 (2011).

[48] D.-W. Chung, M. Ebner, D. R. Ely, V. Wood, and R. E. García, *Validity of the bruggeman relation for porous electrodes,* Modelling and Simulation in Materials Science and Engineering **21**, 074009 (2013).

[49] D. A. G. Bruggeman, *Berechnung verschiedener physikalischer Konstanten von heterogenen Substanzen. I. Dielektrizitätskonstanten und Leitfähigkeiten der Mischkörper aus isotropen Substanzen,* Annalen der Physik **416**, 636 (1935).

[50] B. Tjaden, S. J. Cooper, D. J. Brett, D. Kramer, and P. R. Shearing, *On the origin and application of the Bruggeman correlation for analysing transport phenomena in electrochemical systems,* Current Opinion in Chemical Engineering **12**, 44 (2016).

[51] F. L. Usseglio-Viretta, A. Colclasure, A. N. Mistry, K. P. Y. Claver, F. Pouraghajan, D. P. Finegan, T. M. Heenan, D. Abraham, P. P. Mukherjee, D. Wheeler, *et al.*, *Resolving the discrepancy in tortuosity factor estimation for li-ion battery electrodes through micro-macro modeling and experiment,* Journal of The Electrochemical Society **165**, A3403 (2018).

5

Concluding remarks and future perspectives

5.1 Concluding remarks

The increasing energy demand of electric devices has been driving the development of more robust rechargeable batteries, and a promising avenue is to modify the electrode material morphology from particle to fiber. This thesis aims to provide numerical tools for evaluating electrochemical performance of Li-ion batteries, especially those composed of fiber-based electrodes. In particular, two different types of approaches are exploited: one is a preliminary but efficient method based on fiber arrangement and fiber-contact detection; the other is based on the solution of physics-based governing equations using a FE^2 multi-scale framework.

Chapter 2 The fiber-arrangement-based approach can efficiently explore microstructure configurations and thus quickly evaluate electrode properties such as percolation threshold, electronic conductivity, and active material utilization. The new finding regarding the equivalence between two popular approaches improves the state-of-the-art understanding of the methods for percolation threshold identification in the literature. The extra degree of fiber orientation impacts on the electrode properties but does not change some common features of battery electrodes such as the optimal active-conductive material ratio and the trade-off between energy and power. The discoveries by the numerical simulations shed light on how fiber arrangement affects the overall properties and thus can provide guidelines for future experimental studies of fiber-based electrodes.

Chapter 4 The FE^2 framework offers a more capable alternative to a commonly used approach (Pseudo-2D model) in addressing realistic microstructures. The well-defined microscale problem setting differs from the existing homogenization approaches in terms of characterizing the microstructure using effective transport property tensors. The off-diagonal terms of the transport property tensor are indispensable especially for anisotropic microstructures and the understanding of its importance has been advanced by the microscale simulations. The comprehensive microstructure characterization can offer guidelines for optimal microstructure design to attain desired transport properties. Moreover, the well-defined information exchange between the two scales enables the FE^2 method to allow for

general constitutive relations such as concentration-dependent transport properties.

Chapter 3 The proposed FE^2 framework for the two-equation model extends the conventional framework for the one-equation model by explicitly modeling the interfacial flux and is especially suitable for the battery problem with at least two different phases—the active material and electrolyte. The new feature lies in the separate treatment of the two phases in terms of the volume-averaged macroscale equations, information exchange between the macro- and micro-scales, and boundary conditions of the microscale problem. The microscopic length scale usually has no impact on effective transport properties but affects the tangent matrix of the interfacial flux (e.g., heat transfer coefficient in linear heat conduction problems). The FE^2 framework offers a robust numerical tool for evaluating separate temperature/concentration fields for heterogeneous two-phase media.

5.2 Future perspectives

The endeavor in this thesis to explore battery electrochemical performance is the starting point of more comprehensive studies. The following topics and directions are suggested for more understanding and insights.

First, the FE^2 framework presented in Chapter 4 for ionic transport in electrolyte can be extended by incorporating the framework in Chapter 3 to model the interfacial flux between the active material and electrolyte so that a full battery cell can be simulated using the FE^2 method. The interfacial flux including the lithium ion flux and current flux can be described by Butler–Volmer equation, but different ideas arise as to how to impose the interfacial flux for the microscale simulation. In Gupta et al. [1], "flux based on the Butler-Volmer reaction current was enforced such that the net flux between the two phases was zero", while in Du et al. [2], "the solid-liquid interface is modeled as an insulated wall". In principle, the interfacial flux is an unknown as a function of microscale field variables and should be imposed as the boundary conditions for each domain of the active material and electrolyte. Thus, the interfacial flux is calculated in the way being coupled with the microscale field variables and is generally non-zero. The microscale FE simulation should be conducted with various settings of the interfacial boundary conditions.

Second, the mechanical deformation and potential damage/fracture of the active material can be further incorporated into the current FE^2 framework for the electrochemical processes. The charging and discharging processes in batteries are accompanied with intercalation and deintercalation of lithium into and out of the active material. The consequent volume change of an active particle/fiber is however constrained by surrounding particles/fibers, thus leading to stress development in the active material. The developed stress will in turn affect the electrochemical processes by for example changing the effective transport

properties, and thus it is essential to simultaneously model and simulate electrochemical-mechanically coupled phenomena, especially for electrode materials undergoing large volume changes such as silicon. The repeated charging-discharging processes result in cyclic loading-unloading and can result in damage and fatigue of the active materials. Modeling the mechanical deformation and the damage accumulation at the particle scale and its effect on the continuum-scale capacity loss is urgent for the design of batteries with long cycle life.

Third, a three-dimensional RVE with both the matrix and inclusion domain path-connected should be exploited. For the RVEs studied in Chapter 4, the matrix domain is path-connected, while the "isolated" inclusions are disconnected domain because they are non-overlapping in the two-dimensional setting. The path disconnection in the inclusions (active materials) causes disruption to the transport of lithium and electrons in the active materials, resulting into null effective transport properties at the macroscale. The problem can be avoided in a three-dimensional RVE. As the FE^2 framework is general regardless of problem dimension, it will be interesting to see how the effective transport properties and interfacial flux behave for a three-dimensional RVE where both phases are path-connected. This will also be reflected in the FE^2 modeling of a full battery cell described above: in a real battery electrode microstructure, the pore-filling electrolyte and active/conductive solid materials are path-connected.

Last, well-defined microscale FE simulations can generate training data for a neural network model that can replace the concurrent microscale simulation at each Gauss point in the FE^2 computing process.

References

[1] A. Gupta, J. H. Seo, X. Zhang, W. Du, A. M. Sastry, and W. Shyy, *Effective transport properties of $LiMn_2O_4$ electrode via particle-scale modeling,* Journal of The Electrochemical Society **158**, A487 (2011).

[2] W. Du, N. Xue, W. Shyy, and J. R. R. A. Martins, *A surrogate-based multi-scale model for mass transport and electrochemical kinetics in Lithium-ion battery electrodes,* Journal of The Electrochemical Society **161**, E3086 (2014).

Acknowledgements

The research work presented in this thesis was completed at the Computational Mechanics (CM) group at Delft University of Technology and received funding from the European Research Council (ERC) under the European Union's Seventh Framework Programme (FP7/2007–2013) / ERC Grant agreement n° 617972. I would like to extend my grateful thanks to the CM group for providing excellent working conditions and to the ERC for the financial support.

I wish to express my sincere gratitude to my promotor, Professor Bert Sluys who leads the CM group, for his kind help, advices, and moral support. I thank my promotor and daily supervisor, Professor Angelo Simone, for offering me the Ph.D. position and spending his time in advising me throughout the Ph.D. project. I also owe thanks to Dr. Davide Grazioli for his critical comments on my work and papers. We had a plethora of discussions on the battery project from which I have learned a lot.

The thesis has also benefited from comments and encouragements from my colleagues and friends at TU Delft. Special thanks to Professor Frans van der Meer for organizing our CM group meetings and offering critical comments on my presentations. Other colleagues, officemates, and best friends to whom I am grateful include Ali, Arman, Behrouz, Bram, Debashis, Dongyu, Dragan, Erik, Fanxiang, Fariborz, Iuri, Jafar, Ke Lu, Lars, Liting, Luiz, Lv tao, Marianthi, Mingjuan, Mehdi, Mohsen, Rafid, Richard, Suman, Tiziano, Yaolu, Zheng.

Last but most important of all, I would like to thank my families for being around with me all the time and extending unconditional love and support to me.

Mingzhao Zhuo
August 2020
Delft, the Netherlands

Summary

Conventional battery models (e.g., Pseudo-2D model) were developed especially for particle-based battery electrodes and have limitations in addressing the newly-emerging fiber-based ones. This thesis proposes numerical tools for efficient property evaluation of fiber-based electrodes and for multiscale simulation of battery electrochemical behavior.

An efficient computational model is first developed to evaluate percolation threshold, effective electronic conductivity, and capacity of fiber-based electrodes. The electrode is composed of conductive and active fibers mixed in an electrolyte matrix. This model rests with generation of randomly-distributed fibers by Monte Carlo method. The connection between conductive fibers is used to determine percolation threshold and electronic conductivity, while the connection between conductive and active fibers defines the active material utilization and capacity. An optimal active-conductive material ratio is identified to maximize the electrode capacity, and the study of fiber orientation effect reveals that the isotropic distribution leads to the highest utilization of active fibers.

For more accurate estimation, a FE^2 multiscale framework is further proposed to solve physics-based governing equations. The first part extends the conventional FE^2 method suited to a one-equation model to transient diffusion in a two-phase medium described by a two-equation model. The new features include the macroscale equations derived by the volume-averaging method and separate treatment of the two phases in terms of information exchange between macro- and micro-scales and boundary conditions of the microscale problem. The differentiation of the two phases results in additional macroscale source terms upscaled from the microscale interfacial flux. Unlike effective material properties, the tangents of the interfacial flux depend on the microscopic length scale.

The second part of the FE^2 framework addresses the ionic transport in the pore-filling electrolyte of separators, ignoring the interfacial flux between the electrolyte and the active material. The FE^2 method features a macroscale constitutive relation numerically obtained, rather than assumed as in Pseudo-2D model and many of the existing models, from microscale simulation results. This unique feature enables the FE^2 method to allow for nonlinear (concentration-dependent) transport properties at the microscale and reflect them at the macroscale without postulation. The well-defined microscale problem setting results in effective transport properties expressed in a tensor format that is indispensable for an anisotropic microstructure.

Samenvatting

Conventionele batterijmodellen (bijv. Pseudo-2D-model) zijn speciaal ontwikkeld voor op deeltjes gebaseerde batterij-elektroden en hebben beperkingen bij het aanpakken van de nieuw opkomende vezelgebaseerde modellen. Dit proefschrift stelt numerieke tools voor voor efficiënte evaluatie van eigenschappen van vezelgebaseerde elektroden en voor multischalen simulatie van het elektrochemisch gedrag van batterijen.

Een efficiënt rekenmodel wordt eerst ontwikkeld om de percolatiedrempel, de effectieve elektronische geleidbaarheid en de capaciteit van vezelgebaseerde elektroden te evalueren. De elektrode is samengesteld uit geleidende en actieve vezels gemengd in een elektrolytmatrix. Dit model berust op het genereren van willekeurig verdeelde vezels volgens de Monte Carlo-methode. De verbinding tussen geleidende vezels wordt gebruikt om de percolatiedrempel en elektronische geleidbaarheid te bepalen, terwijl de verbinding tussen geleidende en actieve vezels het gebruik en de capaciteit van actief materiaal bepaalt. Een optimale verhouding actief-geleidend materiaal wordt geïdentificeerd om de elektrodecapaciteit te maximaliseren, en de studie van het vezeloriëntatie-effect onthult dat de isotrope verdeling leidt tot het hoogste gebruik van actieve vezels.

Voor een nauwkeurigere schatting wordt verder een FE^2 multischaalraamwerk voorgesteld om op fysica gebaseerde regeringsvergelijkingen op te lossen. Het eerste deel breidt de conventionele FE^2-methode die geschikt is voor een model met één vergelijking uit naar transiënte diffusie in een tweefasig medium beschreven door een model met twee vergelijkingen. De nieuwe kenmerken zijn onder meer de macroschaalvergelijkingen afgeleid door de volumemiddelingsmethode en de afzonderlijke behandeling van de twee fasen in termen van informatie-uitwisseling tussen macro- en microschaal en randvoorwaarden van het microschaalprobleem. De differentiatie van de twee fasen resulteert in aanvullende macroschaal brontermen opgeschaald van de microschaal grensvlak flux. In tegenstelling tot effectieve materiaaleigenschappen, zijn de raaklijnen van de grensvlakflux afhankelijk van de microscopische lengteschaal.

Het tweede deel van het FE^2-raamwerk behandelt het ionentransport in de poriënvullende elektrolyt van separatoren, waarbij de grensvlakflux tussen de elektrolyt en het actieve materiaal wordt genegeerd. De FE^2-methode biedt een constitutieve relatie op macroschaal die numeriek is verkregen, in plaats van aangenomen zoals in het pseudo-2D-model en veel van de bestaande modellen, uit simulatieresultaten op microschaal. Deze unieke eigenschap stelt de FE^2-methode in staat om niet-lineaire (concentratie-afhankelijke) transporteigenschappen op microschaal mogelijk te maken en deze op macroschaal te reflecteren zonder

postulatie. De goed gedefinieerde probleemstelling op microschaal resulteert in effectieve transporteigenschappen uitgedrukt in een tensorformaat dat onmisbaar is voor een anisotrope microstructuur.

Curriculum Vitæ

Mingzhao Zhuo

11-1990 Born in Anqing, China.

Education

- Ph.D. in Computational Mechanics, Delft University of Technology, the Netherlands 2015–2020
- M.Phil. in Mechanical Engineering, Hong Kong University of Science and Technology, Hong Kong 2012–2015
- B.Eng. with honors in Engineering Mechanics, Sichuan Universiy, China 2008–2012

List of Publications

Journal articles

5. **Mingzhao Zhuo**, Davide Grazioli, Angelo Simone, "Active material utilization and capacity of fiber-based battery electrodes", *Electrochimica Acta*, 333 (2020): 134929. doi:10.1016/j.electacta.2019.134929.

4. **Mingzhao Zhuo**, "FE^2 multi-scale framework for the two-equation model of transient heat conduction in two-phase media" (submitted).

3. **Mingzhao Zhuo**, Davide Grazioli, Angelo Simone, "Tensorial effective transport properties of Li-ion battery separators elucidated by computational multiscale modeling" (under review).

The following publications are not from the Ph.D. project.

2. **Mingzhao Zhuo**, "Timescale competition dictates thermo-mechanical responses of NiTi shape memory alloy bars", *International Journal of Solids and Structures*, 193–194 (2020): 601–617. doi:10.1016/j.ijsolstr.2020.02.021.

1. **Mingzhao Zhuo**, Minglu Xia, Qingping Sun, "Analytical solution of a mass-spring system containing shape memory alloys: Effects of nonlinearity and hysteresis", *International Journal of Solids and Structures*, 171 (2019): 189–200. doi:10.1016/j.ijsolstr.2019.04.004.

Conference presentations and abstracts

May 2019	235th Electrochemical Society Meeting, Dallas, TX, the US. *"A FE^2 Framework for Ionic Transport Modeling in the Electrolyte of a Battery Cell"*
July 2018	10th European Solid Mechanics Conference, Bologna, Italy *"Electrical conductivity and capacity of fiber-based electrodes"*
June 2018	6th European Conference on Computational Mechanics, Glasgow, the UK *"Electrochemical-mechanical interaction in solid polymer electrolyte batteries"*